The Dissertation Committee for Brandon Mark Rawlings Certifies that this is the approved version of the following dissertation:

Photocrosslinkable polymers for temporally stable organic nonlinear optical materials and dual-tone photolithography

Committee:

C. Grant Willson, Supervisor

Michael W. Downer

John G. Ekerdt

Christopher J. Ellison

Benny D. Freeman

Photocrosslinkable polymers for temporally stable organic nonlinear optical materials and dual-tone photolithography

by

Brandon Mark Rawlings, B.S.Ch.E.

Dissertation

Presented to the Faculty of the Graduate School of

The University of Texas at Austin

in Partial Fulfillment

of the Requirements

for the Degree of

Doctor of Philosophy

The University of Texas at Austin

May 2012

Dedication

For Jessica

Acknowledgements

The completion of this dissertation and the successful achievement of my Ph.D. would not have been possible without the encouragement and help of my loving wife, Jessica. This has been a team effort the entire way: she has patiently and kindly reorganized her schedule and priorities countless times to ensure the simultaneous success of our marriage and my education, and she has remained my most faithful confidante, friend, and inspiration.

Obviously, a Ph.D. student's advisor is the most important influence and help in his graduate career. I am very well off to have chosen and been chosen by Grant Willson. There is no doubt that Dr. Willson's focus and attention is directed singularly towards his students' success and benefit, and I am no exception. I am thankful for his uncommon kindness, his vision and leadership, and his untiring efforts directly on my behalf.

My parents, Mark and Gail Rawlings, who have been a constant encouragement to me throughout my life, paid for my undergraduate education and expenses, and have been

As the Willson research group is highly collaborative, there are a number of fellow students who worked alongside me. Dr. Brian Long and Will Bell, who synthesized NLO materials, were of great value to me and were always willing to engage in beneficial discussions. Dr. Wei-Lun "Kane" Jen mentored me in a number of ways during our collaboration in the dual-tone resist work. Xinyu Gu, Younjin Cho, Yuji Hagiwara, Takanori Kawakami, Toshiyuki Ogata, and Ryan Mesch each contributed to the success of the materials-based pitch division project, and I am grateful for Dr. Robert Bristol and Dr. James Blackwell of Intel Corporation for their mentorship and advice during my internship. Dong Park and Warren Herman of the Laboratory for Physical

Sciences at the University of Maryland graciously hosted me and gave me much good advice about measuring NLO properties.

I thank Logan Santos for all the helpful discussions and conversations and for his contributions to our group, and I wish him the best in his future endeavors. Ryan Deschner helped with the revision of this manuscript and has been a loyal friend and helpful critic. The Willson group graduate students and visiting scientists are a uniquely cooperative, supportive group, and I thank each of them for their input and kind help during my studies. The undergraduates in our group that I have been honored to work with, specifically Alex Mitrowski and Daniel Hellebusch, also contributed to the successful completion of my projects.

During my stay in Austin, I have been privileged to have formed relationships with some remarkably loyal and helpful friends. I thank the members of High Pointe Baptist Church in Austin for welcoming us as family and caring for us, especially Juan and Jeanine Sanchez and members of the Manor small group. David and Sarah Trombly were loyal friends to me and Jessica during our time in Austin, and I thank them for the many ways they have enriched our lives.

In all these and above all, I acknowledge and thank God for His kind Providence in helping me towards the completion of this work. S.D.G.

Photocrosslinkable polymers for temporally stable organic nonlinear optical materials and dual-tone photolithography

Brandon Mark Rawlings, Ph.D.

The University of Texas at Austin, 2012

Supervisor: C. Grant Willson

The achievement of thermally stable second-order nonlinear optical (NLO) coefficients in polymers is an important but elusive goal in obtaining useful materials for commercial devices. In order to demonstrate the effect of photocrosslinkable groups on enhancement of stability of NLO properties, a series of NLO polymers were investigated, which contain side-chain NLO chromophores with a variable number of crosslinkable methacrylate groups attached to the chromophore opposite the main chain attachment point. Following electric field poling, polymers were crosslinked by irradiating polymer samples containing a photoinitiator. Decay of second-order NLO properties was measured by second harmonic generation (SHG), and stability of SHG coefficients was significantly enhanced after photocrosslinking for polymers containing multiple crosslinkable groups on the chromophore. Addition of reactive diluents further enhanced stability. The enhancement of thermal stability demonstrates the efficacy of photocrosslinking and suggests that the stability improvements may carry over to systems with more efficient chromophores and more stable polymer backbones.

The addition of photocrosslinkable materials is also exploited in photoresists to mitigate alignment limitations on flexible substrates during photolithographic patterning by enabling imaging of two device layers in a single lithographic exposure. To facilitate

the simultaneous patterning of two device layers, a new photoresist system was developed which is able to store and transfer two images concurrently. The dual-tone photoresist system has the ability to store two independent latent images, distinguished by the incident exposure light wavelength, while remaining compatible with reactive ion etch image transfer processes.

A modified chemically amplified photoresist for 193 nm lithography containing an added photobase generator (PBG) leads to a dual-threshold behavior of the dissolution vs. dose contrast curve that enables pitch division of patterned images. To improve these resists, a study of resist components' effects on line edge roughness and pitch division process windows was performed. The kinetics of two-stage PBGs are compared to single-stage PBGs with a view toward achieving higher acid latent image gradients at the line edge. Application of nuclear magnetic resonance spectroscopy to determine the rate constants for resist components in thin films is demonstrated and discussed as a tool for formulating dual-threshold resists.

Table of Contents

List of Tables

List of Figures

Chapter 1: Introduction

For decades, the design and fabrication of electronic devices has been advancing at staggering rates. As the volume demand for these devices has increased, competition and innovation has driven down fabrication costs, the cost reduction largely coming from reducing the size of solid state devices. Much of this progress has been achieved because of advancements in photolithography, the process used to pattern wafers for semiconductor devices. At the same time, an explosion in the use of such devices has precipitated an increase in demand on communication platforms, including optical communications. As these platforms evolve, there is a need for new devices and new materials to enable modulation and transmission of signals. This work describes research into new crosslinkable polymers for temporally stable nonlinear optical materials and for dual-tone photolithography.

1.1 NONLINEAR OPTICAL MATERIALS

Nonlinear optical materials are one class of materials that are being used in modulators for optical communications. Nonlinear optics (NLO) is the subfield of optics concerned with phenomena caused by the modulation of the optical properties of materials by light. The most familiar optical properties, the index of refraction n and the extinction coefficient k, can be related to the relative permittivity and magnetic permeability which appear in Maxwell's equations. For linear materials, the dipole moment per unit volume, or polarization, is linearly proportional to the applied field:

$$\boldsymbol{P} = \chi^{(1)}\boldsymbol{E} \qquad 1.1$$

The proportionality constant, the linear susceptibility $\chi^{(1)}$, is related to the index and absorption of the material. For cases where the applied optical field is extremely intense, the polarization can exhibit nonlinear behavior, represented by additional terms:

$$\boldsymbol{P} = \chi^{(1)}\boldsymbol{E} + \chi^{(2)}\boldsymbol{EE} + \chi^{(3)}\boldsymbol{EEE} + \cdots \qquad 1.2$$

The nonlinear terms in Equation 1.2 are responsible for a number of interesting and useful phenomena including second harmonic generation, self-phase modulation, optical parametric processes, self-focusing, electro-optic modulation, &c. The nonlinear optical phenomena discussed here are limited to those due to the quadratic or second-order term. Equation 1.2 is general, and the coefficients are tensors with many elements that are themselves frequency dependent, so it convenient to restrict discussions of material properties to those associated with particular phenomena or processes.

1.1.1 Second Harmonic Generation

The most familiar NLO phenomenon and the first to be properly classified as an NLO effect is second harmonic generation (SHG). It was first observed by the irradiation of crystalline quartz with a ruby laser,[1] which produced light at twice the frequency of the incident light. It is one of several optical processes including sum frequency generation, difference frequency generation, and optical parametric amplification that have been used for decades in laser science and are the basis for a wide variety of engineering applications. A ubiquitous example is the diode-pumped solid state frequency doubled laser, commonly found in green laser pointers. Typically, a solid state laser diode pumps a neodymium-doped lasing medium which produces light with a wavelength of 1064 nm. The 1064 nm light passes through an inorganic, crystalline, nonlinear optical material such as potassium titanyl phosphate (KTP), and exits as light with a wavelength of 532 nm, in the green region of the visible spectrum.

The production of light at twice the frequency is a direct consequence of Equation 1.2: for an oscillatory field $\boldsymbol{E} = \boldsymbol{E}_0 e^{-i\omega t} + \mathbf{c.c.}$, the product $\boldsymbol{EE}$ introduces components at twice the frequency (as well as a component with zero frequency). To find the actual

fields produced by the nonlinear optical material, Equation 1.2 is inserted into Maxwell's equations, leading to a wave equation that is modified by the presence of nonlinear terms. The solution to the wave equation involves light at both the fundamental frequency and the second harmonic frequency. However, the amplitudes of the light at the two frequencies are *coupled*, so that energy is exchanged back and forth between the fundamental and second harmonic frequencies as light passes through the material. In order to produce a high efficiency of conversion to second harmonic light, a condition known as phase matching must be achieved. For second harmonic generation, phase matching occurs when $n_\omega = n_{2\omega}$, i.e., the index of refraction is the same at the fundamental and second harmonic frequencies. Very few nonlinear optical materials even approximate this behavior; for most materials, the index of refraction increases monotonically with frequency in the region of interest.

A common solution to this problem involves taking advantage of birefringence, which occurs commonly in NLO materials. Birefringent materials exhibit a dependence of index of refraction on the direction of polarization of light as it passes through the material, which leads to refraction into two rays, termed the ordinary and extraordinary rays. By tuning the angle of incidence, or the temperature of the birefringent material, the dispersion and birefringent effects can be made to cancel.[2] This is only possible under carefully controlled conditions, however. The consequence is that currently, inorganic crystalline materials dominate the market for SHG materials because their dispersion and birefringence characteristics as well as their NLO properties are inherent from their crystal structures. Maximum SHG efficiency can only be achieved by phase matching, but at high laser power, there is sufficient SHG signal generated to allow material characterization even without achieving the phase matched condition.

1.1.2 Electro-optic modulation

The electro-optic (EO) effect, or Pockels effect, is the modulation of the index of refraction of a material in proportion to an applied electric field. The most important applications of the EO effect include Q-switching of laser cavities for pulse production and modulation of electrical signals to optical signals for communications networks. A model application of the electro-optic effect in modulation for telecom networks is the electro-optic Mach-Zehnder interferometer, shown in Figure 1.1. In such a device, light is coupled into a waveguide containing an EO material, and the light is split into two pathways, one surrounded by electrodes that allow a voltage to be applied across the pathway. The applied voltage leads to a change in refractive index and an accompanying phase delay. If a half wave phase delay can be generated, the two signals deconstructively interfere, leading to the suppression of the output.

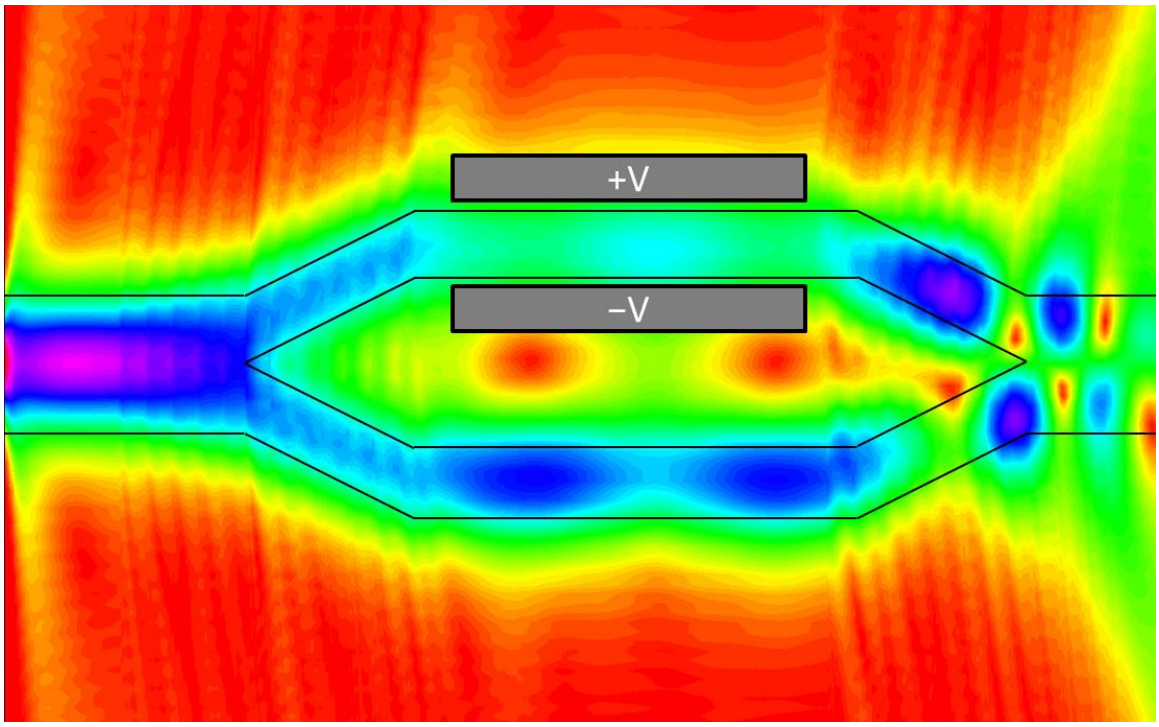

Figure 1.1: An illustration of an electro-optic Mach-Zehnder interferometer, representing amplitude of a Gaussian optical pulse as it propagates through a split waveguide. The application of a voltage on one leg of the waveguide interferometer causes a phase delay, leading to destructive interference of the pulse at the output when the phase delay is half a wave.

The electro-optic coefficient, r_{ij}, describes the magnitude of the effect of an applied electric field on the index of refraction of a material through the following equation:

$$\Delta\left(\frac{1}{n^2}\right)_i = \sum_j r_{ij}E_j \qquad 1.1$$

Like other second-order nonlinear coefficients, it is dependent on the direction of the applied field and the direction of polarization of the light and has units identical to inverse electric field, or pm/V. Using a Taylor expansion, it can be shown that for small $r_{ij}E_j$, the change in the index is approximately proportional to the applied field times the electro-optic coefficient.[3]

Commercial EO modulators that are used to transduce electrical signals to optical and vice versa frequently use lithium niobate, $LiNbO_3$, because it has a large electro-optical coefficient and is optically transparent in the near infrared region that is commonly used for fiber optic communications.[4] Such modulators typically incorporate Mach-Zehnder interferometers with lengths on the order of 1 cm and voltages less than 5 V. These devices are large compared to the scale of integrated circuits.

Inorganic EO modulators dominate the market for modulator materials, but organic materials are highly desirable due to their potential to achieve higher bandwidths with lower fabrication costs. During the late 1980s and early 1990s, a number of academic and industrial research programs were dedicated to using organic EO modulation for optical switches and modulators for time-division multiplexing (TDM) of optical signals. However, the commercialization of wavelength-division multiplexing led to a decrease in demand for organic EO materials research.[5] Recently, the increased demand on data communication networks due to bandwidth intensive applications such as video streaming has led to a resuscitation of interest in organic EO materials.

Although organic EO materials may not replace lithium niobate, they possess advantages that make them attractive for new applications of EO modulators. The response times of organic EO modulators are on the picosecond time scale, allowing for bandwidths of up to 10 THz, greater than those that can be obtained by inorganic materials. In addition, organic EO polymers are far more easily deposited and patterned than crystalline materials. Finally, organic EO materials are capable of much higher electro-optic coefficients than lithium niobate or similar material, by more than an order of magnitude in many cases.

Organic electro-optics are also utilized in photorefractive materials. In this case, local electric fields are created by a charge separation that is induced by the absorption of

light. These local electric fields cause corresponding changes in refractive index that are dependent on the illumination. These changes in refractive index can persist after exposure, yielding a material that has an imbedded refractive index pattern. Such a pattern is useful in applications such as updateable holographic displays.[6]

1.1.3 Material requirements for second-order NLO properties

In order for a material to have useful second-order nonlinear properties, it must have certain symmetry properties. One symmetry requirement can be illustrated by considering the polarization response in the presence of an oscillating electric field. As shown Figure 1.2, the polarization response can be linear (b), nonlinear and noncentrosymmetric (c), or nonlinear and centrosymmetric (not shown). The nonlinear response can be decomposed into its frequency components. Noncentrosymmetric responses include components with even-valued harmonics, including, in this case, a frequency-doubled component as well as a DC component, while symmetric responses never include even-valued harmonics. A noncentrosymmetric arrangement of atoms and/or electron density is necessary to produce a noncentrosymmetric response, so *only noncentrosymmetric materials can exhibit second harmonic generation and the Pockels effect*. Although second-order nonlinear optical coefficients are third-rank tensors with 27 independent elements, assumptions about the permutation of frequencies and the mathematical formalism of Equation 1.2 result in additional symmetries, which reduce the number of independent nonzero elements to 18 or fewer.

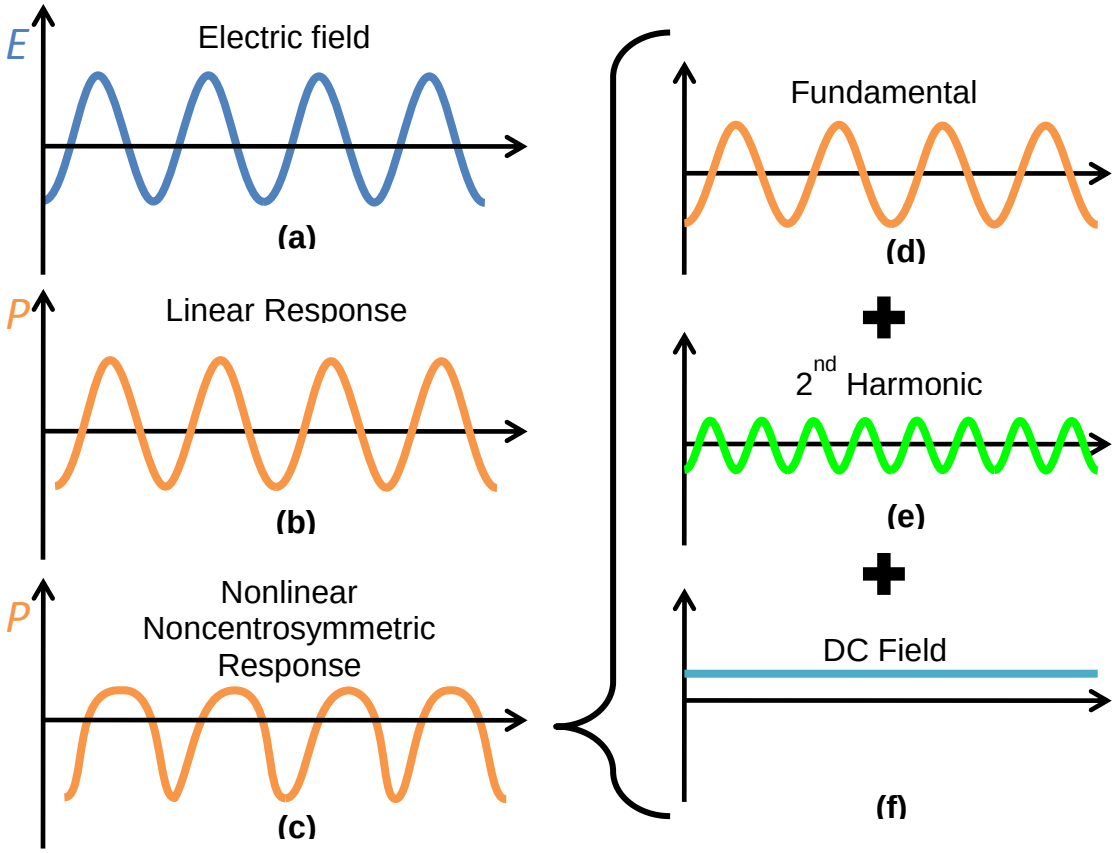

Figure 1.2: Illustration of polarization response to an optical field: (a) Oscillatory electric field of light incident on a nonlinear optical material; (b) linear polarization response; (c) nonlinear noncentrosymmetric response. The noncentrosymmetric response can be analyzed in terms of its Fourier components, including, among others, a component with the fundamental frequency of the incident light (d), a frequency-doubled component (e), and a DC field (i.e. optical rectification) component (f).

For organic and inorganic crystalline materials, the symmetry properties are determined by the symmetry of the crystal class to which the material belongs. Most crystal classes are noncentrosymmetric, but the number of independent elements in second-order NLO coefficients varies: lithium niobate has three independent elements under Kleinman symmetry conditions, while crystalline quartz has just two.[7] Crystals such as lithium niobate are ferroelectric, meaning that they have a nonzero electric

polarization at zero field, owing to the displacement of the lithium and niobium atoms relative to oxygen atoms in the unit cell, as shown in Figure 1.3. The displacement of lithium atoms with respect to both niobium and oxygen atoms is most easily seen.[8] The noncentrosymmetry of the crystal also gives rise to a number of other useful properties, such as pyroelectricity and piezoelectricity.

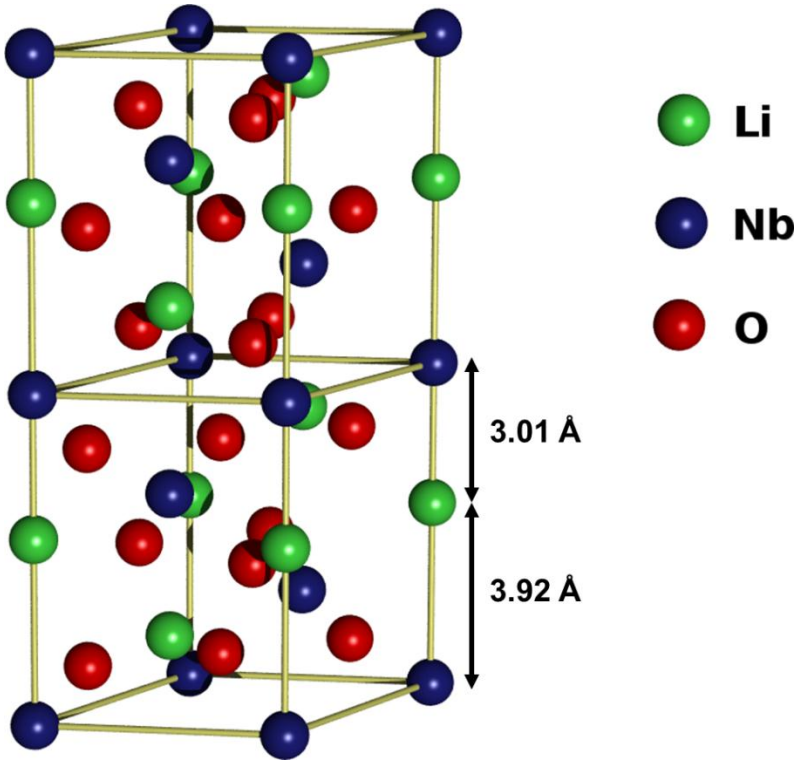

Figure 1.3: Hexagonal unit cell of lithium niobate ($LiNbO_3$), showing displacement of lithium and niobium with respect to the planar oxygen sheets. The displacement of lithium atoms is most easily seen. Adapted from Hellwig.[9]

Organic crystals with nonlinear optical properties can have much larger nonlinear optical coefficients than current inorganic crystals, because their structures can be tailored to incorporate noncentrosymmetry. The most studied and well-known organic NLO crystal is 4-N,N-dimethylamino-4'-N'-methylstilbazolium tosylate (DAST), which

was first reported in 1989 by Marder *et al.*,[10] but has continued to be an important material for a broad range of applications, from SHG and EO modulation to generation of terahertz (THz) radiation. The high nonlinear susceptibility of DAST and other nonlinear organic crystals is due to both the electronic structure of the molecular ions that make up the crystal and the optical and acoustic lattice vibrations of the crystal, but the electronic component dominates, in contrast to inorganic crystalline NLO materials.[11]

1.1.4 Organic NLO molecules and polymers

The electronic component of nonlinear optical susceptibility carries over to noncrystalline organic materials. Organic molecules can often be designed to possess high NLO coefficients by incorporating electron-rich or electron-deficient functional groups, in the same way that materials with very high dipole moment can be produced by incorporating electronegative or electropositive groups in the appropriate arrangement. Well-developed quantum chemical analytics[12,13,14] as well as empirical results on a wide variety of NLO molecules have elucidated clear structure-function relationships.

The molecular first hyperpolarizability, often termed β, is the molecular equivalent of bulk nonlinear optical coefficients, and can be calculated in the two-level approximation as the difference in dipole moment between the ground and excited states, or between the highest occupied molecular orbital (HOMO) and the lowest unoccupied molecular orbital (LUMO). In order to produce a large change in dipole moment, one might incorporate both electron donating and electron accepting groups. Charge transfer from the donating to the accepting group results in a change in dipole moment, since the electron accepting group becomes formally negatively charged.

Substituted benzene is a simple example of the influence of molecular symmetry on nonlinear optical properties. Benzene has no second-order NLO properties because it

is centrosymmetric, but by substituting it with amino- or nitro- groups, it can be made to have appreciable NLO activity. Table 1.1 shows the molecular hyperpolarizability of several substituted benzenes.[3] Benzene substituted with both a nitro- group and an amino- group has the highest dipole moment, and more importantly, the highest difference in dipole moment between the ground and excited states. The conjugated π-electron system of benzene facilitates charge transfer from the electron donating amino- group to the electron accepting nitro group.

Table 1.1: Molecular hyperpolarizability of several substituted benzenes, both experimentally measured and calculated based on the contribution from charge transfer resonance. (From Prasad and Williams 1991)

	$\beta_{exp} \times 10^{50}$ ($C^3\ m^3\ /\ J^2$)	$\beta_{CT} \times 10^{50}$ ($C^3\ m^3\ /\ J^2$)
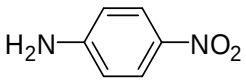	12.8	7.2
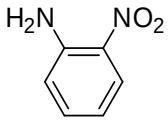	3.8	4.0
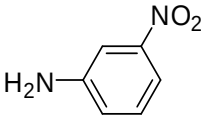	2.2	1.5
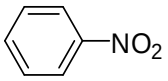	0.8	--
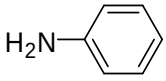	0.4	--

Measurement of molecular second order NLO susceptibilities is complicated by the fact that organic liquids and amorphous solids do not generally possess bulk

noncentrosymmetry. It is therefore necessary to induce a second harmonic response by applying an electric field in a measurement known as EFISHG (electric-field-induced SHG).[15] Hyper-Rayleigh scattering[16] is another widely used method that is able (in contrast to EFISHG) to determine β without knowing from the dipole moment.

1.1.5 Poled polymers

While a host of organic molecules have significant molecular NLO susceptibility, bulk nonlinear optical susceptibility in a material requires aligning the NLO chromophores. Organic polymers are the most common hosts for aligned chromophores. The chromophore can be incorporated covalently into the monomer, which is then polymerized, or it can be added as a dopant. Application of an electric field causes temporary alignment of the chromophores producing bulk second-order NLO susceptibility, among other properties. Poling polyvinylidene fluoride (PVDF), for instance, imparts useful properties of ferroelectricity,[17] piezoelectricity,[18] pyroelectricity,[19] and second-order nonlinear optical phenomena.[20]

Most nonlinear optical poled polymers consist of a polymer host doped with NLO chromophore guests dispersed throughout the polymer matrix. The polymer is heated to near its glass transition temperature T_g and an electric field is applied, either by two electrodes on opposite sides of the polymer, or via a corona discharge created by a needle or wire overtop the polymer. The field-induced alignment of the chromophores can be monitored in real time by using second harmonic generation and is dependent on the free volume of the polymer and the rotational mobility of the chromophores, among other effects.[21] After achieving alignment, the polymer is cooled to well below its T_g, and the applied field is finally removed. A prototypical example is disperse red 1, an azo stilbene

dye with an amine electron donor and a nitro- electron acceptor, doped in poly(methyl methacrylate) (PMMA) or polycarbonate.

The relationship between the bulk and molecular NLO coefficients is complicated in general, but it can be determined with some special assumptions. When the there is no interaction between chromophores, and when the chromophores are assumed to be dipoles in a field, statistical mechanics can be used to derive the following for poled polymer systems:

$$\chi^{(2)} = N f_1^2(\omega) f_2(\omega) \langle \cos^3 \theta \rangle \beta \qquad 1.3$$

In this equation, N is the chromophores number density, the f_1 and f_3 are local field factors which are dependent on the dielectric function, β is the molecular hyperpolarizability, and $\langle \cos^3 \theta \rangle$ is an order parameter that specifies average orientation of chromophores with respect to the principal axis. There are several models for the order parameter, but in all of them, the orientation increases with increased poling field.

Equation 1.3 implies that the bulk nonlinear optical susceptibility increases with the number density of the chromophores. This is only valid, however, at concentrations low enough that the chromophores are noninteracting. At high concentrations, aggregation of the chromophores causes a leveling off of the NLO susceptibility. The concentration at which this occurs varies among models and chromophores shapes.[22] One goal of research in NLO polymers has been to optimize the interactions of the chromophore with the polymer guest and other chromophore molecules to enhance the level at which the polymer can be doped.[23, 24]

1.1.6 Stability of NLO effect in poled polymers

While polymeric NLO materials have advantages over inorganic crystalline materials including high NLO coefficients and fast response times, their deficiency is in

the stability of the NLO coefficients. This instability occurs due to photooxidation or isomerization of the chromophore as well as relaxation of the chromophores to a disordered state. While photooxidation remains a challenge, it can be solved by protecting the polymer from singlet oxygen, either by using a barrier or by adding a singlet oxygen quencher.[5] Relaxation of the chromophores is a problem inherent from the nature of polymeric NLO materials and it is made worse by the fact that devices that incorporate NLO materials typically operate at temperatures well above normal room temperature.

The most straightforward way to increase the thermal stability of guest-host NLO polymers is to choose a polymer host with a high T_g. Currently, a popular choice is amorphous polycarbonate, which has a T_g of nearly 200 °C, although the plasticization effect of added chromophore reduces it. A higher glass transition slows the relaxation of the chromophore within the host, because the backbone of the polymer host moves less. The obvious downside of this is that the poling temperature must be increased, and poling becomes more difficult at higher temperatures. But even if the T_g of the polymer is increased, when manufacturing integrated optics devices, it may be necessary to expose the material to temperatures above 200 °C for minutes or hours during downstream processes.

The decay of dielectric and nonlinear optical properties of polymers illustrates time-temperature superposition. Several models, including the William-Landel-Ferry equation[25] and more advanced models[26] can be used to describe the rate of decay as the temperature approaches and exceeds the glass transition. The rate of relaxation can be tracked by following the amount of SHG as a function of time at a constant temperature and by measuring SHG during a temperature ramp at constant ramp rate. These experiments provide complementary methods to track decay.

Restricting the motion of the chromophore in the polymer by covalently attaching the chromophore to the polymer chain can be expected to increase the stability of NLO coefficients with time. This was demonstrated with PMMA and an azo dye by Singer *et al.*,[27] who found a significant increase in both the overall efficiency and the stability of SHG coefficients, as illustrated in Figure 1.4, which plots SHG coefficients versus time for both the guest/host polymer and the pendant chromophore polymer. Restricting the motion of chromophores can also effectively reduce the dimensionality of the system, changing the relationship between the chromophore alignment and bulk nonlinear optical coefficients.[28]

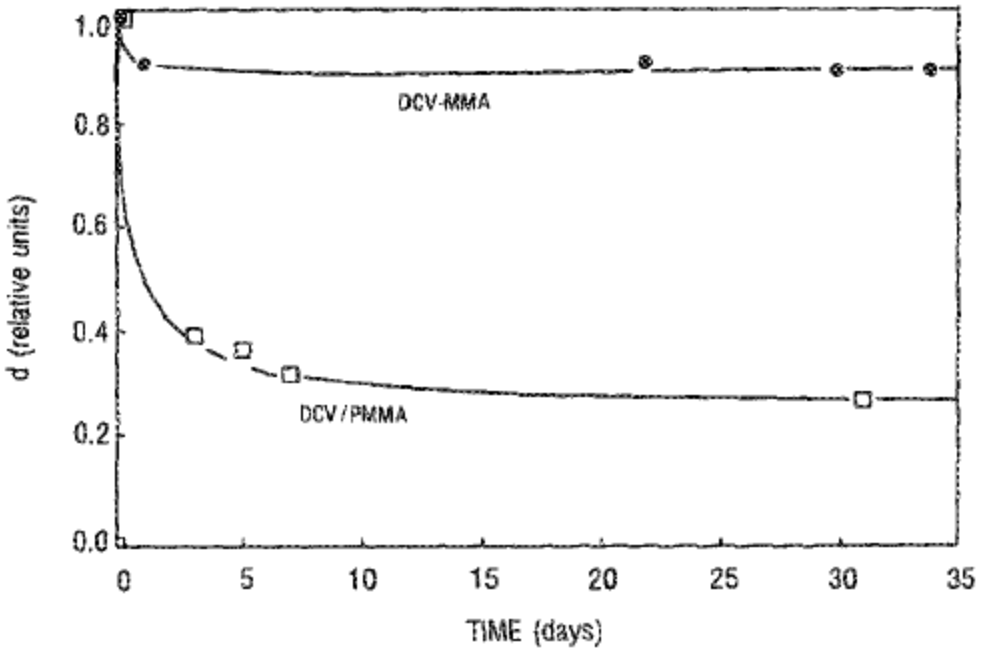

Figure 1.4: Decay of second harmonic coefficient of poly(DCV-MMA) and DCV/PMMA (mixture) corona-poled films. 'DCV' refers to 4-dicyanovinyl-4'(diethylamino) azobenzene and its functionalized analog. Reprinted with permission from Singer *et al.*[27] Copyright 1988, American Institute of Physics.

Thermosetting polymers offer an attractive feature in that they can be poled at low temperatures and later cured to increase their glass transition. For example, polymers with pendant reactive groups can be thermally cured to create interpenetrating polymer networks that lead to stability of NLO effects.[29] However, thermal curing presents a difficulty because heating leads to increased mobility of chromophores, so there is a tradeoff between maximizing poled order and maximizing long term thermal stability. Even for crosslinking that is photoinitiated, the conversion tends to increase with temperature, so that the tradeoff remains, though it may be mitigated. It is desirable to completely separate poling from crosslinking.

Although thermosetting polymers and pendant chromophore polymers increase stability, neither of these systems directly prevent the chromophore from reorienting. In both cases, reorientation of the chromophore is dependent on alpha relaxations in the main chain. Further improvement can be gained if the chromophore is tied to a polymer backbone on both ends of the chromophore. This is accomplished by attaching a polymerizable group onto the chromophore opposite the main polymer chain. Crosslinking causes the chromophore to be linked to two chains, so that relaxation involves rotation of the two main chains, which is obviously more difficult if the chains are connected through entanglements. A main goal of the work presented in Chapter 3 is to show the effect of crosslinking across the chromophore on stability of SHG coefficients.

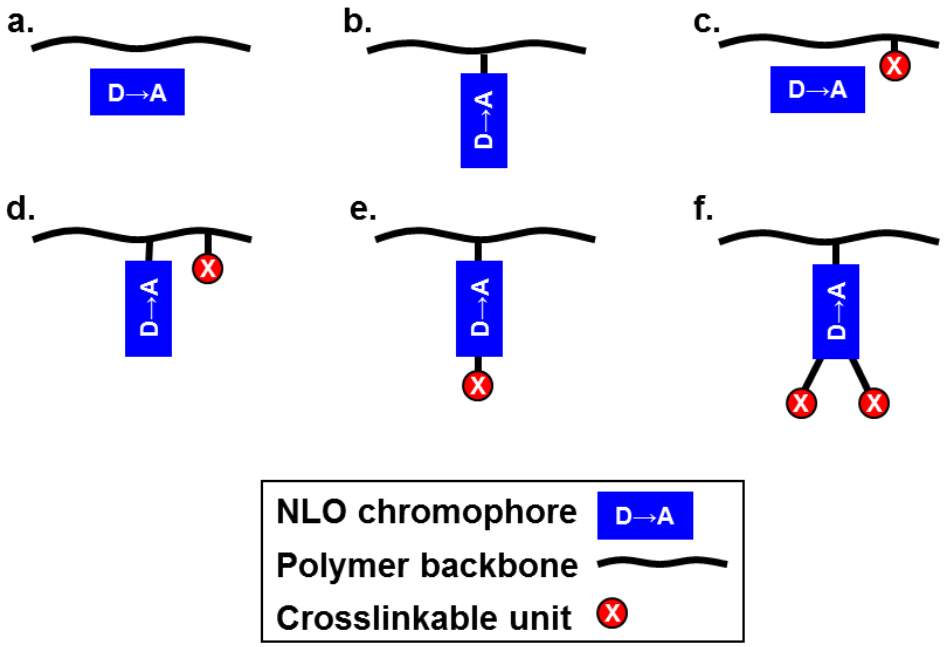

Figure 1.5: Schemes for incorporating an NLO chromophore into a polymer: a) guest-host mixing; b) pendant chromophore; c) guest host in a crosslinkable polymer; d) pendant chromophore in a crosslinkable polymer; e) crosslinking across the chromophore; f) multiple crosslinkable groups on the chromophore.

Figure 1.5 illustrates several motifs for incorporating NLO chromophores into poled polymers. In addition to determining the effect of crosslinking across the chromophore (Figure 1.5e), a major goal of the present research is to determine the effect of multiple attachment points (Figure 1.5f) on enhancing stability of NLO coefficients. Multiple crosslinks across the chromophore are expected to increase the amount of interchain crosslinking, i.e., the crosslinks will be formed between chains that are less correlated in chain motion.

While thermal stability of nonlinear optical effects is not the only area that needs to be addressed for organic NLO materials to become commercially viable, addressing it successfully has the potential to make their production compatible with a wider range of

fabrication processes, including those used to make integrated circuit devices. This includes the patterning of NLO polymers by lithography, including either traditional photolithography or alternative lithography techniques such as imprint lithography.

1.2 DUAL-TONE PHOTOLITHOGRAPHY

1.2.1 The role of photolithography

Since the introduction of the transistor as the primary building block of digital logic circuits, the production output of the semiconductor industry has grown exponentially. Global semiconductor sales in 2010 were $298 billion and are forecast to top $300 billion in 2011.[30] The growth of the semiconductor industry was predicted by Fairchild Semiconductor Inc. founder Gordon Moore, who in 1965 forecasted an exponential increase in the number of transistors on integrated circuits as a function of time.[31] Moore's Law, illustrated by Figure 1.6 as the transistor count per microprocessor by year, was an economic prediction based on the costs of production and research and development, and has been sustained for decades by innovation in patterning technology, applied physics of solid state devices, and CPU architecture.

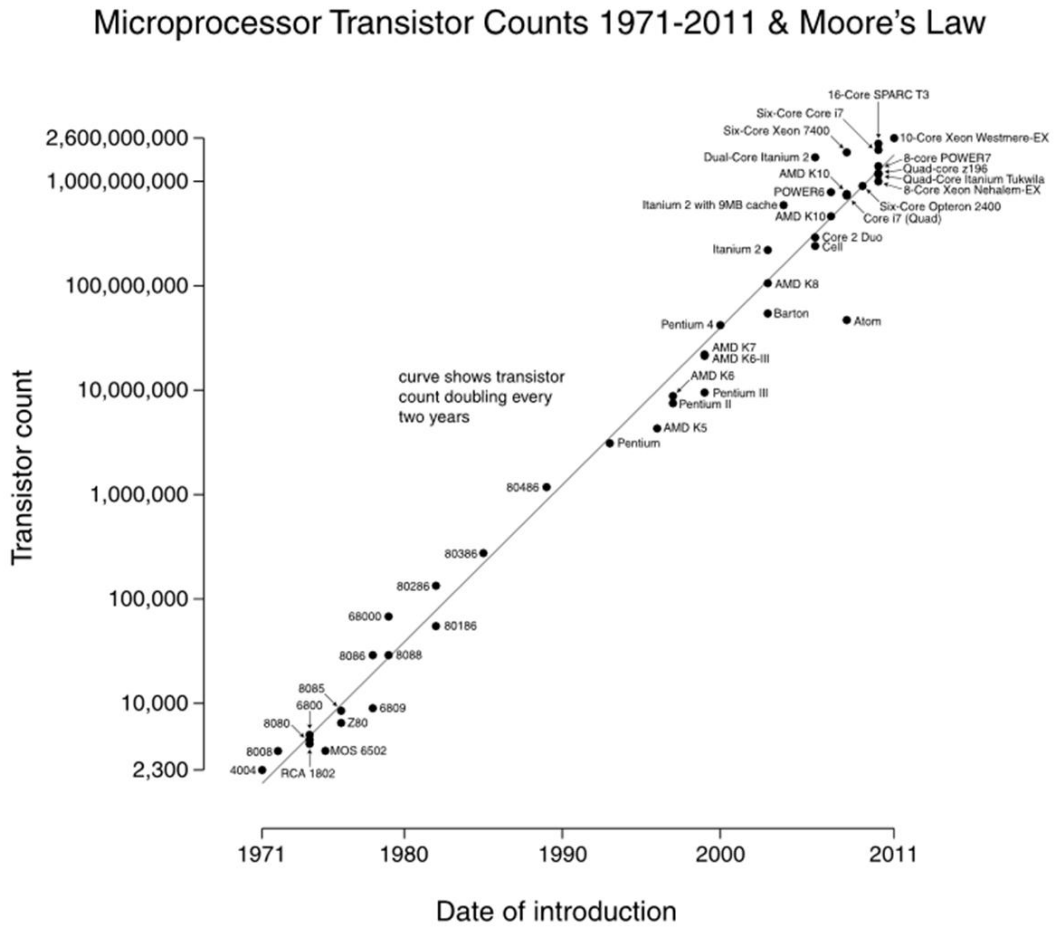

Figure 1.6: The transistor count of commercial microprocessors by year, illustrating Moore's law. The number of transistors on a microprocessor has grown from 2,300 to 2.6 billion since 1971. (Used under Creative Commons license: CC-BY-SA-3.0.)

Photolithography is the patterning of a substrate through a process mediated by a light sensitive material resulting in generation of a relief image (or chemical image) of a template or master. It has been and continues to be a key process in the fabrication of semiconductor devices that are the backbone of the digital age. As devices have become more complex and the number of transistors has ballooned, the size of those structures

has decreased, enabled by advances in photolithography. Patterning is necessary to create the complex multilevel structures common to semiconductor devices. Figure 1.7 shows a typical cross-section and 3D rendering of a typical integrated circuit device manufactured in the early 2000s. The transistor source, drain, and gates, along with copper interconnect lines, trenches, and vias must all be defined lithographically. The number of layers continues to grow with each successive technology node requiring an increasing number of lithography steps.

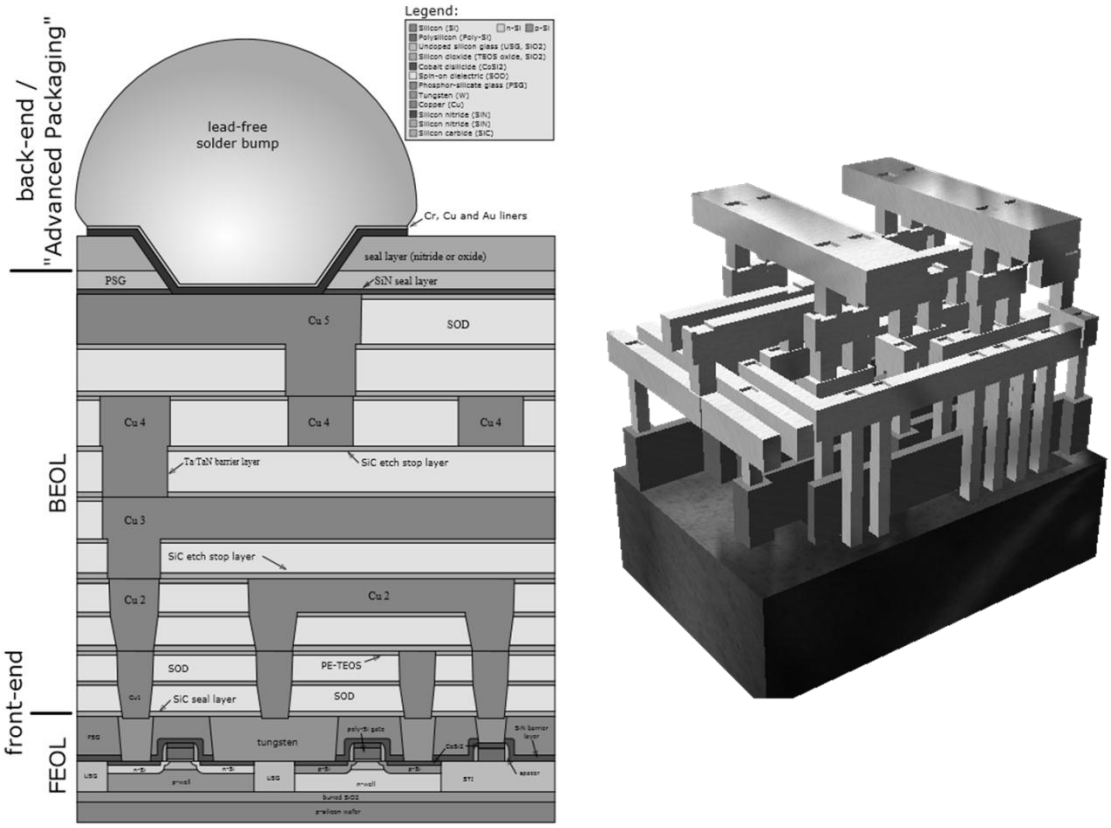

Figure 1.7: Cross-section schematic and 3D rendering of an integrated circuit device typically manufactured in the early 2000s. (Used under Creative Commons license: CC-BY-SA-3.0.)

The photolithographic process starts with a substrate that is coated with a light-sensitive polymeric photoresist. The resist is illuminated with visible or UV light that first

travels through a photomask, which allows light to be transmitted only in designated areas to create an image of the pattern on the photomask. The process is illustrated in Figure 1.8. The photoresist generally serves two purposes: first, it must undergo a light-dependent chemical change (usually in the form of a solubility switch), and second, it must effectively resist etching or ion implantation. In the usual case where the photoresist undergoes a solubility switch, a developer (often an aqueous base or an organic solvent) is applied to remove soluble areas. After developing, the photoresist that remains forms a relief image identical to the image on the photomask. The photoresist relief image is transferred into the underlying material via an etching process that selectively etches the underlying material but leaves the resist and the material under it unchanged. The relief image can also be transferred as an ion doping image by using ion implantation instead of etching. Finally, the photoresist is stripped, leaving a relief image (or other image) in the underlying substrate.

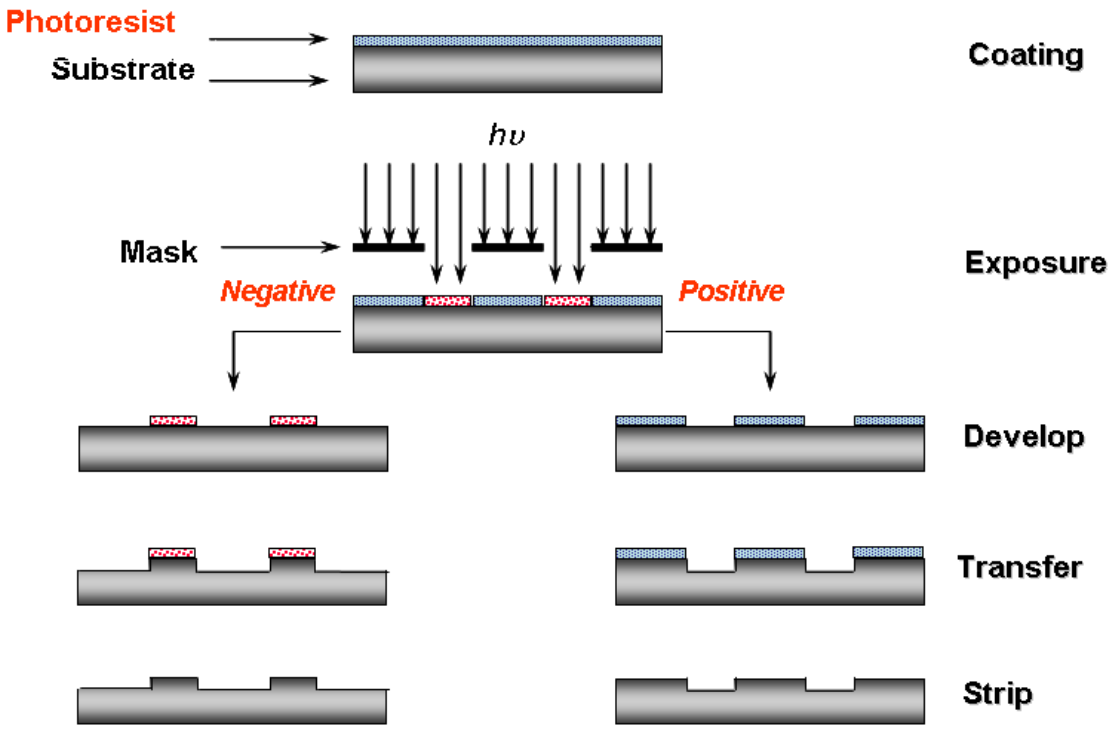

Figure 1.8: Overview of the photolithography process. After the resist is spin-coated onto a substrate, it is illuminated through a mask, causing a change in solubility in developer (either positive or negative). The relief image is transferred to the substrate and the photoresist is removed.

Photoresists (or more properly photoresist/developer combinations) are categorized according to the solubility switch that occurs in the illuminated regions. Resists that become more soluble in developer upon illumination are positive tone, and those that become less soluble are negative tone. Although resists are commonly referred to as positive or negative tone, the solubility switch is dependent on the resist, the developer, and the wavelength of illumination, among other factors. For instance, a resist developed by Fujifilm Corp. can be developed with either an aqueous base, tetramethylammonium hydroxide (TMAH), or with an organic solvent, or both successively.[32]

Accompanying the exponential growth in the number of transistors has been a concurrent decrease in the minimum size of features produced by photolithography. The minimum feature size is dependent on the size of features on the photomask, and the ability to produce an optical image in resist that resolves the smallest features. The formation of any optical image is subject to diffraction. At its best, photolithography is diffraction limited, and the minimum feature size is given by Rayleigh's equation:

$$W = \frac{k_1 \lambda}{NA} \qquad 1.4$$

In this equation, W is the minimum feature size that can be resolved optically, λ is the wavelength of light in meters, NA is the numerical aperture of the objective lens, and k_1 is a process-dependent factor. Resolution of a lithography system is dependent on the image that is being printed.

Rayleigh's equation gives direction on how to reduce feature sizes. The factor k_1 is dependent on the photoresist, illumination, and the mask. However, for a perfect photoresist, and using off-axis illumination and phase-shift masks, $k_1 \geq 0.25$ is the limit for dense lines and spaces. The numerical aperture (NA) is related to the size of the objective lens. Early lithography systems featured a photomask that contacted the resist directly without a lens. These were replaced by proximity printing, where the mask is suspended a short distance above the wafer (shown in Figure 1.8). Proximity lithography was replaced by projection printing, in which the diffracted image coming out of the photomask is collected and focused on the wafer plane using an objective lens system. In practice, the number and complexity of lens systems has grown.

The numerical aperture of lithography systems has increased, but it is limited to the index of refraction of the medium. Until the mid-2000s, air or vacuum, with an index of 1.0 was the medium, so the numerical aperture was limited to 1.0. By introducing a

higher-index liquid (water) between the objective lens and the photoresist (immersion lithography), the NA has been increased to greater than 1.4. However, in order to increase the NA further, it will be necessary to have higher index lenses,[33, 34] photoresists,[35] and immersion fluids.[36]

The remaining factor in Rayleigh's equation is the wavelength λ. Minimum feature sizes producible by photolithography shrank as a result of repeated moves to lower wavelengths. Mercury arc-lamp sources provided visible and ultraviolet light at 436 nm (g-line), 405 nm (h-line), and 365 nm (i-line). Excimer laser sources at 248 nm (KrF) and 193 nm (ArF) replaced arc-lamp sources, and 157 nm excimer lithography was developed to replace 193 nm, but it was not used in production due to high development costs and the advent of immersion lithography. As the wavelength of light decreases, adapting the infrastructure required for production becomes more costly and difficult. For instance, the next generation lithography tool, extreme UV lithography, uses light at 13.5 nm, a wavelength that is absorbed by practically all matter, including air, so it uses reflective rather than transmissive optics. In doing so, it eliminates the ability to use a mask pellicle and requires new mask inspection and cleaning tools and new defect analysis tools.[37] The cost of such a tool is estimated to 125 million dollars each.

1.2.2 Large area and flexible substrates

Traditional photolithography has exceeded expectations in terms of the number of components it can pattern on silicon wafers, and most resources for lithography development have been focused on achieving ever smaller features. As transistor-based devices continue to permeate medicine, sensing, communications, and other applications, the diversity of patterned devices will expand. For instance, demand for flexible displays requires patterning on flexible substrates. The patterning of large area substrates presents

another challenge. Traditional photolithography, as well as laser ablation,[38] inkjet patterning,[39] imprint lithography,[40] etc. are all being explored for patterning flexible and large area substrates on different scales.

Traditional microfabrication processes incorporating lithographic patterning rely heavily on precise alignment and overlay control between device layers. When patterning on top of a patterned substrate, alignment marks are included to ensure overlay between serially patterned layers. For flexible substrates, however, the flexible and conformal nature of the substrates introduces distortions between successive lithography steps, as shown in Figure 1.9, limiting the accuracy of alignment and overlay during the patterning of these materials.[41, 42] Misalignment is particularly detrimental to fabrication of thin film transistors (TFTs), where the gate must be accurately aligned to the source and drain for proper device function.

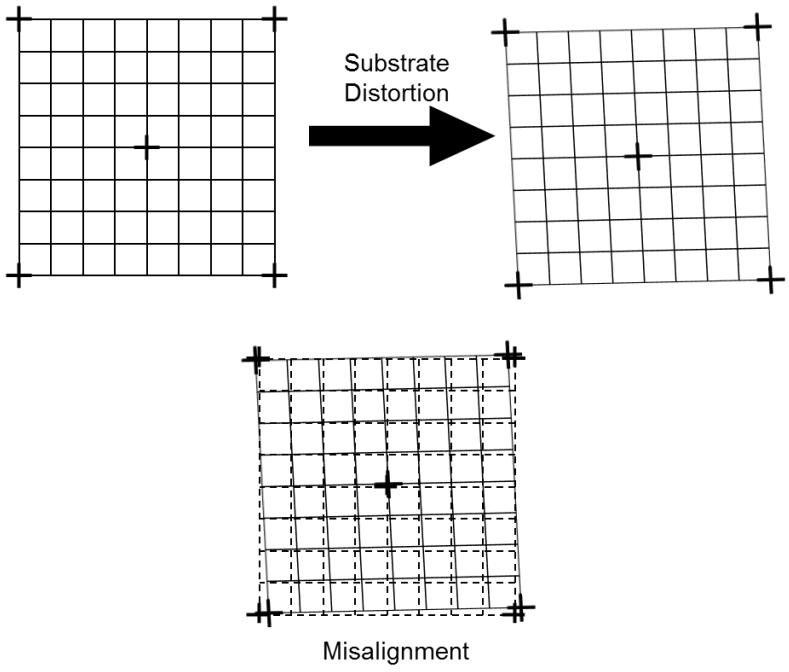

Figure 1.9: Effect of distortion of flexible or conformable substrates on layer-to-layer alignment.

1.2.3 Dual-tone photoresist

One remedy to the challenge of overlay alignment on a flexible substrate is the use of self-aligned structures that can be patterned in a single lithographic exposure step. The process is said to be self-aligned because the mask contains information sufficient to print two layers, and the alignment is done on the mask. Simultaneously imaging of two device layers minimizes the impact of substrate distortions on device overlay errors by moving control of layer-to-layer overlay error to on-mask feature alignment (or mask-to-mask alignment during the one lithographic step).

To enable the simultaneous imaging of two device layers, a photoresist capable of storing two different latent images and correctly transferring them into the substrate during subsequent etch processes is needed. Prior work on dual-tone photoresists introduced formulations capable of storing two independent images,[43, 44] but the reported systems are incompatible with the reactive ion etch processes commonly used today. The work reported in Chapter 4 involves a dual-tone photoresist system that maintains the ability to store two independent latent images, distinguished by the incident exposure light wavelength, while remaining compatible with reactive ion etch image transfer processes.

1.3 PHOTORESIST FOR MATERIALS-BASED PITCH DIVISION

1.3.1 193 nm lithography extensions

While there is steady progress towards EUV lithography, its introduction has been slowed by a number of factors, most notably the unavailability of a 13.5 nm light source powerful enough to realize throughput sufficient for economical production.[37] A number of alternative lithography solutions, including imprint lithography[45] and maskless e-beam lithography[46] are emerging as competitors (some in markets such as patterned media for

hard disk drives), but the semiconductor industry continues to rely on patterning with 193 nm sources. In addition and in conjunction with immersion lithography, there have been a number of processing approaches developed that enable reduction of the size of patterned features beyond the theoretical limit of Rayleigh's equation, a process referred to as pitch division.

Double patterning techniques, in conjunction with immersion lithography, allow for the extension of 193 nm photolithography to the 22 nm production node. Two straightforward, but capital- and time-intensive double patterning methods are litho-etch-litho-etch (LELE), and litho-freeze-litho-etch (LFLE). These both involve doing a lithographic patterning step, and either transferring the image into a hard mask (in LELE) or chemically modifying the resist to make it inert (LFLE), and then doing a second aligned lithography step before transferring via etch, as shown in Figure 1.10. Self-aligned double patterning[47], also shown in Figure 1.10, incorporates a conformal coating, which is partially etched, leaving two sidewall spacers lines for every resist line. The spacer pattern is then transferred into the resist.

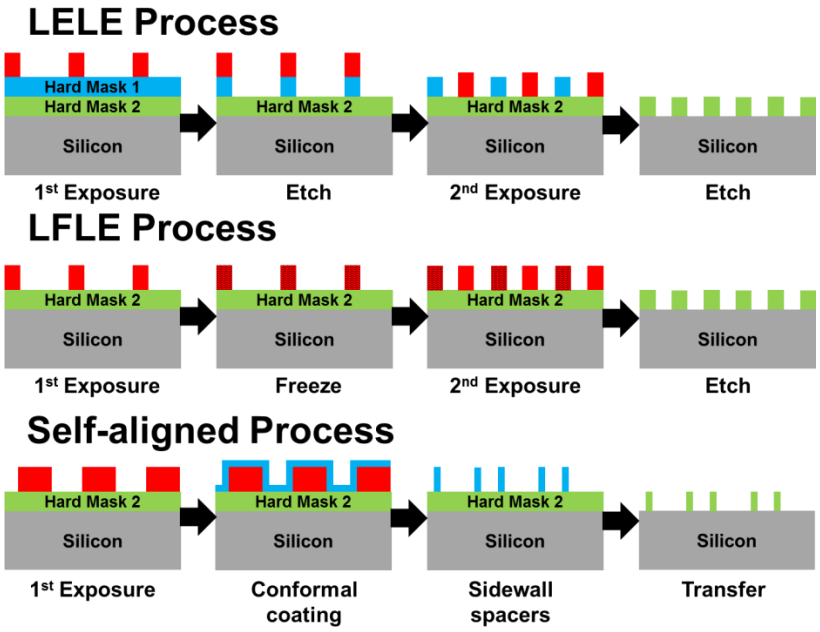

Figure 1.10: Schematic of three approaches to double patterning. The litho-etch-litho-etch (LELE) is a process in which two interspersed patterns are defined serially. The litho-freeze-litho etch involves "freezing" the resist after the first etch to make it act as a hard mask rather than a photoresist, then doing subsequent lithography and etch steps. Self-aligned double patterning is accomplished via sidewall spacers left behind after etching a conformal coating placed on top of a patterned resist.

1.3.2 Materials-based pitch division

The previously mentioned double patterning techniques, all require additional exposure or etch steps, which require costly tool time for processing. Materials-based solutions for pitch division tend to not require as much additional processing time. Dual-tone development involves developing the same resist with two different developers, one that gives a positive tone, and the other a negative tone. If the dose thresholds for dissolution are different for the two developers, it is possible to double the number of lines and spaces patterned by developing with both developers sequentially.[48] The existence of two dose thresholds for a single resist is the key characteristic that allows for

pitch division. Chapter 5 concerns a photoresist with two dose thresholds that requires only a single developer. In this pitch division photoresist, the two dissolution thresholds are a result of the reaction kinetics of the photoresist. Chapter 5 describes the optimization of pitch division photoresist formulations, kinetics characterization by NMR, and analysis of kinetics.

1.4 CHAPTER 1 REFERENCES

1. Franken, P. A.; Hill, A. E.; Peters, C. W.; Weinreich, G., Generation of Optical Harmonics. *Physical Review Letters* **1961,** 7, (4), 118-119.

2. Boyd, R. W., *Nonlinear Optics*. 3rd ed.; Elsevier: Boston, 2008.

3. Prasad, P. N.; Williams, D. J., *Introduction to Nonlinear Optical Effects in Molecules and Polymers*. John Wiley & Sons, Inc.: New York, 1991; p 307.

4. Wooten, E. L.; Kissa, K. M.; Yi-Yan, A.; Murphy, E. J.; Lafaw, D. A.; Hallemeier, P. F.; Maack, D.; Attanasio, D. V.; Fritz, D. J.; McBrien, G. J.; Bossi, D. E., A review of lithium niobate modulators for fiber-optic communications systems. *Selected Topics in Quantum Electronics, IEEE Journal of* **2000,** 6, (1), 69-82.

5. Dalton, L. R.; Sullivan, P. A.; Bale, D. H., Electric Field Poled Organic Electro-optic Materials: State of the Art and Future Prospects. *Chemical Reviews* **2009,** 110, (1), 25-55.

6. Tay, S.; Blanche, P. A.; Voorakaranam, R.; Tunc, A. V.; Lin, W.; Rokutanda, S.; Gu, T.; Flores, D.; Wang, P.; Li, G.; St Hilaire, P.; Thomas, J.; Norwood, R. A.; Yamamoto, M.; Peyghambarian, N., An updatable holographic three-dimensional display. *Nature* **2008,** 451, (7179), 694-698.

7. Zernike, F.; Midwinter, J. E., *Applied Nonlinear Optics*. Dover: New York, 2006; p 197.

8. Weis, R. S.; Gaylord, T. K., Lithium niobate: summary of physical properties and crystal structure. *Applied Physics A: Materials Science & Processing* **1985,** 37, (4), 191-203.

9. Hellwig, A. CC-BY-SA-3.0. http://en.wikipedia.org/wiki/File:Linbo3_Unit_Cell.png (31 January 2012),

10. Marder, S. R.; Perry, J. W.; Schaefer, W. P., Synthesis of organic salts with large 2nd-order optical nonlinearities. *Science* **1989,** 245, (4918), 626-628.

11. Jazbinsek, M.; Mutter, L.; Gunter, P., Photonic Applications With the Organic Nonlinear Optical Crystal DAST. *Ieee Journal of Selected Topics in Quantum Electronics* **2008,** 14, (5), 1298-1311.

12. Kuzyk, M. G., Physical Limits on Electronic Nonlinear Molecular Susceptibilities. *Physical Review Letters* **2000,** 85, (6), 1218-1221.

13. Zhou, J.; Szafruga, U. B.; Watkins, D. S.; Kuzyk, M. G., Optimizing potential energy functions for maximal intrinsic hyperpolarizability. *Physical Review A* **2007,** 76, (5), 053831.

14. Zhou, J.; Kuzyk*, M. G., Intrinsic Hyperpolarizabilities as a Figure of Merit for Electro-optic Molecules†. *The Journal of Physical Chemistry C* **2008,** 112, (21), 7978-7982.

15. Singer, K. D.; Garito, A. F., Measurements of molecular second order optical susceptibilities using dc induced second harmonic generation. *The Journal of Chemical Physics* **1981,** 75, (7), 3572-3580.

16. Clays, K.; Persoons, A., Hyper-Rayleigh scattering in solution. *Physical Review Letters* **1991,** 66, (23), 2980-2983.

17. Furukawa, T.; Johnson, G. E., Measurements of ferroelectric switching characteristics in polyvinylidene fluoride. *Applied Physics Letters* **1981,** 38, (12), 1027-1029.

18. Yongrae, R.; Varadan, V. V.; Varadan, V. K., Characterization of all the elastic, dielectric, and piezoelectric constants of uniaxially oriented poled PVDF films. *Ultrasonics, Ferroelectrics and Frequency Control, IEEE Transactions on* **2002,** 49, (6), 836-847.

19. Hilczer, B.; Kulek, J., The effect of dielectric heterogeneity on the pyroelectric response of PVDF. *Dielectrics and Electrical Insulation, IEEE Transactions on* **1998,** 5, (1), 45-50.

20. Bauer, S.; Eberle, G.; Eisenmenger, W.; Schlaich, H., Second-harmonic generation with partially poled polymers. *Optics letters* **1993,** 18, (1), 16-18.

21. Boyd, G. T.; Francis, C. V.; Trend, J. E.; Ender, D. A., Second-harmonic generation as a probe of rotational mobility in poled polymers. *J. Opt. Soc. Am. B* **1991,** 8, (4), 887-894.

22. Dalton, L. R.; Steier, W. H.; Robinson, B. H.; Zhang, C.; Ren, A.; Garner, S.; Chen, A.; Londergan, T.; Irwin, L.; Carlson, B.; Fifield, L.; Phelan, G.; Kincaid, C.; Amend, J.; Jen, A., From molecules to opto-chips: organic electro-optic materials. *Journal of Materials Chemistry* **1999,** 9, (9), 1905-1920.

23. Sullivan, P. A.; Akelaitis, A. J. P.; Lee, S. K.; McGrew, G.; Lee, S. K.; Choi, D. H.; Dalton, L. R., Novel Dendritic Chromophores for Electro-optics: Influence of Binding Mode and Attachment Flexibility on Electro-optic Behavior. *Chemistry of Materials* **2005,** 18, (2), 344-351.

24. Sullivan, P. A.; Rommel, H.; Liao, Y.; Olbricht, B. C.; Akelaitis, A. J. P.; Firestone, K. A.; Kang, J.-W.; Luo, J.; Davies, J. A.; Choi, D. H.; Eichinger, B. E.; Reid,

P. J.; Chen, A.; Jen, A. K. Y.; Robinson, B. H.; Dalton, L. R., Theory-Guided Design and Synthesis of Multichromophore Dendrimers: An Analysis of the Electro-optic Effect. *Journal of the American Chemical Society* **2007,** 129, (24), 7523-7530.

25. Williams, M. L.; Landel, R. F.; Ferry, J. D., The Temperature Dependence of Relaxation Mechanisms in Amorphous Polymers and Other Glass-forming Liquids. *Journal of the American Chemical Society* **1955,** 77, (14), 3701-3707.

26. Dureiko, R. D.; Schuele, D. E.; Singer, K. D., Modeling relaxation processes in poled electro-optic polymer films. *J. Opt. Soc. Am. B* **1998,** 15, (1), 338-350.

27. Singer, K. D.; Kuzyk, M. G.; Holland, W. R.; Sohn, J. E.; Lalama, S. J.; Comizzoli, R. B.; Katz, H. E.; Schilling, M. L., Electro-optic phase modulation and optical second-harmonic generation in corona-poled polymer films. *Applied Physics Letters* **1988,** 53, (19), 1800-1802.

28. Benight, S. J.; Johnson, L. E.; Barnes, R.; Olbricht, B. C.; Bale, D. H.; Reid, P. J.; Eichinger, B. E.; Dalton, L. R.; Sullivan, P. A.; Robinson, B. H., Reduced Dimensionality in Organic Electro-Optic Materials: Theory and Defined Order. *The Journal of Physical Chemistry B* **2010,** 114, (37), 11949-11956.

29. Hubbard, M. A.; Marks, T. J.; Yang, J.; Wong, G. K., Poled polymeric nonlinear optical materials. Enhanced second harmonic generation stability of crosslinkable matrix/chromophore ensembles. *Chemistry of Materials* **1989,** 1, (2), 167-169.

30. Association, S. I. Global Semiconductor Sales Hit Record $298.3 Billion in 2010. http://www.sia-online.org/news/2011/01/31/global-sales-reports-2011/global-semiconductor-sales-hit-record-298.3-billion-in-2010/

31. Moore, G. E., Cramming more components onto integrated circuits. *Proceedings of the IEEE* **1998,** 86, (1), 82-85.

32. Van Look, L.; Bekaert, J.; Truffert, V.; Wiaux, V.; Lazzarino, F.; Maenhoudt, M.; Vandenberghe, G.; Reybrouck, M.; Tarutani, S. In *Printing the metal and contact layers for the 32- and 22-nm node: comparing positive and negative tone development process*, San Jose, California, USA, 2010; Dusa, M. V.; Conley, W., Eds. SPIE: San Jose, California, USA, 2010; pp 764011-12.

33. Burnett, J. H.; Benck, E. C.; Kaplan, S. G.; Sirat, G. Y.; Mack, C. In *Birefringence issues with uniaxial crystals as last lens elements for high-index immersion lithography*, 2009; 2009; p 727421.

34. Liberman, V.; Rothschild, M.; Palmacci, S.; Bristol, R.; Byers, J.; Turro, N.; Lei, X.; O'Connor, N.; Zimmerman, P. In *High-index immersion lithography: preventing lens photocontamination and identifying optical behavior of LuAG*, 2008; 2008; p 692416.

35. Matsumoto, K.; Costner, E. A.; Nishimura, I.; Ueda, M.; Willson, C. G., High Index Resist for 193 nm Immersion Lithography. *Macromolecules* **2008,** 41, (15), 5674-5680.

36. Taylor, J. C.; Costner, E. A.; Goh, S.; Wojtczak, W.; Dewulf, D.; Willson, C. G., The effect of added salts on the optical properties of water for high index immersion lithography fluids. *Journal of Vacuum Science & Technology B: Microelectronics and Nanometer Structures* **2008,** 26, 506.

37. Wagner, C.; Harned, N., EUV lithography: Lithography gets extreme. *Nat Photon* **2010,** 4, (1), 24-26.

38. Huang, M.; Zhao, F.; Cheng, Y.; Xu, N.; Xu, Z., Large area uniform nanostructures fabricated by direct femtosecond laser ablation. *Opt. Express* **2008,** 16, (23), 19354-19365.

39. Arias, A. C.; MacKenzie, J. D.; McCulloch, I.; Rivnay, J.; Salleo, A., Materials and Applications for Large Area Electronics: Solution-Based Approaches. *Chemical Reviews* **2010,** 110, (1), 3-24.

40. Ahn, S. H.; Guo, L. J., Large-Area Roll-to-Roll and Roll-to-Plate Nanoimprint Lithography: A Step toward High-Throughput Application of Continuous Nanoimprinting. *ACS Nano* **2009,** 3, (8), 2304-2310.

41. Cheng, I. C.; Kattamis, A.; Long, K.; Sturm, J. C.; Wagner, S., Stress control for overlay registration in a Si: H TFTs on flexible organic polymer foil substrates. *Journal of the Society for Information Display* **2005,** 13, 563.

42. Jain, K.; Klosner, M.; Zemel, M.; Raghunandan, S., Flexible Electronics and Displays: High-Resolution, Roll-to-Roll, Projection Lithography and Photoablation Processing Technologies for High-Throughput Production. *Proceedings of the IEEE* **2005,** 93, (8), 1500-1510.

43. Hinsberg, W. D.; MacDonald, S. A.; Pederson, L. A.; Willson, C. G., A lithographic analog of color photography: self-aligning photolithography using a resist with wavelength-dependent tone. *Journal of Imaging Science* **1989,** 33, (4), 129-35.

44. Hinsberg, W. D.; Pederson, L. A.; Willson, C. G. In *Zero-misalignment Lithographic Process Using a Photoresist with Wavelength-selected tone*, Advances in resist technology and processing V, Santa Clara, California, 29 February-2 March, 1988; MacDonald, S. A., Ed. SPIE: Santa Clara, California, 1988; pp 2-12.

45. Wilson, C. G., A Decade of Step and Flash Imprint Lithography. *Journal of Photopolymer Science and Technology* **2009,** 22, (2), 147-153.

46. Chen, J. J. H.; Lin, S.; Fang, T.; Chang, S.; Krecinic, F.; Lin, B. J. In *Multiple electron beam maskless lithography for high-volume manufacturing*, 2009; IEEE: 2009; pp 96-97.

47. Finders, J.; Dusa, M.; Vleeming, B.; Megens, H.; Hepp, B.; Maenhoudt, M.; Cheng, S.; Vandeweyer, T. In *Double patterning for 32nm and below: an update*, San Jose, CA, USA, 2008; Levinson, H. J.; Dusa, M. V., Eds. SPIE: San Jose, CA, USA, 2008; pp 692408-12.

48. Fonseca, C.; Somervell, M.; Scheer, S.; Printz, W.; Nafus, K.; Hatakeyama, S.; Kuwahara, Y.; Niwa, T.; Bernard, S.; Gronheid, R. In *Advances and challenges in dual-tone development process optimization*, San Jose, CA, USA, 2009; Levinson, H. J.; Dusa, M. V., Eds. SPIE: San Jose, CA, USA, 2009; pp 72740I-12.

Chapter 2: Measurement of second-order nonlinear optical properties

2.1 INTRODUCTION

Due to the complexity of fabrication of integrated optics devices incorporating NLO materials, it is desirable to evaluate the fundamental NLO properties of materials to determine their suitability for NLO devices. The most accessible second-order nonlinear phenomena are second harmonic generation and the electro-optic (EO) effect. The magnitudes of both of these effects are proportional to the appropriate nonlinear optical coefficients.

A major goal of the present research is to find NLO materials that exhibit high NLO coefficients that are stable at elevated temperatures. EO coefficients are particularly relevant for polymer materials, since they determine device characteristics like the modulator length and half-wave voltage. The EO coefficient can be determined using an attenuated total reflection method incorporating a prism coupler, as described below. The prism coupler method is also capable of quickly determining the NLO polymer's linear optical properties (i.e. index of refraction) and thickness, so it is convenient to extend this method to allow for measurement of EO coefficients.

SHG is a convenient method for tracking the real-time poled order of an NLO polymer film, both during poling and after poling. Measurement of SHG as a function of time for elevated temperatures characterizes the thermal stability of NLO properties. For characterization of stability of NLO properties, SHG analysis can be carried out in a relative fashion, i.e., relative to an initial or final value. With care, however, SHG can be normalized to an inorganic standard with known SHG coefficients to obtain SHG coefficients for the polymer. SHG and EO coefficients at various wavelengths can be compared by employing dispersion models such as a two-level model. The determination of SHG coefficients and EO coefficients are discussed below.

2.2 SECOND HARMONIC GENERATION COEFFICIENTS

The measurement of second harmonic generation coefficients of poled polymers is straightforward but requires care in order to extract the desired data. A simplified scheme for the measurement is shown in Figure 2.1. The source is a near-infrared Q-switched pulsed laser source which is focused on a rotation stage. After the polarized light passes through the sample, light at the original wavelength is filtered out with a band-pass filter. After passing through another polarizer, the light is collected with a photomultiplier tube. Because the light is pulsed, a boxcar integrator is used to collect the intensity data, which is fed to a computer.

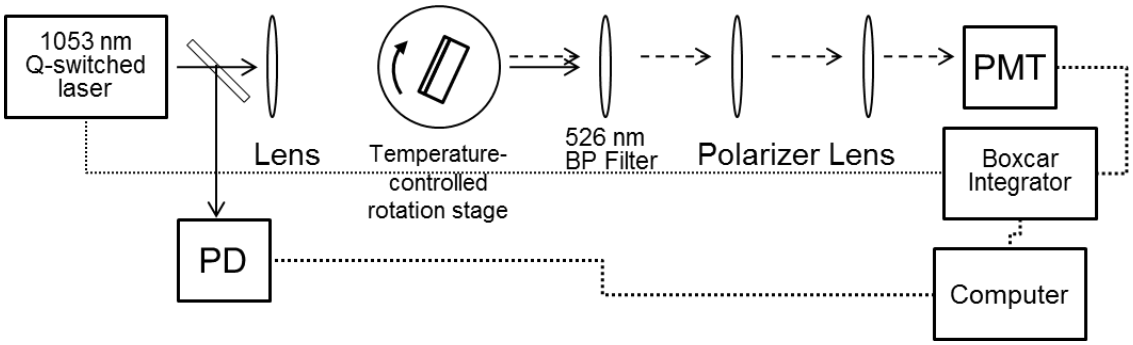

Figure 2.1: Experimental setup for measurement of second harmonic generation coefficients for poled polymers.

In order to determine nonlinear optical coefficients for a thin film, the wave equation that is derived from Maxwell's relations must be adapted to account for second harmonic generation. Typically, in deriving the wave equation for optical materials, the relative magnetic permeability is assumed to be unity and the electric susceptibility is captured in terms of the index of refraction and absorption of the material. For second-order materials, however, the nonlinear polarization is included in the wave equation by splitting the polarization into linear and nonlinear terms as follows:

$$\boldsymbol{P} = \chi^{(1)}\boldsymbol{E} + \chi^{(2)}\boldsymbol{EE} + \cdots \equiv \boldsymbol{P}^{(1)} + \boldsymbol{P}^{\mathrm{NL}} \qquad 2.1$$

The linear term is carried through in terms of index of refraction and absorbance, while the nonlinear term generates an additional source term on the right hand side of the wave equation:

$$\nabla^2 \mathbf{E}_n(\mathbf{r}) - \nabla(\nabla \cdot \mathbf{E}_n(\mathbf{r})) + \frac{\omega_n^2}{c^2} \boldsymbol{\epsilon}^{(\mathbf{1})}(\omega_n) \cdot \mathbf{E}_n(\mathbf{r}) = -\frac{\omega_n^2}{\epsilon_0 c^2} \mathbf{P}_n^{\mathrm{NL}}(\mathbf{r}) \qquad 2.2$$

Additionally, the new wave equation applies for every frequency ω_n, so the equation must be solved for the fundamental as well as the second harmonic. In the above equation, ϵ_0 is the vacuum permittivity, $\boldsymbol{\epsilon}^{(\mathbf{1})}$ is the relative permittivity tensor, and c is the speed of light. The solution to the equation can be expressed as plane waves with amplitudes that vary in the NLO active regions. At each interface, there are reflected and transmitted rays of both the fundamental and second harmonic. The boundary conditions at the interfaces are determined by employing the continuity equation as well as the law of energy conservation, and lead to nonlinear analogues of the Fresnel equations and Snell's law.

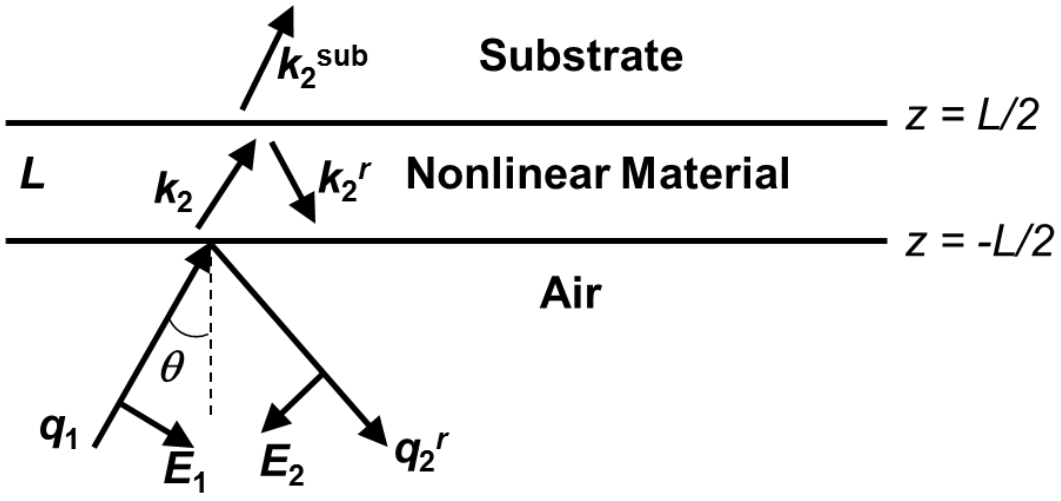

Figure 2.2: Diagram of wavevectors (k and q) as well as electric field vectors (E) for second harmonic generation in a thin NLO film on a substrate (*p*-polarized incidence shown). The index $n = [1,2]$ refers to the fundamental (1) or second-harmonic (2) frequency, and only the 2nd harmonic is shown inside the NLO material and substrate.

Finally, Equation 1.1 is an equation in three dimensions, so the directionality of the electric field and the spatial symmetry of the materials must also be accounted for. Accordingly, the polarization of the light with respect to the plane of incidence can be either transverse electric (TE, or *s*-polarized) or transverse magnetic (TM, or *p*-polarized). In the case of poled polymers, the direction of poling is perpendicular to the substrate plane. For *p*-polarized light, the poling birefringence causes a slight "walk-off" angle between the wave propagation and the Poynting vector, which is the direction of energy flow.

Jerphagnon and Kurtz first reported a solution for the SHG wave equation for uniaxial crystals,[1] but they made inadequate assumptions regarding the boundary conditions and dispersion that were later corrected by Herman and Hayden.[2] The Herman and Hayden (HH) method considers the incident fundamental ray, the reflected second

harmonic, the transmitted and back-reflected second harmonics, and the second harmonic transmitted to the substrate as shown in Figure 2.2. A partial explanation of the SHG wave equation and its solution is found in Appendix A.

2.2.1 Solution of SHG equation and angle dependence

Since poled polymer materials are dispersive, the amplitude of the emerging second harmonic depends strongly on the angle of incidence and thickness of the NLO material. Although closed-form solutions are obtainable, they are somewhat unwieldy. Park and Herman give closed-form solutions which take into account multiple reflections of both the fundamental and second-harmonic in multilayer stacks including a single NLO layer. The transmission coefficient for the second harmonic is represented by the following expression due to Park and Herman[3]:

$$
\begin{aligned}
&t_{a\to S}^{(\eta\to p)} \\
&= -e^{-2ik_0 n_{2s} c_{2s}(L+d_T)} \frac{4\pi i k_0 L}{n_{2f} c_{\gamma_2} c_{2-\gamma}} \left[\frac{t_{a\to S}^{(1\eta)} E_{1a}}{t_{f\to S}^{(1\eta)}}\right]^2 \frac{t_{a\to S}^{(2p)}}{t_{a\to f}^{(2p)}} \\
&\times \left\{ \begin{array}{l} d_{eff}^{(\eta\to p)} \left[e^{-i\Phi^{(\eta\to p)}} + r_{f\to a}^{(2p)} \left(r_{f\to S}^{(1\eta)}\right)^2 e^{i\Phi^{(\eta\to p)}}\right] \mathrm{sinc}\left(\Psi^{(\eta\to p)}\right) \\ + d_{eff}^{r(\eta\to p)} \left[\left(r_{f\to S}^{(1\eta)}\right)^2 e^{i\Psi^{(\eta\to p)}} + r_{f\to a}^{(2p)} e^{-i\Psi^{(\eta\to p)}}\right] \mathrm{sinc}\left(\Phi^{(\eta\to p)}\right) \end{array} \right\}
\end{aligned}
\qquad 2.3
$$

The transmission coefficient of Equation 2.3 relates the intensity of *p*-polarized second harmonic light in the substrate to the intensity of either *s*- or *p*-polarized fundamental light impinging on the sample. The total transmitted SHG power is given by:[3]

$$P_{2\omega} = \frac{\epsilon_0 c}{2} \left(t_{Sa}^{(2p)}\right)^2 \left|t_{a\to S}^{(\eta\to p)}\right|^2 A_{\mathrm{cross}} \qquad 2.4$$

where $t_{Sa}^{(2p)}$ is the Fresnel transmission coefficient of the *p*-polarized SH from the substrate to air and A_{cross} is the cross-sectional area of the fundamental beam. Superscripts refer to the fundamental or second harmonic (1 and 2, respectively) and to the polarization, while subscripts refer to the layer (*a*, *f*, and *S* for air, film, and substrate, respectively).

The terms in Equations 2.3 and 2.4 are described in Table 2.1. The angle dependence can be thought of as being due to three components. First, in order to conserve momentum, SHG processes must satisfy the phase matching condition. For dispersive materials that are not phase-matched by matching the index of refraction (via angle tuning or temperature tuning of birefringence), the SHG power will oscillate with optical path length as the phase mismatch increases and decreases. As the angle of incidence changes, the path length changes monotonically, so the amplitude of SHG oscillates with increasing angle. The number of oscillations increases with the index mismatch and with the sample thickness as shown in Figure 2.3. For films that are thick compared to the coherence length (the product of wavelength and index mismatch), the phase mismatch is much more important. In addition to phase mismatch, there is angle dependence due to transmission and reflection coefficients. Transmission falls off with increasing angle of incidence and is dependent on polarization.

Table 2.1: Description of the terms in Equations 2.3 and 2.4. A full explanation of terms is available in [3].

Term	Description	Contribution to θ-dependence of SHG
$t_{a\to S}^{(\eta\to p)}$	Analog of transmission coefficient for SHG (not unitless, because of nonlinearity)	
$t_{Sa}^{(2p)}$	Transmission coefficient for second harmonic from substrate to air	Falls off as $\theta\to$critical angle
$e^{-2ik_0 n_{2s} c_{2s}(L+d_T)}$	Phase term for boundary condition matching at substrate, no contribution to amplitude if substrate is lossless	None
$\frac{4\pi i k_0 L}{n_{2f} c_{\gamma_2} c_{2-\gamma}}$	Interaction path length	Significant effect on shape of envelope
$\left[\frac{t_{a\to S}^{(1\eta)} E_{1a}}{t_{f\to S}^{(1\eta)}}\right]^2 \frac{t_{a\to S}^{(2p)}}{t_{a\to f}^{(2p)}}$	Transmission coefficients for fundamental into the NLO region and SHG out of the substrate. Also contains the fundamental field strength and contributions due to multiple reflections	Small effect on shape of envelope
$d_{eff}^{(\eta\to p)}$, $d_{eff}^{r(\eta\to p)}$	"Effective" SHG coefficient: describes components of SHG coefficient tensor that overlap with electric field of incident and reflected fundamental	Primary determinant of envelope shape
$\left[e^{-i\Phi^{(\eta\to p)}} + r_{f\to a}^{(2p)} \left(r_{f\to S}^{(1\eta)}\right)^2 e^{i\Phi^{(\eta\to p)}}\right]$	Multiple reflections of both the fundamental and SHG waves	Only for multiple reflections
$\mathrm{sinc}\left(\Psi^{(\eta\to p)}\right)$ $\mathrm{sinc}\left(\Phi^{(\eta\to p)}\right)$	Phase matching terms that arise from conservation of momentum. Ψ, Φ describe phase mismatch between fundamental and SHG in co- and counter-directional waves, respectively.	Modulation of envelope dependent on thickness and index mismatch (Figure 2.3)

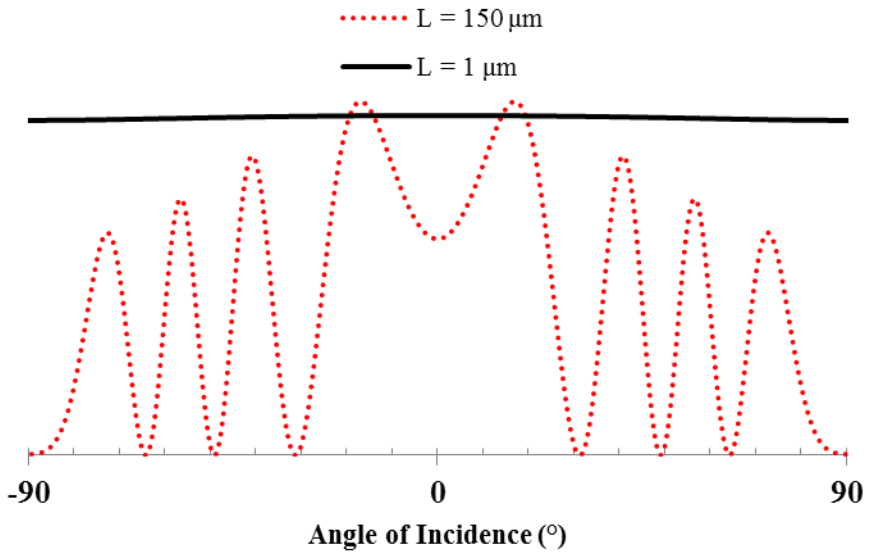

Figure 2.3: Effect of phase mismatch on angle dependence of SHG power (arbitrary units) for an NLO material with $n_1 = 1.5$, $n_2 = 1.54$, $\lambda = 1.064$ μm for thicknesses of 150 μm and 1 μm. Note that the two plots are scaled differently to allow comparison of shape.

The third source of angle dependence is due to the directionality of the nonlinear optical coefficients. Second-order NLO coefficients are expressed as second rank tensors, with indices specifying the direction of the electric field for both input fundamentals (they need not be the same) and the output SHG direction, for a total of 27 elements. For SHG, this number is reduced to 18, since the two inputs are of identical frequency. SHG coefficients are usually specified in a 3×6 matrix with the second of the two indices specifying one of six combination of input directions (*xx*, *yy*, *zz*, *yz*, *xz*, *xy*) relative to the poling axis (designated the *z*-axis). The symmetry of the NLO material further reduces the independent nonzero elements, and tables of symmetry specify the SHG coefficient matrices for materials of different space groups.[4] For poled polymers, the symmetry of the $C_{\infty v}$ (∞mm point group) applies, as shown below:

$$\boldsymbol{d} = \begin{bmatrix} 0 & 0 & 0 & 0 & d_{15} & 0 \\ 0 & 0 & 0 & d_{15} & 0 & 0 \\ d_{31} & d_{31} & d_{33} & 0 & 0 & 0 \end{bmatrix} \quad 2.5$$

When Kleinman symmetry applies (as is assumed to be the case for the polymers discussed herein), $d_{15} = d_{31}$, so there are only two independent elements, d_{31} and d_{33}.

The SHG output depends on the effective SHG coefficient, d_{eff}, which is determined by the angle between the poling axis and the incident fundamental light. The effective SHG coefficient is:

$$d_{eff} = -\hat{\boldsymbol{e}}_2 \cdot \boldsymbol{d} \cdot \hat{\boldsymbol{e}}_{\mathbf{11}} \quad 2.6$$

In this equation, $\hat{\boldsymbol{e}}_2$ is the unit vector of the SH electric field while $\hat{\boldsymbol{e}}_{\mathbf{11}}$ is a combination of two unit vectors of the incident electric field. The vectors depend on the polarization and the incident angle as follows:

$$\hat{\boldsymbol{e}}_2^p = [\cos\theta_1 \quad 0 \quad -\sin\theta_1] \; p\text{-polarization}$$

$$\hat{\boldsymbol{e}}_2^p = [0 \quad 1 \quad 0] \; s\text{-polarization}$$

$$\hat{\boldsymbol{e}}_{11}^{pp} = \begin{bmatrix} \cos^2\theta_1 \\ 0 \\ \sin^2\theta_1 \\ 0 \\ -2\sin\theta_1\cos\theta_1 \\ 0 \end{bmatrix}, \; \hat{\boldsymbol{e}}_{11}^{ss} = \begin{bmatrix} 0 \\ 1 \\ 0 \\ 0 \\ 0 \\ 0 \end{bmatrix} \quad 2.7$$

Applying Equation 1.6 to *p*-polarization of both the fundamental and SHG waves, we obtain the following (for Kleinman conditions):

$$d_{eff}^{p\to p} = d_{31}\sin 2\theta_1 \cos\theta_2 + \sin\theta_2 \left(d_{31}\cos^2\theta_1 + d_{33}\sin^2\theta_1\right) \quad 2.8$$

Importantly, Equation 2.8 implies that the SHG power output for p-to-p polarization is dependent on two independent SHG coefficients. In order to back out SHG

coefficients from power measurements, it is necessary to measure other polarization combinations. For other polarizations:

$$d_{eff}^{s\to p} = d_{31}\sin\theta_2$$
$$d_{eff}^{s\to s} = 0 \qquad 2.9$$
$$d_{eff}^{p\to s} = 0$$

Equation 2.9 shows that measuring the *s*-polarized SHG output is fruitless as no SHG is produced. Measurement of the s-to-p combination allows calculation of d_{31}, which can then be used to compute d_{33}. Thus, the most convenient way to measure d_{31} and d_{33} is to measure s-to-p and p-to-p polarizations. The shape of the contribution of d_{eff} is shown in Figure 2.4. In order to fit the SHG coefficients properly, it was necessary to properly account for the angular dependence from the Maker fringe and transmission coefficients. In order to do this, the thickness, refractive index, and absorbance of all optical layers were determined. The substrate was characterized by spectroscopic ellipsometry, and the poled NLO film was characterized by prism coupling, as described in Section 2.3.1.

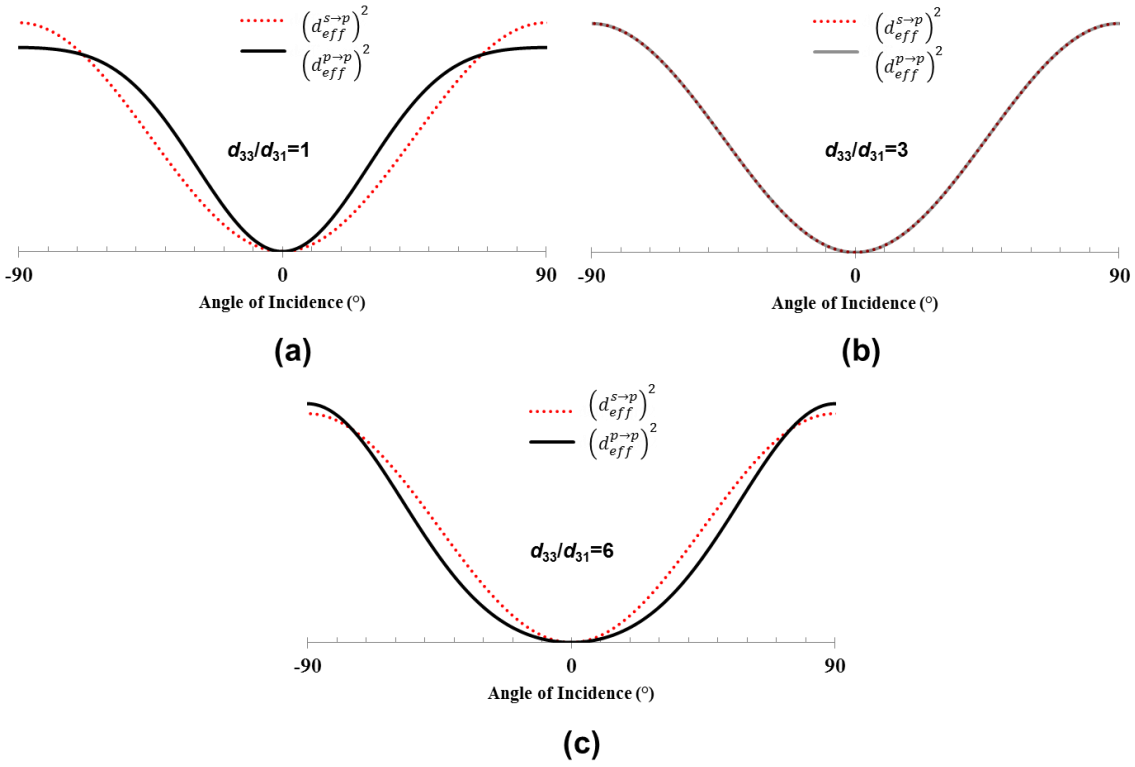

Figure 2.4: A comparison of the shape of the contribution (in arbitrary units) from effective SHG coefficients, assuming no dispersion. The d_{33}/d_{31} ratio is assumed to be 1 (a), 3 (b), or 6 (c). Note that in each case, the $s\rightarrow p$ plots have been scaled up relative to $p\rightarrow p$ in order to show shape differences. For (b), the scale factor is equal to $(d_{33}/d_{31})^2$=9.

2.2.2 Normalization to quartz

The intensity of SHG output is proportional to the square of input fundamental intensity, so in order to accurately compute d_{33} and d_{31}, the fundamental must be measured. In addition, absorption and reflection in the lenses, polarizers, and filters must also be accounted for. The most straightforward way to do this is to use an inorganic NLO crystal with known SHG coefficients as a calibration standard. The calibration can be done with two equivalent optical paths and detectors for the sample and the SHG standard, but, in this work, we first measured both the fundamental and SH for the NLO

crystal standard and then replaced the standard with the NLO polymer. Care was taken to ensure that both samples were placed at the beam waist, and that reflection and transmission coefficients were appropriately accounted for.

Crystalline quartz is a common standard for calibration of SHG measurements. A sample of X-cut crystalline quartz (MTI Corp.) was used in the present experiments. Quartz has the following SHG coefficients:[4]

$$\tilde{\boldsymbol{d}} = \begin{bmatrix} d_{11} & -d_{11} & 0 & d_{14} & 0 & 0 \\ 0 & 0 & 0 & 0 & -d_{14} & -d_{11} \\ 0 & 0 & 0 & 0 & 0 & 0 \end{bmatrix} \qquad 2.10$$

These coefficients are relative to the crystal axis of quartz (3 refers to the Z-axis); however, in order to use Equation 2.3 it is convenient to rewrite the coefficient in terms of the coordinates given in Figure 2.1:

$$\begin{matrix} X \to z \\ Y \to x \\ Z \to y \end{matrix} \quad \begin{matrix} 1 \to 3 \\ 2 \to 1 \\ 3 \to 2 \\ 4 \to 6 \\ 5 \to 4 \\ 6 \to 5 \end{matrix} \qquad 2.11$$

This leads to the following SHG matrix:

$$\tilde{\boldsymbol{d}} = \begin{bmatrix} 0 & 0 & 0 & -d_{14} & -d_{11} & 0 \\ 0 & 0 & 0 & 0 & 0 & 0 \\ -d_{11} & 0 & d_{11} & 0 & 0 & d_{14} \end{bmatrix} \qquad 2.12$$

According to supplier tabulations, for X-cut quartz, $d_{11} = 0.46$ pm/V and $d_{11} < 0.01$ pm/V, although there are large variations among reported values based on the method used.[5] Neglecting d_{11}, the effective SHG coefficients for *p*-to-*p* and *s*-to-*p* propagation are, respectively,

$$\begin{aligned} d_{eff}^{p \to p} &= -d_{11} \sin(\theta_2 + 2\theta_1) \\ d_{eff}^{s \to p} &= 0 \end{aligned} \qquad 2.13$$

Hence, it is sufficient to make only either *p*-to-*p* or *s*-to-*p* measurements. It is also important to note that X-cut quartz must be appropriately oriented so that the crystal axis is transverse to the direction of propagation of light.

2.2.3 Experiment

The beam path for the SHG experiment is shown in Figure 2.1. The low-power IR laser source is a Nd:YLF Q-switched 500 mW diode-pumped solid state pulsed laser (Lightwave Electronics Series 110) with *s*-polarized output at 1053 nm. The pulse rate is 2 kHz with <7 ns pulse duration. The beam was split by a quartz (amorphous) window, and the partial reflection was returned to a Si photodiode (UDT Instruments) for fundamental intensity measurement. The transmitted beam was focused on the sample, and the output passes through a 523 nm bandpass filter (Andover) and a polarizer (*p*-transmission), where it is then focused onto the detector, a PMT module (Hamamatsu) located behind a second short pass filter. An annotated photograph of the experiment setup is shown in Figure 2.5.

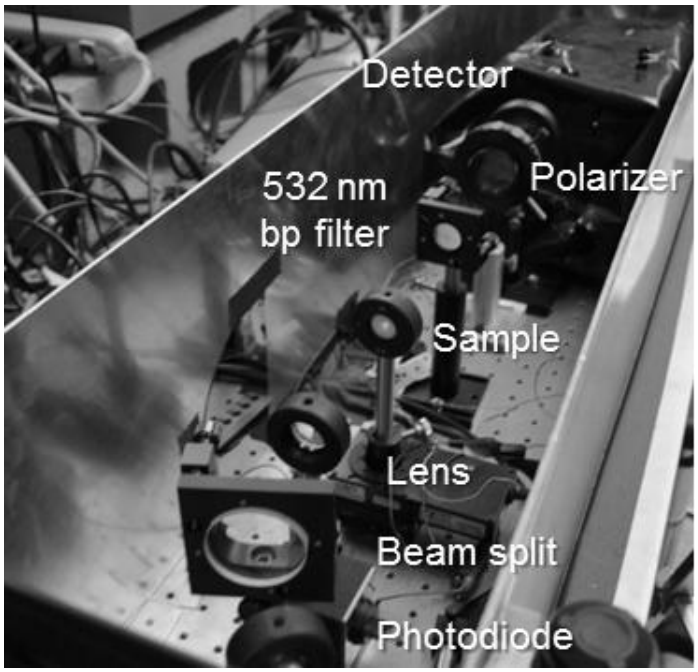

Figure 2.5: Annotated photograph of SHG experiment setup

In order to produce laser peak power large enough to easily measure SHG, the laser was Q-switched at 200 kHz. A gated (boxcar) integrator was employed to isolate the pulse amplitude. The custom built gated integrator was assembled from standard solid state components according to literature descriptions that allows for subtraction of the baseline (nonpulse background) signal.[6-8] The pulse gate was defined by a digital signal sent from the Q-switch to a computer that generates digital gate integration and reset pulses using LabVIEW software (National Instruments). The integrator circuit integrates and stores the signal from the integration pulse until the time of the reset pulse just before the next laser pulse. National Instruments data acquisition analog-to-digital converters measure the integrated value of SHG pulses. Since the fundamental signal is much stronger than the SHG signal and the pulse-to-pulse stability is sufficient, the fundamental intensity is time-averaged via a Si photodetector and a transimpedance

amplifier with a response time that is long compared to the pulse duration, allowing for a stable intensity input.

A LabVIEW virtual instrument (VI) controlled the generation of digital pulses for integration. Another VI automates the collection of the integrated intensity, averaging 500 pulses for each data point, and automates the rotation of the sample stage (Newport), which rotates through discrete angles between data collections. In addition, for elevated temperature studies of polymer samples, the temperature of the sample is controlled via a heater mounted on the sample stage.

In the case of quartz, multiple reflections of fundamental and SHG light are neglected since the crystal thickness of 300 μm is much larger than the size of the focused beam and the coherence length of the NLO interaction. The transmission coefficients are computed with the Fresnel formulae,[9] using the index of refraction of single-crystal quartz at both the fundamental and second harmonic wavelengths. The rotation axis of the quartz crystal must be carefully aligned with the fundamental beam to prevent asymmetry of the fringes, which interfere with proper fitting.

Prior to collection of data, the background fundamental and SHG signals with the beam blocked were recorded and later subtracted from the intensities. The corrected SHG intensity divided by the square of the fundamental intensity was computed and fit. For quartz, a three- or four-parameter fit were used, as the dispersion, or the difference in the index of quartz at the fundamental and second harmonic, is a more determinative parameter on the shape of the data than either individual index of refraction. The other fit parameters were the thickness of the quartz and the calibration factor f, which accounts for experimental factors that are independent of the sample, such as sensitivity of the detectors, beam area at the beam waist, amplifier gains, absorption and reflection of optics, and the constants.

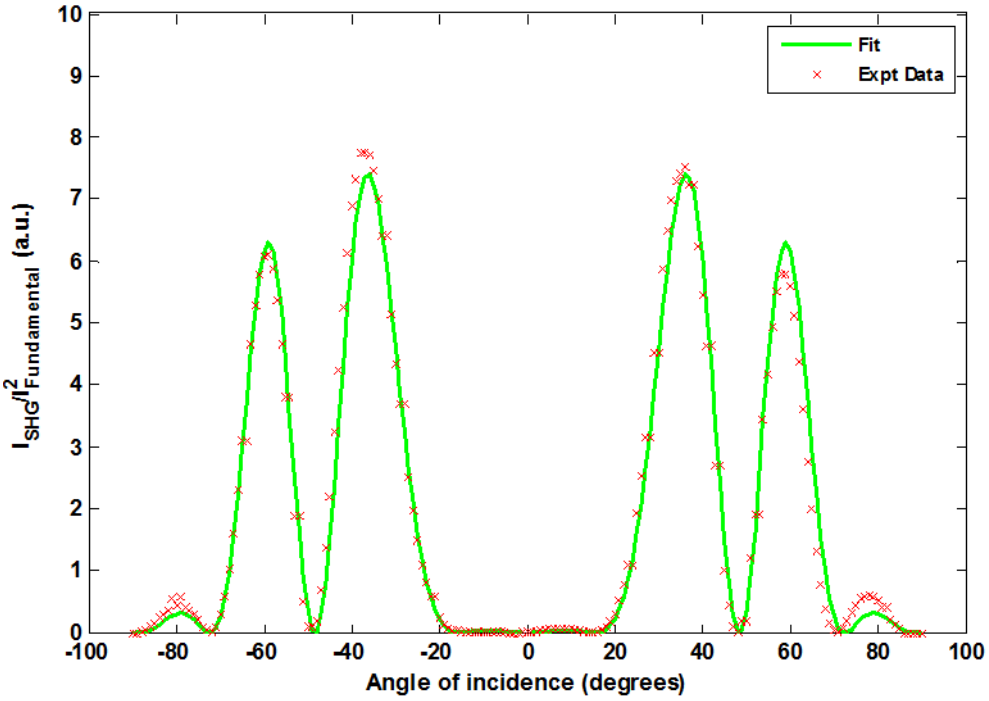

Figure 2.6: SHG power divided by the square of fundamental power vs. incident angle for p-to-p SHG of X-cut quartz. A fit of the data results in estimates for the index of refraction and thickness (nominally 300 μm) and the calibration factor that is used for computation of SHG coefficients for NLO polymers. Fit values are: f=0.033 (calibration factor), n(1053 nm) = 1.5429 , n(526 nm) = 1.5562, L= 312 μm.

Figure 2.6 shows a plot of SHG intensity divided by the square of fundamental intensity for X-cut quartz. The data was fitted with the MATLAB (The MathWorks, Inc.) Curve Fitting Toolbox routine *nlinfit* using a Gauss-Newton algorithm, giving index values of $n_{1053\text{nm}}$ = 1.5429 and $n_{526\text{nm}}$ = 1.5562, a thickness of L = 312 μm, and a calibration factor of f = 0.078. For these fits, absorption, birefringence, and multiple reflections were neglected. The value of f was then used to compute the SHG coefficients for polymer films.

2.2.4 SHG Coefficients of NLO poled polymers

Nonlinear optical polymers were spin coated onto an indium tin oxide-coated (ITO-coated) glass substrate, allowing for application of an electric field across the polymer during poling. Immediately following poling, NLO polymers are mounted on a rotation stage and SHG intensity is measured as a function of angle by rotating the sample. A typical SHG intensity curve for *s*-to-*p* and *p*-to-*p* transmission is shown in Figure 2.7 for a corona-poled non-crosslinkable tolane polymer (synthesis and characterization details as well as poling are discussed in Chapter 3). The fundamental intensity input and the lens alignment must be adjusted to prevent damage of the film (shown in Figure 2.8), which destroys the illuminated areas and leads to transient emission of broadband visible light, some of which enters the detector and interferes with the measurement.

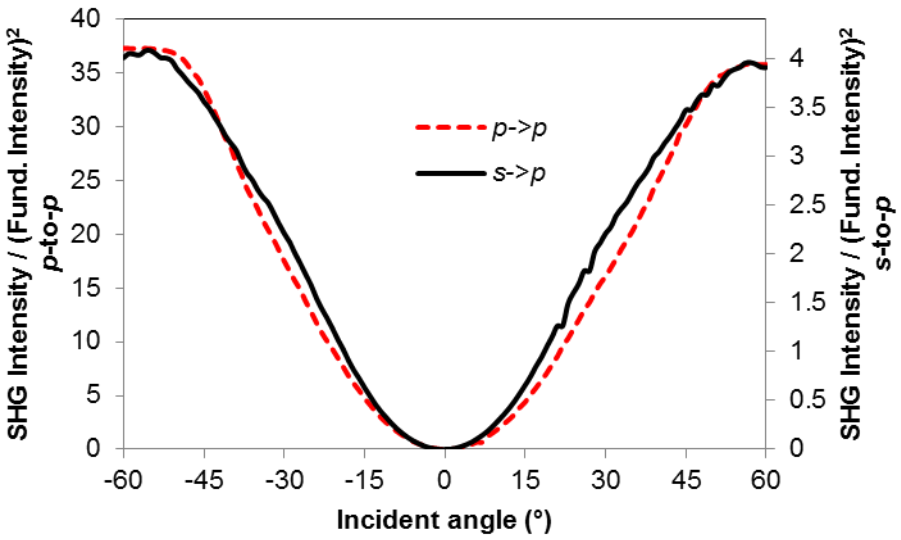

Figure 2.7: SHG Intensity data for a corona-poled NLO polymer for *p*-to-*p* and *s*-to-*p* transmission.

The data for Figure 2.7 were fit to the model specified by Equation 2.3, greatly simplified by a number of assumptions. First, we neglect absorption of the fundamental

and second harmonic since the wavelength of maximum absorption for the polymers of interest is around 400 nm, well below the 526 nm of the second harmonic. For polymers with more active chromophores, however, absorption must be taken into account. Also neglected is birefringence, which can be accounted for by measuring the ordinary and extraordinary indices of refraction (see below). A three-layer model of air-film-substrate (glass) was also assumed, although it can be extended by including the ITO layer optical constants.[10] Finally, multiple reflections of the second harmonic and fundamental were neglected, although analysis of reflections of SH shows that the contribution of SH reflection is minimal in the case of thin polymer films.

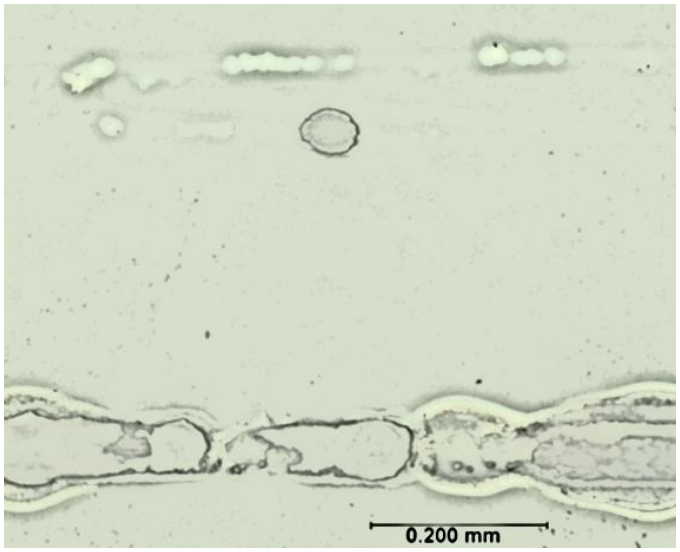

Figure 2.8: Micrograph of NLO polymer film damage by fundamental beam. Film damage was accompanied by a transient visible glow of the sample that interferes with the measurement.

The dispersion was measured via spectroscopic ellipsometry (JA Woollam) of a sample of the non-crosslinkable polymer on silicon using a Cauchy model for the index of refraction. The dispersion was measured on the unpoled sample and is assumed to be

independent of poling-induced birefringence. The M-2000 ellipsometer spectrum extends to 1000 nm, so the index at 1053 nm was extrapolated using the Cauchy fit, giving an index of 1.619 at 1053 nm and 1.669 at 523 nm. The remaining parameters are the SHG coefficients and the film thickness. The *s*-to-*p* transmittance was fitted first, using the calibration factor from quartz, yielding a d_{31} of 4.4 pm/V and a film thickness of 2.24 μm. The *p*-to-*p* transmittance was then fitted using the value of d_{31}, giving d_{33} = 7.0 pm/V and a thickness of 2.24 μm.

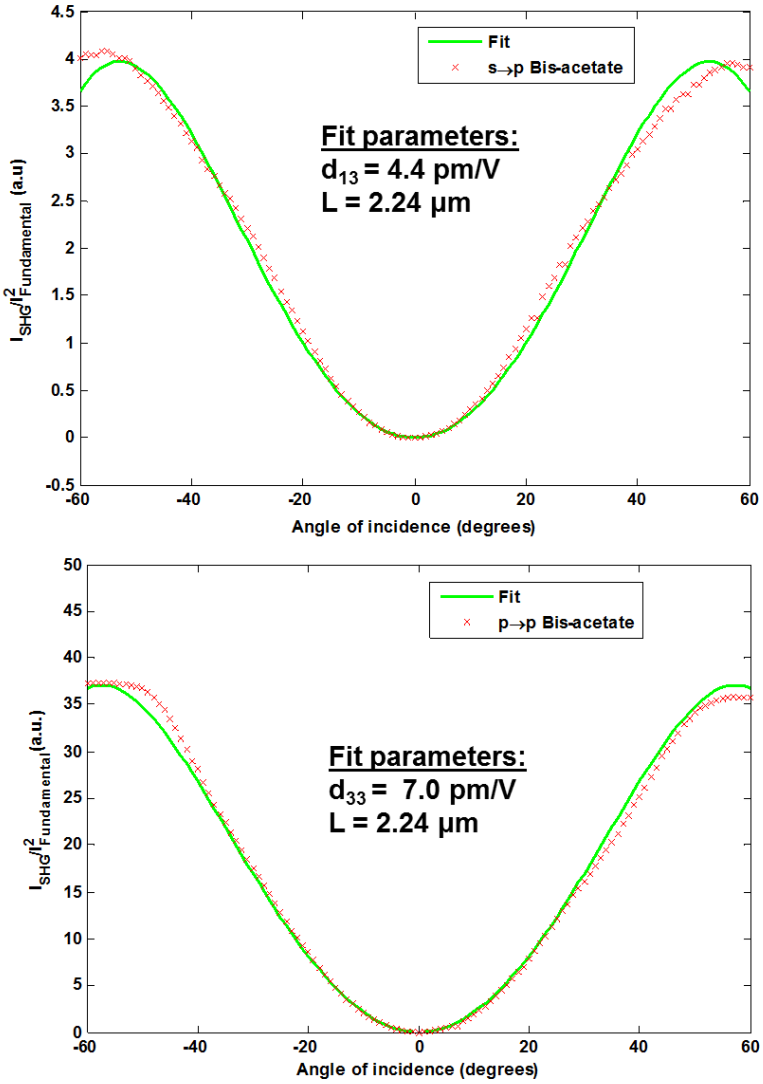

Figure 2.9: Parameter fits for d_{33} and d_{31} for a side-chain tolane chromophore NLO polymer ("bis-acetate", see Chapter 3 for structure), fitted for *s*-to-*p* (top) and *p*-to-*p* (bottom) and transmittance.

The relatively simple optical model allows for quick fitting of the SHG data and an estimate of the magnitude of SHG coefficients, but it is subject to several limitations. The ratio of d_{33}/d_{31} was found to be 1.6, well below the ratio of 3 predicted for weak poling conditions. The discrepancy highlights the intrinsic difficulty of SHG coefficient

measurements. Closed-form solutions for SHG transmittance that include multiple reflections of the fundamental, birefringence, and absorption as well as multiple layers for electrode residues and transparent electrodes have been unavailable until very recently.[3] It was accordingly difficult to assign uncertainty to the SHG measurements, although comparison of the SHG coefficients with similar polymers poled under similar circumstances[11] suggests that the estimates are below the true value.

A more straightforward application of SHG measurement involved the measurement of degradation of SHG coefficients due to relaxation of the chromophores. Rather than measure the SHG as a function of angle, the SHG was measured at a constant angle as a function of time at an elevated temperature, or as a function of temperature at a constant ramp rate. The relative SHG coefficient at time t (d_t/d_0) was computed as the square root of the ratio of SHG intensity relative to initial SHG intensity (also controlling for variations in the fundamental intensity over time). These measurements are discussed in Chapter 3.

Because the poled NLO polymers used in this study are more immediately applicable to electro-optic modulator applications than second harmonic generation, and because of the difficulties in accurately measuring SHG coefficients, it is useful to supplant the SHG coefficient measurements with measurements of electro-optic coefficients. Both SHG and electro-optic coefficients arise from molecular hyperpolarizability, and are related using a two-level dispersion model, where the electro-optic coefficient is assumed to arise solely from electronic effects and not from acoustic or optical phonons.[12, 13]

2.3 ELECTRO-OPTIC COEFFICIENTS

The electro-optic (EO) coefficient describes the change in the index of refraction of a material in the presence of an applied DC or low frequency electric field. Like SHG coefficients, EO coefficients are described with a third-rank tensor that can be reduced to a two-dimensional 6×3 matrix using contracted notation:

$$\Delta\left(\frac{1}{n^2}\right)_i = \sum_j r_{ij} E_j \qquad 2.14$$

where $\left(\frac{1}{n^2}\right)_i$ are the six coefficients in the common expression for the index ellipsoid (see Born and Wolf).[9] The most direct way to measure EO coefficients would be to apply an electric field in a given direction and measure the accompanying change in the index of refraction; however, the size of the electric field that can be applied is limited to the dielectric breakdown of the material, and EO coefficients are typically on the order of 50 pm/V for NLO polymers.[14, 15] Dielectric breakdown fields for typical NLO polymers are approximately 100 V/μm, and fields of this magnitude cause poling that changes the EO coefficients. For a polymer of index 1.6, application of Equation 2.14 with a 10 V/μm field leads to an index change on the order of 0.001, which is detectable by direct measurement of the index of refraction, but modulation of the voltage at a low frequency (100-2000 Hz) is often employed to improve uncertainty of the measurement.

A number of methods have been devised to measure EO coefficients. Because EO materials are often employed in EO modulators, one relevant method is to construct a simple EO modulator of known dimensions (for instance, a Mach-Zehnder interferometer as described in Chapter 1) and measure the voltage required for modulation. The EO coefficient is inversely proportional to the half-wave voltage, the voltage applied to the EO modulator required to produce a relative phase lag of half a wave. These methods are limited because they require an extensive fabrication process to obtain data.

Other, more convenient methods allow for measurement of EO coefficients in thin polymer films that are poled as deposited. For electrode-poled polymers, the NLO polymer is spin-coated onto a transparent conducting electrode and coated with a second gold electrode. Measurement of the EO properties is accomplished by measuring the polarization retardation in the EO material using a Soleil-Babinet compensator at variable applied voltages and incident angles.[16, 17] The advantages of this method are that it can be done without removing the top electrode required for electrode poling, but it is subject to errors introduced by absorption of the transparent conductor and EO film that are only corrected with extensive knowledge of the anisotropic optical properties of each layer.[18] In addition, an assumption must be made concerning the ratios of EO coefficients arising from *s*- and *p*-polarizations; in particular, only one independent EO coefficient can be determined. Park *et al*. described a simplified Fabry-Perot method for reflective measurement of independent EO coefficients.[19]

For poled polymers that were corona poled, no top opaque electrode was applied, and waveguiding methods were used. One such method is the attenuated total reflection (ATR) method,[20] which uses a prism in contact with the polymer sample, as shown in Figure 2.10. Laser light (in this case from a HeNe 633 nm laser) enters a high index prism and experiences total internal reflection at the prism/air interface (or the electrode/air interface if a semitransparent electrode is coated onto the prism). However, if the air layer is thin enough, the evanescent wave propagates sufficiently into the polymer film in frustrated total internal reflection.[21] For a polymer film on a substrate of lower index than the film, light is confined inside the film under certain conditions, with the film acting as a slab waveguide. When light is confined inside the waveguide, the reflectance drops sharply, allowing for characterization of index of refraction and thickness of films as well as nonlinear optical properties.

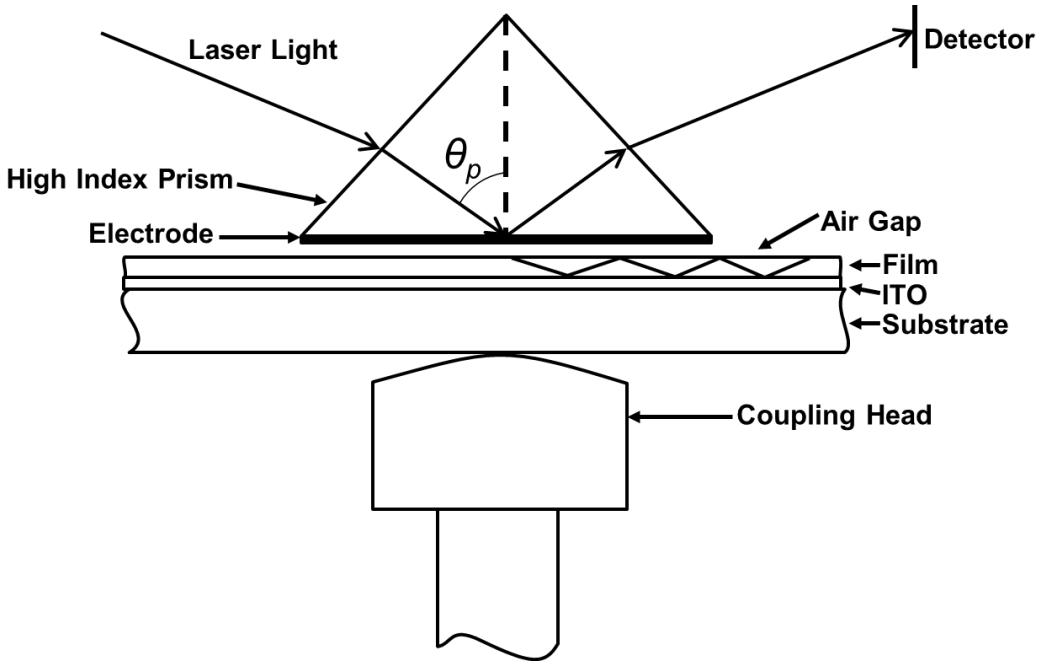

Figure 2.10: Diagram of geometry for prism coupling measurement of refractive index and electro-optic coefficients for thin films.

2.3.1 Measurement of linear optical properties by prism coupling

The conditions for guided waves for 3-layer slab waveguides can be derived from geometrical optics (for symmetric waveguides) and Maxwell's relations (for asymmetric waveguides). For confinement, the angle of propagation must be greater than the critical angle for internal reflection, and the phase change due to two reflections (and the corresponding propagation through the film) must be an integer multiple of 2π. The angle of propagation, and indices of refraction of the film and cladding layers are the determinative parameters. Birefringence is accounted for by specifying the ordinary and extraordinary indices of refraction of the film, n_o and n_e, respectively. The criteria for guided modes are given here for *s*-polarization (transverse electric, or TE):[22]

$$k_0\sqrt{n_o^2 - N^2}d_f - \tan^{-1}\frac{\sqrt{N^2 - n_{\text{top}}^2}}{\sqrt{n_o^2 - N^2}} - \tan^{-1}\frac{\sqrt{N^2 - n_{\text{bot}}^2}}{\sqrt{n_o^2 - N^2}} = m\pi \qquad 2.15$$

For *p*-polarization (transverse magnetic, or TM) light:

$$k_0 \frac{n_o}{n_e} \sqrt{n_e^2 - N^2} d_f - \tan^{-1} \frac{n_o n_e \sqrt{N^2 - n_{\text{top}}^2}}{n_{\text{top}}^2 \sqrt{n_o^2 - N^2}} - \tan^{-1} \frac{n_o n_e \sqrt{N^2 - n_{\text{bot}}^2}}{n_{\text{bot}}^2 \sqrt{n_o^2 - N^2}} = m\pi \quad 2.16$$

In these equations, $N = n_p \sin \theta_p$ is the effective index (related to the angle of incidence in the prism via Snell's law), n_{top} and n_{bot} are the indices of refraction of the top (air) and bottom (substrate) layers, respectively, k_0 is the vacuum wavenumber, d_f is the film thickness, and m is a non-negative integer that is the mode number.

As the thickness and index of the film increases, the number of modes satisfying the mode equation above increases. As the angle of incidence is being changed, dips in reflection identify the angle (and hence the effective index) that corresponds to each guided mode. Assuming the indices of the top and bottom layers and the prism are known, and that the effective index can be inferred from the angle of incidence (referencing of the prism angle is required), the index of refraction and thickness can be determined. For TE propagation, the presence of two modes allows Equation 2.15 to be solved for the thickness and ordinary index. Similarly, for TM propagation, the presence of two modes is sufficient for the thickness and extraordinary index to be determined if the ordinary index is first inferred from TE analysis or assumed to be equal to the extraordinary index. When more modes are available than are needed to specify the parameters, the additional information is used to compute standard deviations for the fit parameters.

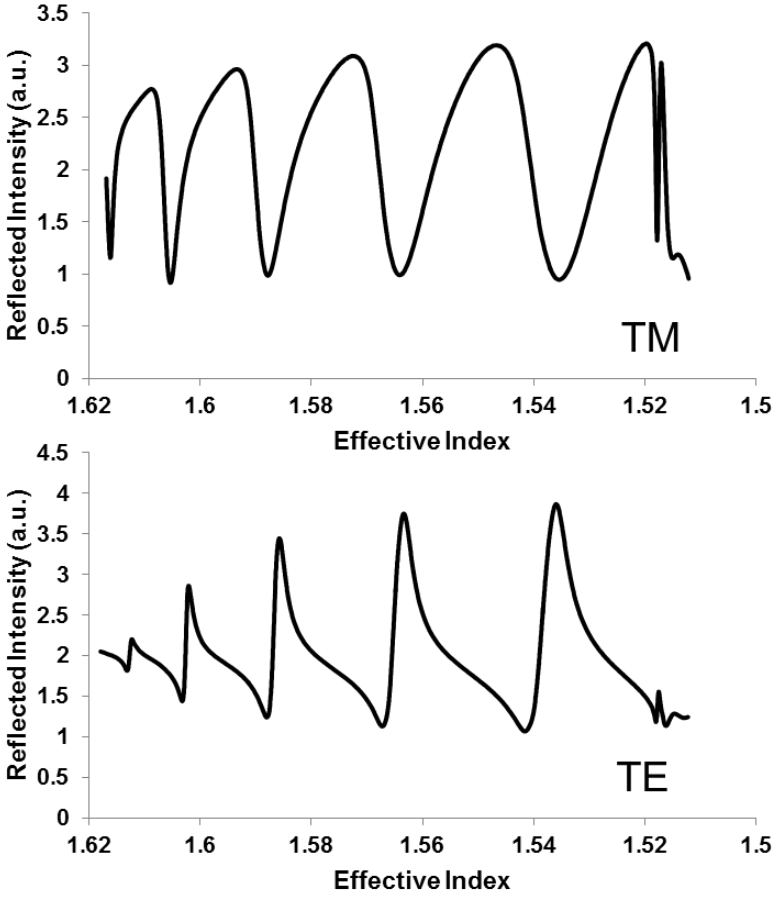

Figure 2.11: Plot of reflectance versus effective index (see text) for a prism coupled, unpoled NLO polymer. The effective index values at the local minima are used to fit the film thickness and index: $n_o = 1.6163$ (error 0.0001), $n_e = 1.6175$ (error 0.0014), $d_f = 2.88$ μm (error 0.07 μm).

Figure 2.11 shows a plot of reflectance versus effective index (i.e. $n_p \sin \theta_p$) for an uncrosslinked, unpoled "bis-acetate" tolane polymer (see Chapter 3). The effective index values corresponding to local minima were determined using a MATLAB program, and the effective index values were used in Equations 2.15 and 2.16, which lead to the following values for the film index and thickness: $n_o = 1.6163$ (error 0.0001), $n_e = 1.6175$ (error 0.0014), $d_f = 2.88$ μm (error 0.07 μm). The drops in reflectance appear distorted in the case of TE light due to the presence of the thin metal electrode layer on the prism.

The effect of the metal coating on the locations of the local minima was verified to be minimal using thin film reflectance models that account for additional layers as well as comparisons to experiments done using a non-coated prism.

2.3.2 Using prism coupling to measure EO coefficients

When an electric field is applied to an electro-optic sample, there is a change in the index of refraction, causing in a change in the effective index for the guided modes and a shift in the reflectance curve illustrated in Figure 2.12. The modulation in the reflectance ΔR at a given experimental point is equal to the slope of the reflectance curve times the index modulation, provided that the change in index is sufficiently small. The experiment point should be chosen as the point with maximum slope.

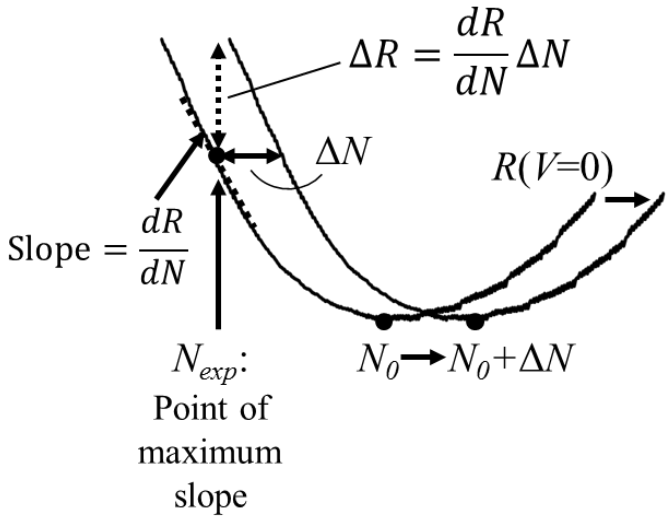

Figure 2.12: Modulation of reflectance curve by application of a voltage to an EO polymer. The modulation in reflectance ΔR at a given experimental point (chosen as the point of maximum slope) is approximately equal to the slope of the reflectance curve times the modulation in index.

Just as with SHG coefficients, the EO coefficients of poled polymer films are reduced to two independent coefficients for the case where the direction of the applied

electric field is coincident with the direction of poling. Outside the absorbing region, the EO coefficient can be related to experimentally measurable quantities by the following equations:[22]

$$r_{13} = -\frac{R_m^{TE}}{\left(\frac{\partial R}{\partial N}\right)_{TE}\frac{\partial N_{TE}}{\partial n_o}} \cdot \frac{2d_f}{n_o^3 V} \qquad 2.17$$

$$r_{33} = -\frac{R_m^{TM} + \left(\frac{\partial R}{\partial N}\right)_{TM}\frac{\partial N_{TM}}{\partial n_o}\frac{n_o^3 r_{13} V}{2d_f}}{\left(\frac{\partial R}{\partial N}\right)_{TM}\frac{\partial N_{TM}}{\partial n_e}} \cdot \frac{2d_f}{n_e^3 V} \qquad 2.18$$

In these equations, the indices of refraction and thickness are determined by the prism coupling method described above, R_m is the modulation of reflectance (equivalent to ΔR in Figure 2.12), $\partial R/\partial N$ is the slope at the experimental point in Figure 2.12, and V is the applied voltage. The remaining information needed to compute EO coefficients comes from the partial derivatives of the effective index with respect to the film index. These partial derivatives are computed by differentiating Equations 2.15 and 2.16 with respect to the relevant film index of refraction and solving for $\partial N/\partial n$.

2.3.3 Experimental setup

The prism coupling apparatus, manufactured by Metricon Corp. (model 2010/M), operates at a wavelength of 633.5 nm (HeNe) with a silicon photodiode detector. Prisms (model 200-P-1) are coated with Ni (~100 Å) via e-beam sputtering (CHA Industries, Inc.) for measurement of electro-optic coefficients. Modulation of reflectance caused by the application of a small voltage (10 V) is very small compared to the total intensity signal that is measured. In order to improve measurement accuracy of modulated reflectance, a 10 V sinusoidal (AC) voltage was applied across the sample via a function

generator (BK Precision), with frequency set to 100 Hz in order to avoid interference by 60 Hz ambient noise. The prism electrode was electrically connected to the prism coupler chassis using conductive epoxy, and the voltage was applied to the chassis.

Because there is a sinusoidal voltage applied, the intensity of light at the detector consists of a DC component and a much smaller AC component with the same 100 Hz frequency as the applied voltage. The signal from the photodiode was amplified with the desired gain and offset provided by an external amplifier, but the amplifier was modified to bypass the high pass filters that would otherwise filter out the AC component. The AC component was isolated using a virtual lock-in amplifier consisting of a 24-bit digital-to-analog converter data acquisition card (National Instruments, 4472) and customized LabVIEW software. The settling time for the lock-in amplifier is 0.5 s, and the angle of incidence was controlled by a stepper motor moving at one step every second to allow sufficient sampling time. The LabVIEW software stores the time, DC signal, modulated amplitude, and phase difference between the modulated signal and the applied voltage.

MATLAB software was used to match the intensity vs. effective index data collected within the Metricon software with the intensity and modulated amplitude vs. time data collected by the LabVIEW software. The index and thickness values were determined using Equations 2.15 and 2.16. The experimental point for determination of EO coefficients was found by fitting the DC intensity in the neighborhood of the first guided mode to a normalized 10^{th}-order polynomial. The polynomial was differentiated to compute the slope at each effective index. The two points with the maximum and minimum slope (on opposite sides of the local minimum in reflectance) were chosen as experimental points for calculation of EO coefficients. Equations 2.17 and 2.18 are applied at these points to yield the EO coefficients.

2.3.4 Electro-optic coefficients

The electro-optic coefficients are proportional to the magnitude of the modulated (AC) reflectance intensity divided by the *slope* of the DC reflected intensity. Figure 2.13 shows a plot of this quantity vs. effective index, as well as the DC reflected intensity itself. The sample is "bis-MAC" tolane polymer corona-poled at 4.5 kV needle voltage for 15 minutes (Chapter 3). Since the slope of the DC intensity is in the denominator in Equation 2.17, the EO coefficients cannot be determined at the mode index, and it is desirable for the sample to exhibit steep slopes in DC intensity around the mode index. For the bis-MAC sample, the estimated EO coefficients are r_{33} = 4.4 pm/V and r_{33} = 1.7 pm/V.

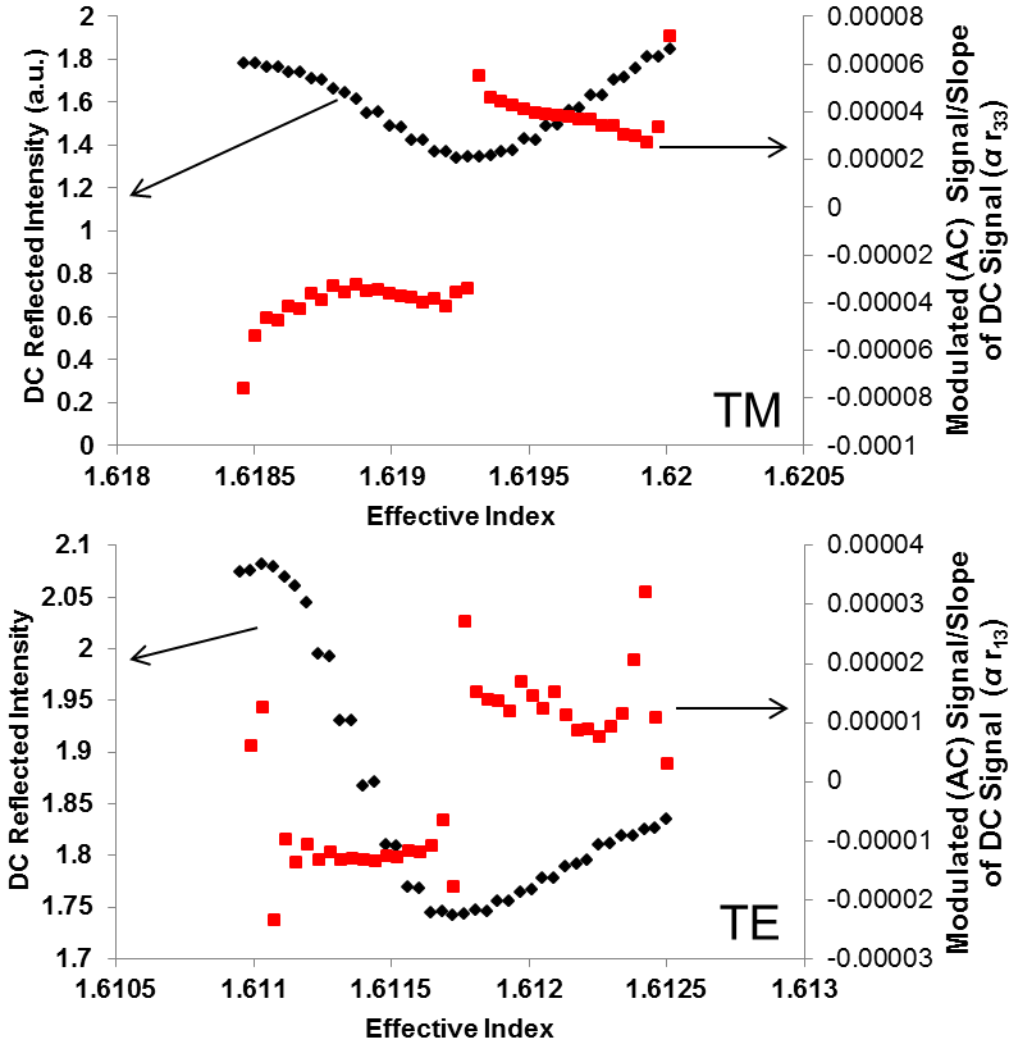

Figure 2.13: Plots of reflected DC intensity and modulated intensity normalized by slope of DC intensity vs. effective index in the region close to the first guided mode for both TM (top) and TE (bottom) incidence. The sample is a corona-poled "bis-MAC" tolane polymer (see Chapter 3). The EO coefficients were estimated to be r_{33} = 4.4 pm/V and r_{33} = 1.7 pm/V.

A number of factors contribute to uncertainty of the EO coefficients computed in this manner. First, the modulated (AC) intensity measured by the lock-in amplifier includes noise that must be subtracted. In addition, the settling time of the lock-in amplifier causes variability in the modulated intensity, as the lock-in amplifier may not

have time to "lock-in" on the modulation frequency before the sample stage moves for the next measurement. Second, the DC reflected intensity profiles may become artificially distorted or shifted, leading to inaccuracies in the slopes of these profiles. If one side of the reflectance dip is more sloped than the other, estimates based on slopes on one side can be drastically different than those based on experimental points on the other side.

One cause of distortion in reflected intensity is overcoupling, which occurs when the sample is pressed with excessive pressure against the prism. Because the substrates, for most samples, are 1 mm thick glass slides, it is often necessary to increase the pressure to achieve coupling of light into the film. However, overcoupling can lead to a shift in the modulated (AC) intensity relative to the DC intensity. When one is divided by the slope of the other, the mismatch leads to wildly varying estimates of EO coefficients. Overcoupling was easily addressed by reducing the coupling head pressure.

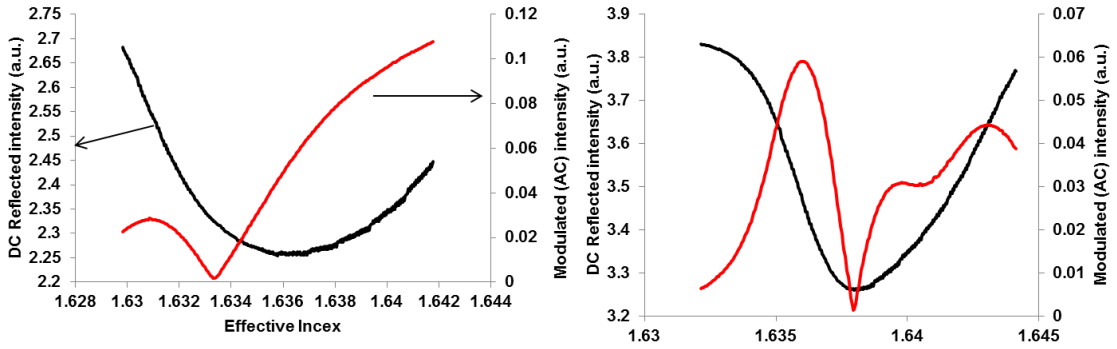

Figure 2.14: Overcoupling causes a relative shift in modulated intensity relative to DC intensity, leading to error in estimates of EO coefficients.

A convenient aspect of the prism coupling technique is that it measures the ordinary and extraordinary indices of refraction, so the EO coefficient can be compared

to the birefringence, which is also a function of poled order. To demonstrate this, poled polymers were prepared with polycarbonate (Sigma-Aldrich) loaded with various weight ratios of disperse red 1 (DR1), an NLO dye. EO coefficients were estimated in the manner described above, with one estimate on each side (left side estimate, LSE, and right side estimate, RSE) of the reflectance dip, corresponding to the maximum and minimum slope of reflectance. Birefringence ($n_o - n_e$) was also measured as a matter of course. Table 2.2 shows the results. As predicted and observed previously[23], the birefringence and EO coefficients increased with increasing loading of the NLO chromophore, then level off and start to decrease. The data also illustrate differences in the estimate of EO coefficients for the left and right edge of the dip. These differences can be caused by overcoupling or lag/lead in the modulated signal relative to the DC signal.

Table 2.2: SHG coefficient estimates for poled guest/host composites of DR1 in polycarbonate based on the left side estimate (LSE) and right side estimate (RSE) of the reflectance dip.

Wt. ratio DR1:polymer	Change in birefringence	r_{13} (LSE)	r_{13} (RSE)	r_{33} (LSE)	r_{33} (RSE)	r_{33}/r_{13}
2	-0.0089	1.22	1.14	4.07	2.78	2.9
5	-0.0173	0.6	2.6	6.5	6.6	4.1
10	-0.0205	3.9	4.0	25.4	8.6	4.3
15	-0.0368	4.6	5.6	26.3	2.5	2.8
20	-0.0282	3.9	6.6	13.0	13.2	2.5

2.4 CONCLUSION

The measurement of reliable SHG coefficients and EO coefficients requires great care. The methods described above use relatively simple models for the optical film; for instance, they often neglect the transparent conductor layers, birefringence, and absorption of the various layers. The errors associated with these simplified models have been estimated, and a variety of extensions are available.[18, 22, 24] The goal of the efforts presented here is to allow for quick, simple characterization of the SHG and EO coefficients. As the focus of our research turns from thermal stability of NLO coefficients to maximizing the EO coefficients, the methods described here will be increasingly useful for assessing new NLO chromophores and polymers as they are produced.

2.5 REFERENCES

1. Jerphagnon, J.; Kurtz, S. K., Maker Fringes: A Detailed Comparison of Theory and Experiment for Isotropic and Uniaxial Crystals. *Journal of Applied Physics* **1970,** 41, (4), 1667-1681.

2. Herman, W. N.; Hayden, L. M., Maker fringes revisited: second-harmonic generation from birefringent or absorbing materials. *J. Opt. Soc. Am. B* **1995,** 12, (3), 416-427.

3. Park, D. H.; Herman, W. N., Closed-form Maker fringe formulas for poled polymer thin films in multilayer structures. *Opt. Express* **2012,** 20, (1), 173-185.

4. Boyd, R. W., *Nonlinear Optics*. 3rd ed.; Elsevier: Boston, 2008.

5. Kuzyk, M. G.; Dirk, C. W., *Characterization techniques and tabulations for organic nonlinear optical materials*. CRC: 1998; Vol. 60.

6. Wang, X., Gated integrator with signal baseline subtraction. In Google Patents: 1996.

7. Yamasaki, K.; Tanaka, A.; Kimura, T.; Kajimoto, O., An inexpensive handmade grated integrator. *Review of Scientific Instruments* **1995,** 66, (8), 4395-4396.

8. Clark, W. G.; Kerlin, A. L., Solid State Gated Integrator. *Review of Scientific Instruments* **1967,** 38, (11), 1593-1596.

9. Born, M.; Wolf, E.; Bhatia, A. B., *Principles of optics: electromagnetic theory of propagation, interference and diffraction of light*. Cambridge Univ Pr: 1999.

10. Bartella, J.; Schroeder, J.; Witting, K., Characterization of ITO- and TiOxNy films by spectroscopic ellipsometry, spectraphotometry and XPS. *Applied Surface Science* **2001,** 179, (1–4), 181-190.

11. Jungbauer, D.; Teraoka, I.; Yoon, D. Y.; Reck, B.; Swalen, J. D.; Twieg, R.; Willson, C. G., Second order nonlinear optical properties and relaxation characteristics of poled linear epoxy polymers with tolane chromophores. *Journal of Applied Physics* **1991,** 69, (12), 8011-8017.

12. Singer, K. D.; Kuzyk, M. G.; Sohn, J. E., Second-order nonlinear-optical processes in orientationally ordered materials: relationship between molecular and macroscopic properties. *J. Opt. Soc. Am. B* **1987,** 4, (6), 968-976.

13. Morichere, D.; Chollet, P. A.; Fleming, W.; Jurich, M.; Smith, B. A.; Swalen, J. D., Electro-optic effects in two tolane side-chain nonlinear-optical polymers: comparison between measured coefficients and second-harmonic generation. *Journal of the Optical Society of America B: Optical Physics* **1993,** 10, (10), 1894-900.

14. Dalton, L. R., Organic electro-optic materials. Past, present, and future. *PMSE Preprints* **2003,** 88, 173-174.

15. Kuzyk, M. G., Physical Limits on Electronic Nonlinear Molecular Susceptibilities. *Physical Review Letters* **2000,** 85, (6), 1218-1221.

16. Teng, C. C.; Man, H. T., Simple reflection technique for measuring the electro-optic coefficient of poled polymers. *Applied Physics Letters* **1990,** 56, (18), 1734-1736.

17. Schildkraut, J. S., Determination of the electrooptic coefficient of a poled polymer film. *Applied Optics* **1990,** 29, (19), 2839-41.

18. Park, D. H.; Lee, C. H.; Herman, W. N., Analysis of multiple reflection effects in reflective measurements of electro-optic coefficients of poled polymers in multilayer structures. *Opt. Express* **2006,** 14, (19), 8866-8884.

19. Park, D. H.; Luo, J.; Jen, A. K.-Y.; Herman, W. N., Simplified Reflection Fabry-Perot Method for Determination of Electro-Optic Coefficients of Poled Polymer Thin Films. *Polymers* **2011,** 3, (3), 1310-1324.

20. Chen, A.; Chuyanov, V.; Garner, S.; Steier, W.; Dalton, L., Modified Attenuated Total Reflection for the Fast and Routine electro-optic Measurements of Nonlinear Optical Polymer Thin Films. *Organic thin films for photonic applications* **1997,** 14, 158.

21. Hecht, E., *Optics (4th edn)*. Addison-Wesley: San Francisco, CA, 2002; p 698.

22. Park, D. H. Characterization of linear electro-optic effect of poled organic thin films. University of Maryland, College Park, MD, 2008.

23. Dalton, L. R.; Sullivan, P. A.; Bale, D. H., Electric Field Poled Organic Electro-optic Materials: State of the Art and Future Prospects. *Chemical Reviews* **2009,** 110, (1), 25-55.

24. Hayden, L. M.; Sauter, G. F.; Ore, F. R.; Pasillas, P. L.; Hoover, J. M.; Lindsay, G. A.; Henry, R. A., Second-order nonlinear optical measurements in guest-host and side-chain polymers. *Journal of Applied Physics* **1990,** 68, (2), 456-465.

Chapter 3: Enhancement of second-order nonlinear optical stability by photocrosslinking across the chromophore

3.1 INTRODUCTION

The achievement of thermally stable second-order nonlinear optical (NLO) coefficients in polymers is an important but elusive goal in obtaining useful materials for commercial devices. While much attention has rightfully focused on tailoring chromophore shape and functionality to maximize second-order NLO coefficients and prevent chromophore aggregation during poling, less has been accomplished in the way of appreciably improving the thermal stability of NLO properties.

Several approaches have been employed to extend thermal stability of poled polymers. Incorporation of NLO chromophores into polymers with high glass transition temperatures (T_g) is effective but requires higher poling temperatures. Currently, a popular choice is amorphous polycarbonate[1-3], which has a T_g of nearly 200 °C, although the added chromophore lowers the T_g by plasticization. Restricting the motion of the chromophore in the polymer by covalently attaching the chromophore to the polymer chain increases the stability of NLO coefficients with time.[4]

Thermal stability can be improved through hardening of the polymer lattice by attaching reactive moieties, which are often thermally initiated. For example, polymers with pendant reactive groups can be thermally cured to create interpenetrating polymer networks that lead to stability of NLO effects.[5] Crosslinkable groups have included urethane[6], epoxy[7-9], benzocyclobutene[10], and Diels-Alder[11-13] chemistries. However, thermal curing presents a difficulty because heating leads to increased mobility of chromophores, so there is a tradeoff between maximizing poled order and maximizing long term thermal stability. In order to avoid this tradeoff, it is desirable to separate the poling and crosslinking processes.

Since poling is a thermally sensitive process, thermally initiated crosslinking is difficult to separate from poling unless the reaction kinetics of crosslinking are carefully controlled.[14] Alternatively, photoinitiated crosslinking allows for greater control since the crosslinking reaction can be delayed until after the chromophores are fully aligned. Lee *et al.* have demonstrated a maleimide polymer which photocrosslinks via the 2+2 cycloaddition of chalcone crosslinker groups placed both on the chromophore and on side chains of copolymer repeat units.[15] However, only a single crosslinkable group was inserted across the chromophore, and the stability increase corresponds to an increase in the T_g of about 30 °C. Betterton *et al*.[16] suggested the extension of crosslinking across the chromophore to include multiple crosslinkable acrylate groups. Increasing the number of links across the chromophore is expected to increase the degree of interchain crosslinking, thus increasing the degree of entanglements such that motion of the chromophore in the matrix is restricted.

3.2 NLO POLYMERS

3.2.1 Chromophore design

In order to demonstrate the effect of the number of photocrosslinkable groups, we synthesized a series of polymers bearing side-chain NLO chromophores with a variable number of crosslinkable methacrylate groups attached to the chromophore opposite the main chain attachment. Specifically, we targeted functionalized polynorbornene polymers with tolane chromophore[9, 17, 18] side groups with zero, one, and two crosslinkers attached to the electron donor. Although it is possible to functionalize polymers with crosslinkable groups following polymerization, we chose to polymerize prefunctionalized monomers, since this allows certainty of the number density of crosslinkable groups on the polymer. However, this requires polymerization of a monomer without reaction of the

crosslinkable group. In order to accomplish this, we chose ring opening metathesis polymerization (ROMP),[19-21] which shows a tolerance for crosslinkable groups such as epoxides, acrylates, methacrylates, and imides.[22]

Figure 3.1 shows the design elements of the monomer. The main polymerizable group is norbornene, the most widely studied and used polymerizable group for ROMP. The acceptor, a sulfonyl group,[23] is attached to the norbornene via an ester linkage. The sulfonyl group is conjugated to the tolane chromophore, which acts as a π-electron linkage between the acceptor and the donor. The electron donator is an amino group, and the crosslinkable group is a methacrylate, chosen because methacrylates can be selectively polymerized via photolysis of a free radical generating photoinitiator. It should be emphasized that the monomer was not chosen to provide maximal NLO efficiency; in fact, the tolane chromophore is inferior to polyene and stilbene chromophore linkages in terms of theoretical maximum NLO activity.[24] However, polyene and stilbene chromophores are known to be particularly sensitive to photooxidation by singlet oxygen,[25] which limits their applicability to photocrosslinked systems.

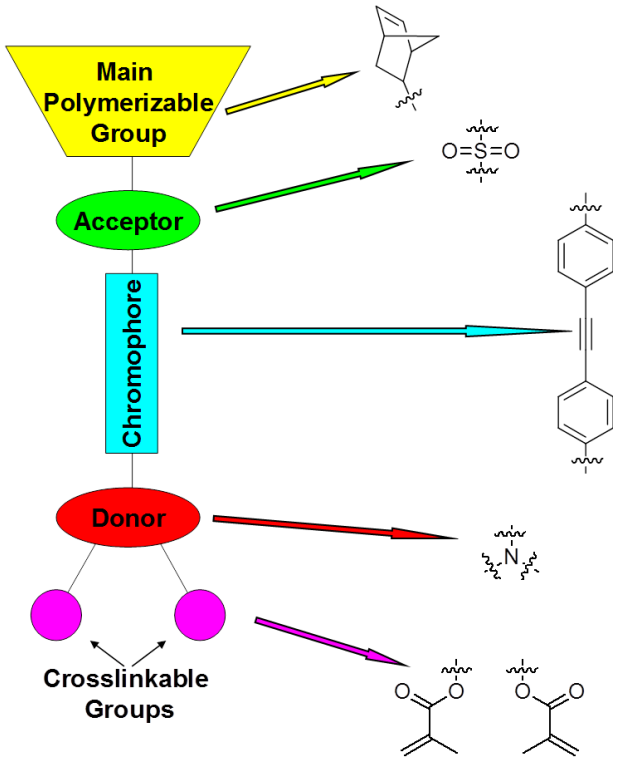

Figure 3.1: Schematic showing the design of the monomer precursor to the crosslinkable NLO polymers.

3.2.2 Outline of synthesis

The monomer synthesis involved combination of an acceptor fragment and a donor fragment in a coupling reaction to form the monomer (Figure 3.2). The acceptor fragment was formed by the condensation of a phenyl sulfone with norbornene carboxylic acid, while two donor fragments were designed with one or two alcohol functional groups. The combination takes place in three steps: the amine donor was first coupled to trimethylsilyl (TMS) protected acetylene using Sonogashira conditions. The product was subsequently deprotected, followed by coupling to the acceptor fragment to form the monomer. The original synthesis, discussed in detail elsewhere,[26] calls for purification between the coupling steps, but a recent modification of the reaction due to

William K. Bell allows for a three-step, one-pot reaction that results in lower yield but allows for fewer purification steps.

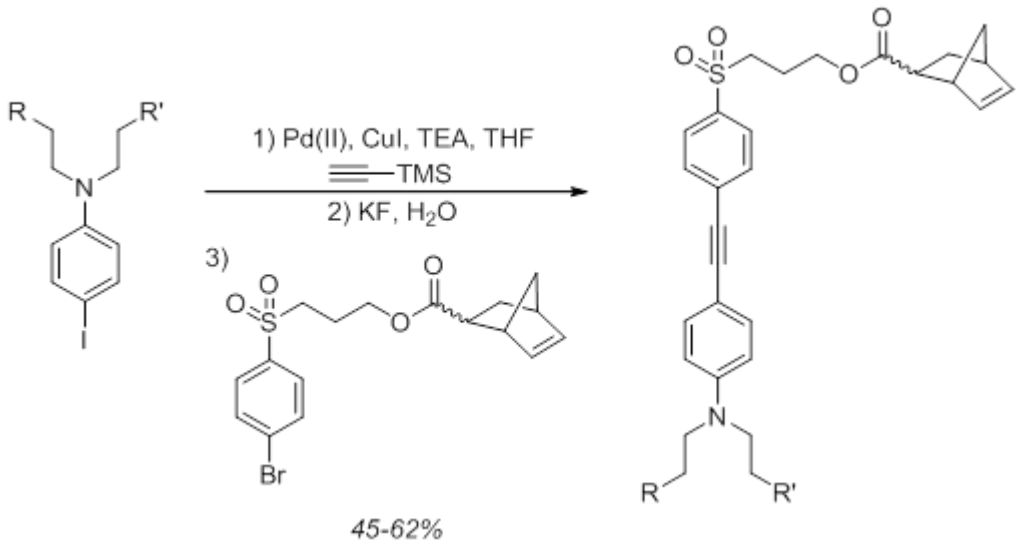

Figure 3.2: Outline of the three-step, one-pot reaction conditions used for coupling of the amine donor to the sulfone acceptor. R, R'= −OH, −H for the singly crosslinkable monomer, otherwise R, R'= −OH, −OH.

Following synthesis of the monomer and just prior to polymerization, the crosslinkable groups were attached by reaction with methacryloyl chloride in the presence of triethanolamine. The monomer was polymerized by reaction with Grubbs II catalyst[19] to yield a polymers with 30-60 kDa molecular weight, as shown in Figure 3.3.

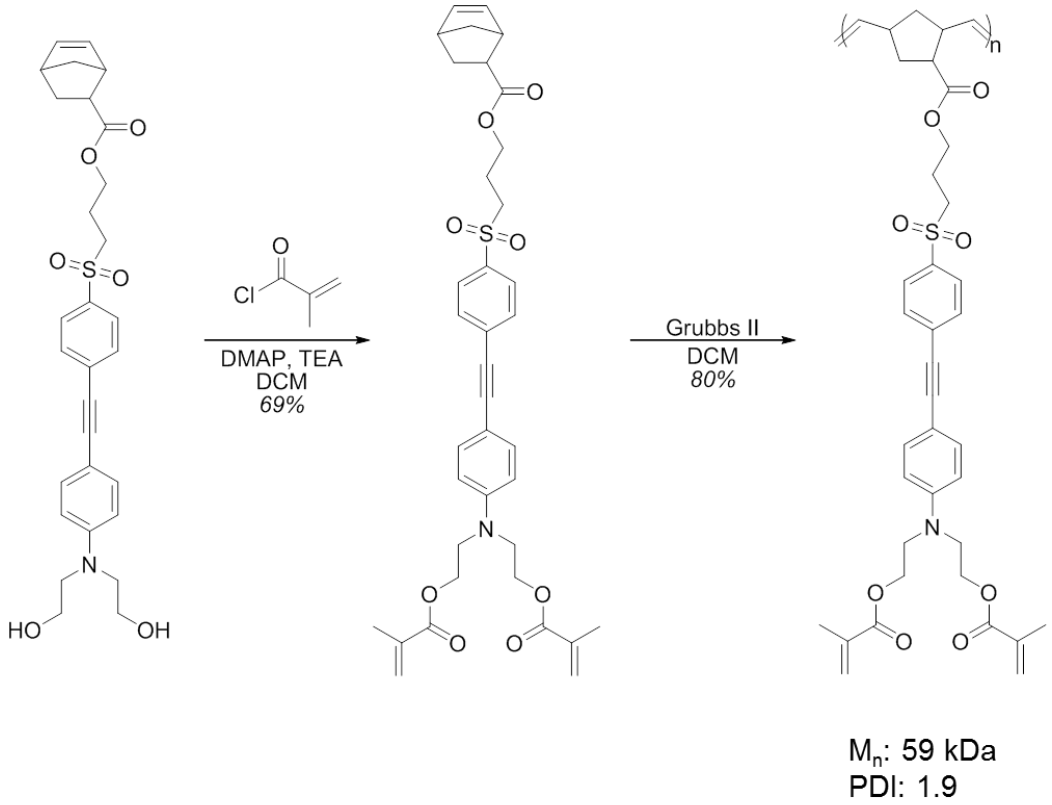

Figure 3.3: The final steps of the NLO polymer synthesis, shown for the case of bis-crosslinkable polymer: functionalization with methacryloyl chloride and polymerization using Grubbs II catalyst.

The resulting polymers are termed “Bis-acetate”, “Mono-mac”, and “Bis-mac” for the noncrosslinkable bis-acetate, singly crosslinkable mono-methacrylate, and doubly crosslinkable bis-methacrylate polymers, respectively. Figure 3.4 shows the structures as well as the molecular weight and glass transition temperatures (T_g). The glass transition temperatures are low compared to most other NLO polymers. By comparison, polycarbonate, a common polymer host for guest/host NLO materials, has a T_g of over 150 °C.[2] The low T_g adversely affects NLO stability, but it is convenient for assessing the stabilizing effect of crosslinking because it allows poling of the polymers at lower temperatures. Other ROMP-polymerized polymers are available with glass transition

temperatures over 150 °C.[27] Thermogravimetric analysis showed that all three polymers are stable to greater than 250 °C.[26] In addition, polymer films remain soluble after exposure to visible light and after overnight baking at 85 °C and a 1 min hot plate bake at 110°C.

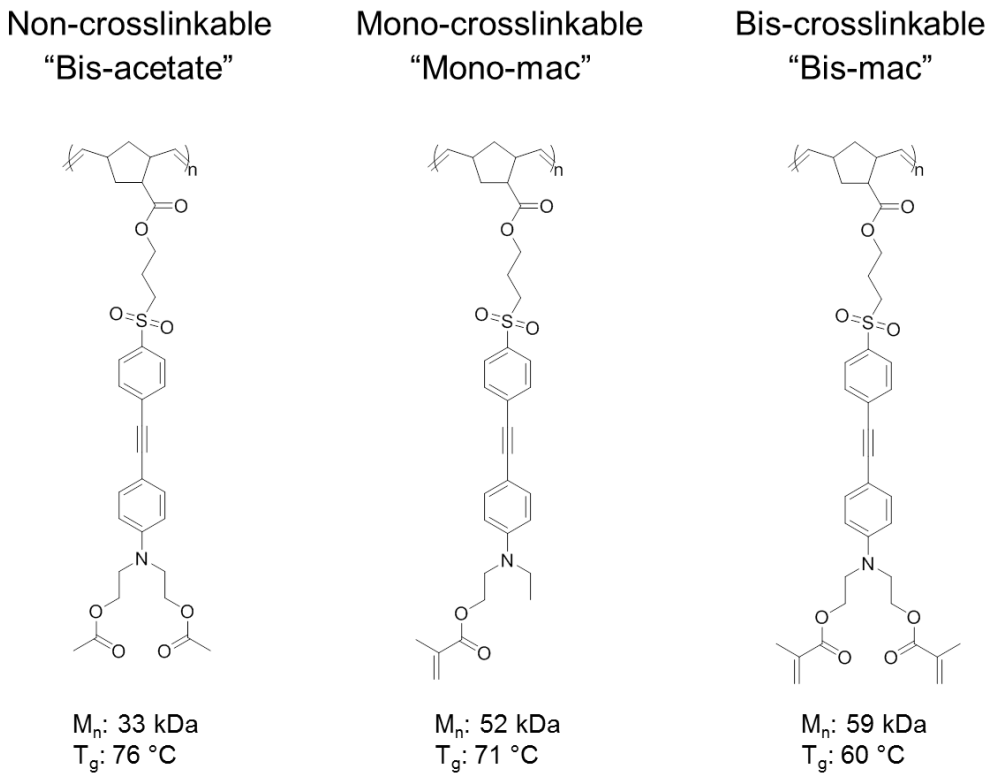

Figure 3.4: Structures, short names, molecular weights, and glass transition temperatures for the tolane polymers studied.

3.2.3 Optical properties

The absorbance and index of refraction have been characterized in films and in solution. All of the polymers have indices of refraction of approximately 1.62 at 633 nm, as characterized by prism coupling (Chapter 2) and spectroscopic ellipsometry. Figure 3.5 shows the UV absorption spectra of solutions of monomer precursors. The

bathochromic shift of the tolane shows that there is electronic communication between the donor and acceptor moieties. The wavelength of maximum absorption (λ_{max}) is 370 nm but is red-shifted further for the Mono-mac and Bis-mac polymers.

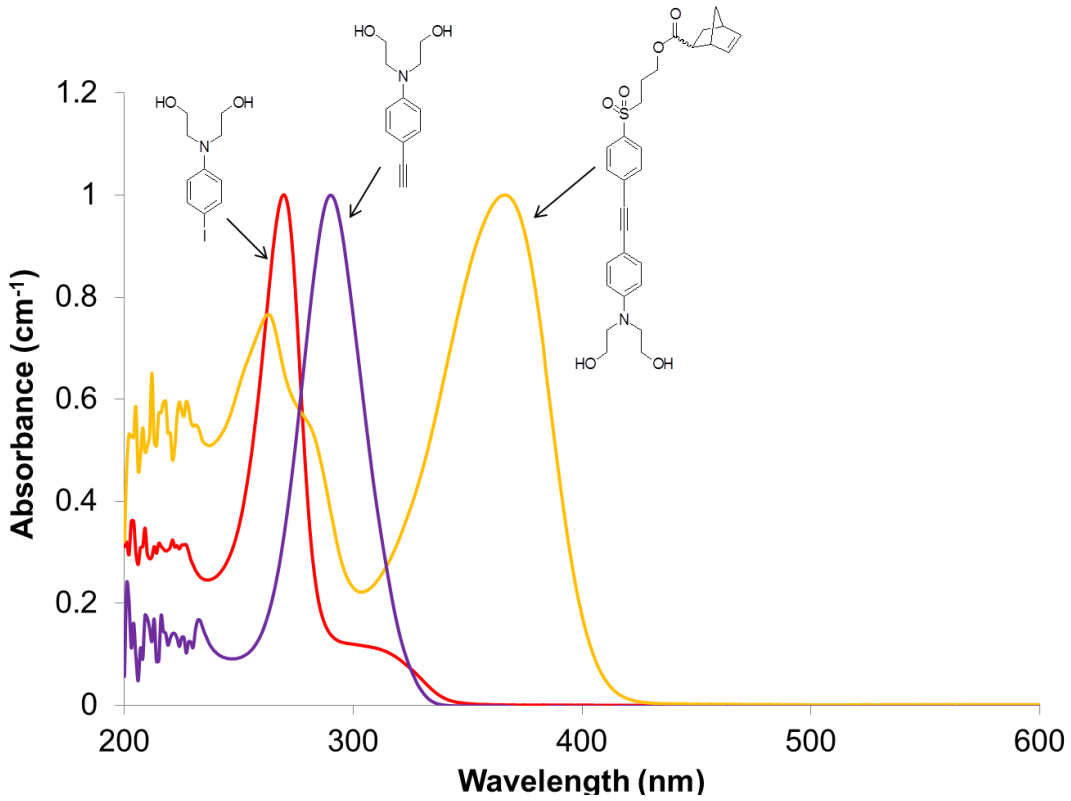

Figure 3.5: UV-vis spectra of solutions of tolane monomer precursors. The bathochromic shift is indicative of electric communication between the donor and acceptor.

The absorbance of the chromophore near 365 nm presents some challenges for UV curing via crosslinking by irradiation in the UV. The difficulty is compounded by the fact that the loading of absorber is high compared to the amount of photoinitiator typically added to methacrylate polymerization formulations. Consequently, identifying a photoinitiator that efficiently initiates free radical polymerization was a major challenge for the tolane polymers, as discussed in Section 3.4.

3.3 POLING

3.3.1 Contact poling

In order to achieve a net noncentrosymmetry in the bulk polymer material, the dipolar chromophores must be aligned, usually by electric field poling. Although novel methods such as laser assisted poling have been demonstrated[28], the two most common methods for poling organic NLO polymers are contact poling and corona poling. Contact poling involves sandwiching the NLO film between two electrodes, one of which is typically made of transparent indium tin oxide (ITO). The structure of a contact-poled sample is shown in Figure 3.6 (top). The NLO polymer was dissolved in cyclopentanone and spin-coated onto ITO-coated glass slides (Sigma Aldrich, 70 Ω/□ nominal sheet resistance). A thin layer of gold was deposited by sputter coating (Electron Microscopy Supplies). To facilitate attachment of electrode leads and prevent shorting, the gold electrode was deposited through a shadow mask so that the gold electrode was smaller than the ITO. Also, prior to spin-coating, a portion of the ITO was etched away from the substrate, allowing contact to the gold electrode in these regions without shorting through the polymer.

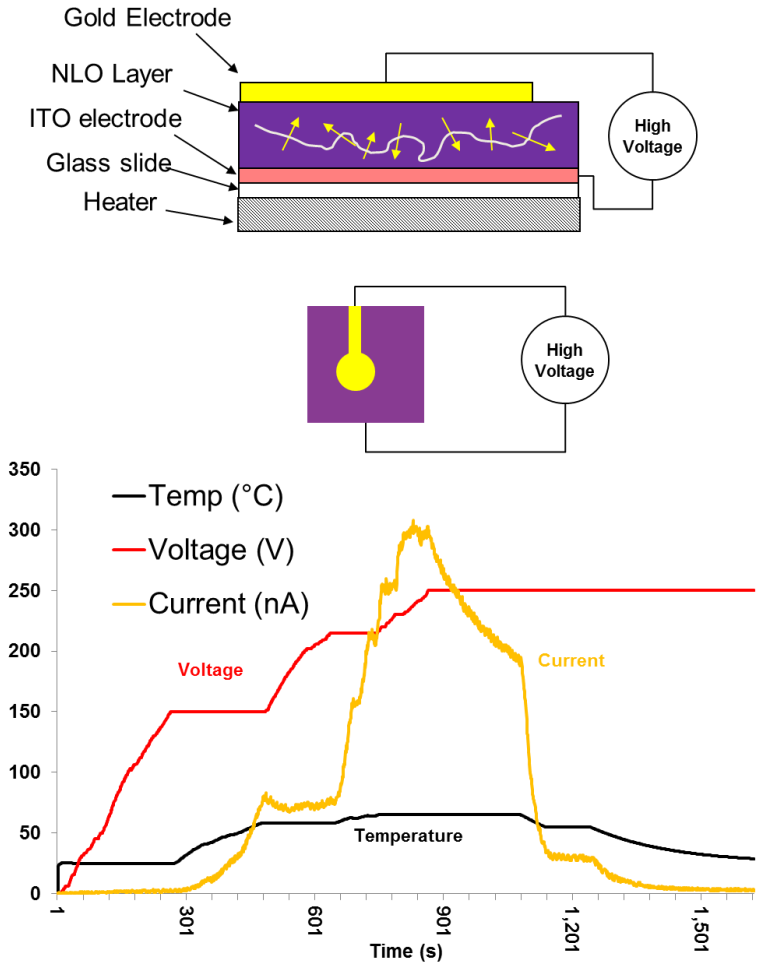

Figure 3.6: Sample structure from side view (top) and top view (middle) and a chart of process variables (bottom) for contact poling of an NLO polymer.

Contact poling allows for a uniform electric field of known magnitude to be applied over a fairly large area, but it is subject to shorting of the electrodes, resulting from dielectric breakdown of the polymer.[29] Dielectric breakdown occurs for most polymers at or below a field of 120 V/μm, but the exact breakdown voltage was found to be extremely variable and dependent on the quality of the film and electrode. Some breakdown events are self-repairing, as the current spikes and then decreases to below the original level, while other events cause a permanent short between the electrodes, ruining

the sample. Even at conditions well below breakdown, there is a nonzero current through the film that is due to a field electron emission and Fowler-Nordheim tunneling.[30] Since the time of these experiments, Huang *et al.* have demonstrated reduced tunneling by using ITO substrates that are coated with TiO_2.[31]

In order to prevent shorting, the following process, illustrated by the process variables at the bottom of Figure 3.6, was used for contact poling. First, with the sample at room temperature, the voltage is raised to approximately 50 V/μm, well below the breakdown voltage of the polymer. The thickness of the sample is determined by prism coupling. The current was monitored by a picoammeter with leads placed across the sample. The temperature was then raised slowly to ten degrees below the glass transition temperature. The voltage and temperature were then alternately increased to their maximal values, 100 V/μm and just below the T_g, respectively, paying careful attention to the current because the current is especially sensitive to temperature near the T_g. The polymer was poled for a fixed time, at the end of which the temperature was slowly ramped down. Finally, the field was removed and the electrodes were purposely shorted to remove any residual field. For the case where poling was accompanied by photocrosslinking, the sample was exposed at the maximum poling temperature. Exposure was accompanied by a large increase in the observed current, possibly a result of the photoelectric effect at either the gold or ITO interfaces.

3.3.2 Corona Poling

Corona poling uses a needle suspended above the sample to which a high voltage is applied. The high voltage around the thin needle tip produces an electric corona, ionizing the air at the needle tip. Ions are directed towards the grounded ITO electrode below the polymer, causing a buildup of charge on the top of the NLO polymer. The

main advantage of corona poling is that it is not susceptible to shorting due to dielectric breakdown, because the field is not generated by a top electrode. Unfortunately, the process is more difficult to control, because the electric field is not directly measured. This also complicates comparison of NLO coefficients of corona poled polymers, because the fields may vary between samples due to differences in thickness or dielectric constant. In addition, corona poling is known to lead to localized film damage due to breakdown. The corona poling setup is illustrated for poled polymers in Figure 3.7.

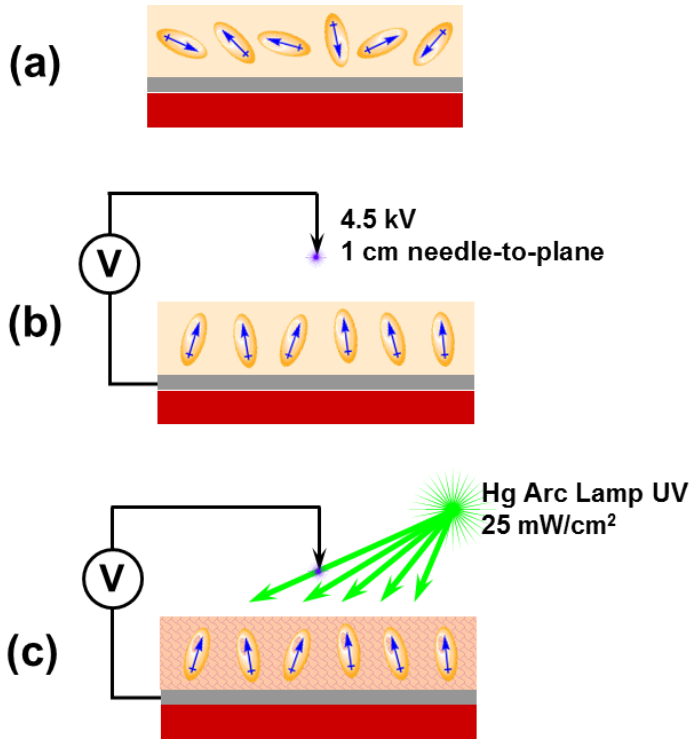

Figure 3.7: Cartoon diagram illustrating corona poling of polymer films. (a) the unpoled sample illustrating the disordered state of the dipoles in the film; (b) the sample is heating to near the Tg and application of a 4.5 kV voltage to the corona needle causes the dipoles to align. (c) Crosslinked samples are exposed with a Hg high pressure arc lamp broadband UV source at 25 mW/cm^2 intensity.

The film damage caused by corona poling introduces a tradeoff between increasing poling voltage to increase attainable NLO coefficients and preventing the film from being damaged. Some ways to address this problem include introducing a second high voltage grid to control fields at the film[32] and using a thin removable protective layer such as polyacrylic acid during poling.[33] However, it was determined through comparative experiments for our polymers that a PAA layer significantly degrades the SHG activity of poled films.

In order to maximize the SHG intensity of poled polymers while controlling film damage, a fractional factorial experiment design was carried out by changing needle to sample distance, poling time, poling voltage, and poling temperature. Films of bis-acetate polymer (2 μm thick, T_g 76 °C) were coated from cyclopentanone solution and baked in a vacuum oven at 85 °C overnight to remove excess solvent. Two levels were used for needle to sample height (1 or 3 cm), poling voltage (3.5 or 4.5 kV), poling time (2 or 10 minutes). A 2^{4-1} fractional factorial design with 3 center points was employed to screen important process conditions. Figure 3.8 shows the model fits for dependence on each variable. Poling time did not seem to have an effect for times between 2 and 10 minutes. The most important effects come from decreasing the needle to plane distance, which increases SHG response but also increases the film damage, and from decreasing the temperature, which increases SHG response while reducing film damage. Subsequent corona poling experiments of the polymer films utilized a 70 °C poling temperature, 4.5 kV voltage, 1 cm needle-to-plane distance, and a 10 minute poling time.

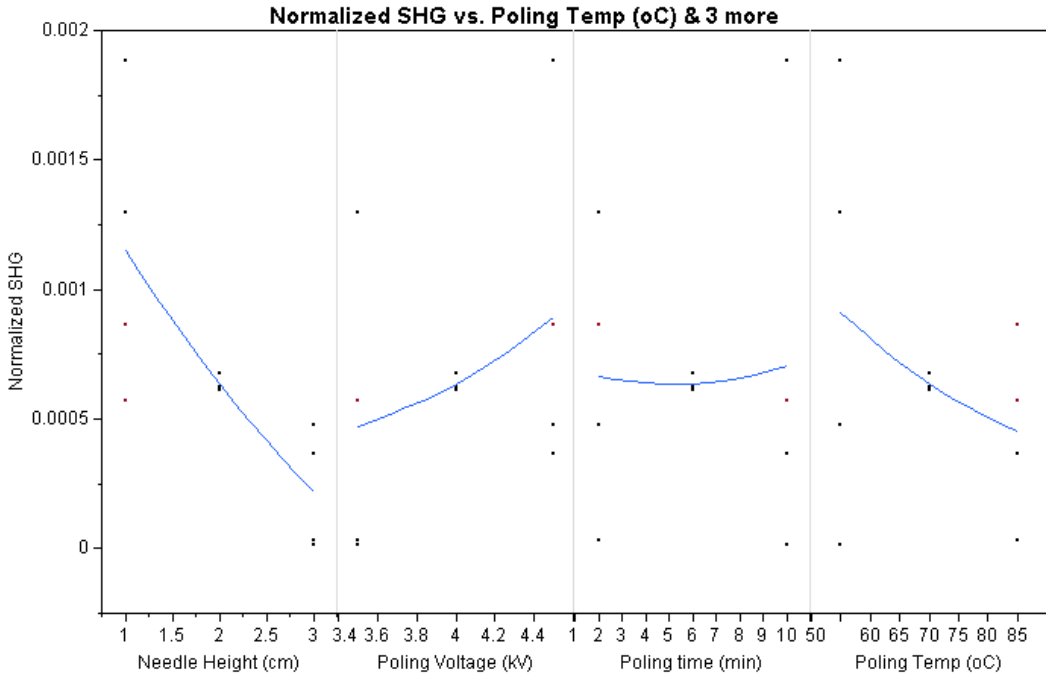

Figure 3.8: Second-order model fits for 24-1 fractional factorial experimental design using needle height, poling voltage, poling time, and poling temperature as independent variables. The response variable is SHG intensity (in arbitrary units) normalized by the square of fundamental intensity at a 45° angle of incidence.

3.4 PHOTOCROSSLINKING

The effect of increased thermal stability imparted by photocrosslinking NLO polymers is predicated on the successful conversion of the methacrylate groups in the film during, but not before irradiation with light, thus taking advantage of the potential for photocrosslinking to allow separation of the poling and crosslinking processes. The effects of a variety of photoinitiators, crosslinking conditions, and cocrosslinkers on crosslinking efficiency have been investigated, using Fourier transform infrared spectroscopy to monitor crosslinking conversion.

3.4.1 Autoinitiated crosslinking

Mono-mac and Bis-mac tolane polymers undergo crosslinking upon irradiation with broadband UV light generated from a medium pressure Hg arc lamp source. Upon irradiation using a Novacure spot curing system (EXFO, now Lumen Dynamics), Bis-mac and Mono-mac polymers become completely insoluble in cyclopentanone and dichlorobenzene solvents that easily dissolve the polymers that have not been exposed to light. Monitoring of the C-C triple bond in the FTIR (2100 cm^{-1}) during irradiation indicated an accompanying degradation of chromophore[26], suggesting that the polymerization might be autoinitiated.

To evaluate the thermal stability of NLO properties, films of Bis-acetate, Mono-mac, and Bis-mac polymers were spin-coated onto ITO substrates and contact poled using the procedure described above. Mono-mac and Bis-mac polymers were poled both with and without irradiation. The intensity was not measured in situ, but it is estimated to be on the order of 20 mW/cm^2 based on subsequent lamp measurements at similar distances. The NLO activity was monitored by SHG intensity at constant angle of incidence as a function of temperature for a temperature ramp from room temperature at a constant ramp rate of 10 °C/min. As expected, the SHG intensity decayed to zero completely as the temperature approached the glass transition. SHG intensity decay for Mono-mac and Bis-mac polymers is shown in Figure 3.9. There is perhaps a slight delay in the SHG decay for Mono-mac, but no appreciable difference for the Bis-mac polymer, showing that the crosslinking conversion, while sufficient to insolubilize the polymers, is not sufficient to significantly increase the stability of NLO properties.

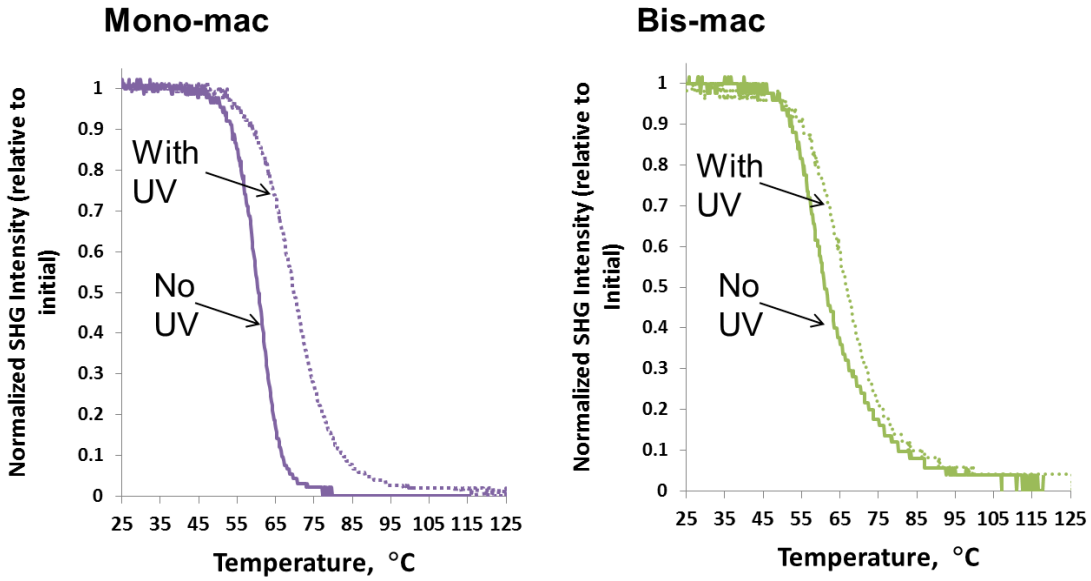

Figure 3.9: SHG intensity vs. temperature for a 10 °C/min temperature ramp for Mono-mac and Bis-mac exposed and unexposed polymers.

3.4.2 Evaluation of crosslinking by FTIR spectroscopy

The lack of increase of thermal stability of Mono-mac and Bis-Mac films with no initiator suggested that the extent of crosslinking conversion in both polymers in the absence of photoinitiator was very low. In order to evaluate crosslinking of NLO polymer films, we employed real-time FTIR spectroscopy. FTIR has been used as a tool to monitor conversion of acrylates in dental resins[34] as well as thiol-ene and thiol-acrylate reactions used in a wide variety of engineering applications.[35-38] A portion of a representative mid-IR spectrum is shown in Figure 3.10. The peaks that can be used to monitor conversion of the methacrylate functional groups are the vinyl C−H bend mode, located at 816 cm^{-1}, and the C−C stretch, located at 1635 cm^{-1}. Conversion is calculated as the percent decrease in the peak area of these peaks; however, since the 816 cm^{-1} is obscured by other peaks in the tolane spectra, the 1635 $cm^{-1}$was primarily used. Nearby

aromatic breathing modes (~1604, 1583 cm^{-1}) were used as reference peaks when necessary to correct for intensity fluctuations between spectra.

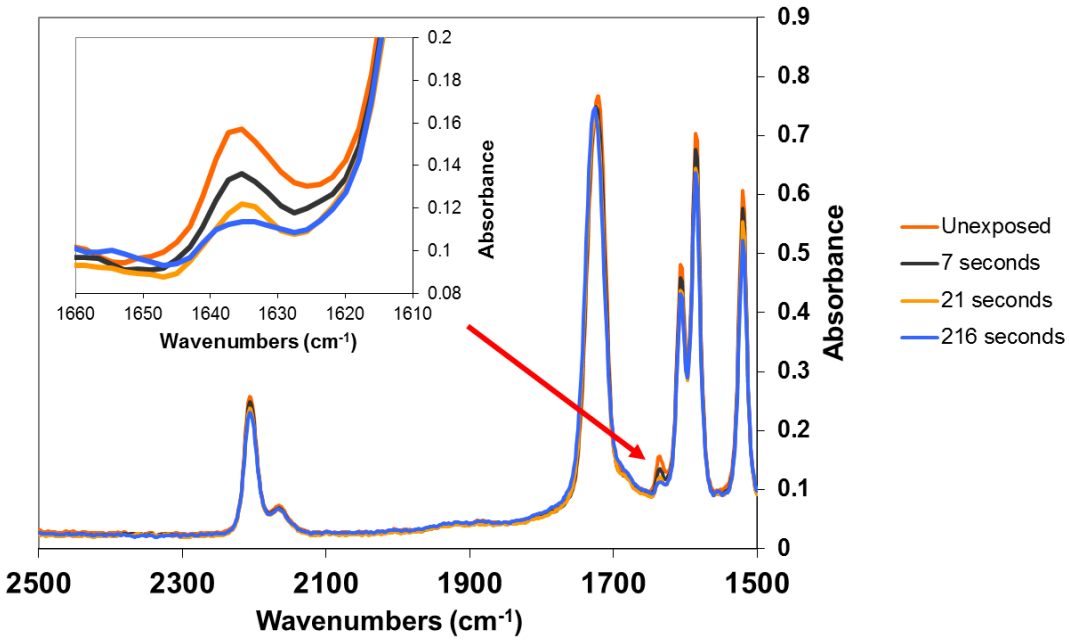

Figure 3.10: A portion of the FTIR absorption spectrum of the Mono-mac polymer with Irgacure 819 photoinitiator exposed with a 470 nm LED at several time intervals.

3.4.3 Photoinitiators

The low crosslinking conversion evidenced by **Error! Reference source not ound.** led us to consider adding a photoinitiator to improve crosslinking conversion. Due to the absorption of Bis-mac and Mono-mac polymers at 370 nm, we sought free radical photoinitiators with appreciable absorbance above 400 nm, which are shown in Figure 3.11. Irgacure 819 (obtained from BASF), a bis-acylphosphine oxide, absorbs at 370 nm but has an absorbance tail that reaches above 400 nm. Irgacure 784 (BASF) has an absorbance at 398 and a much smaller one at 470. Camphorquinone (CQ), when combined with an aliphatic amine, is a common photoinitiator for curing of acrylate-

based dental resins and has an absorbance (albeit very weak at 28 L/mol cm extinction) at 514, well to the red of the polymer absorbance.[39] Finally, bis(triphenylgermyl)ketone (BGK), which demonstrates absorption well into the visible spectrum, was synthesized according to Tehfe *et al*.[40]

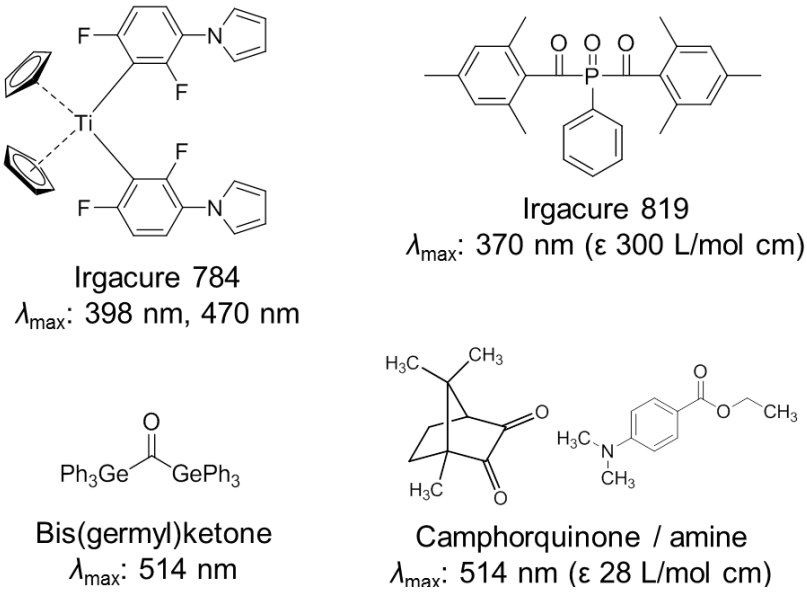

Figure 3.11: Several photoinitiators with appreciable absorbance above 400 nm.

Two exposure sources were used to initiate radical generation. The Novacure 2100 spot curing system (Lumen Dynamics) employs a 100 W high pressure Hg arc lamp, with major emission peaks at 365, 405, 436, and 550 nm. The broadband light intensity was measured to be 23 mW/cm^2 at a distance of 5 inches from the light guide output. In addition, a 450 nm LED with an intensity of approximately 8 mW/cm^2 at the sample was employed to isolate initiation due to light absorbed in the visible region.

Special care was taken with the visible light photoinitiators to avoid prematurely exposing samples. Also, in order to conserve the valuable NLO polymers and to provide a less crowded FTIR spectrum, formulations of the photoinitiators in a mixture of

acrylate monomers (85 wt% isobornyl acrylate (IBA), 15 wt% ethylene glycol diacrylate (EDGA)) as well as in neat pentaerythritol triacrylate (P3A) were used to screen photoinitiators. The BGK initiator did not initiate conversion of the acrylate double bond at a 1 wt% loading in the IBA/EDGA mixture and it had poor solubility in P3A. It was also found to have a short shelf life in spite of the effort taken to avoid exposing the initiator to visible light.

Camphorquinone in combination with ethyl p-dimethylaminobenzoate (DMAB) at loadings of 0.5 wt% of both CQ and DMAB in the IBA/EDGA mixture successfully initiated conversion of the acrylate double bonds. However, the extinction coefficient of CQ at 514 nm is quite low compared to that of other photoinitiators (cf. Irgacure 819, Figure 3.11) and it was believed that the absorption of light by the polymer would interfere with the photoinitiators. To simulate the absorption of the polymer, small amounts of the unfunctionalized precursor to the Mono-mac polymer, termed Mono-ol, was added in various molar ratios to CQ. Figure 3.12 shows the acrylate FTIR peaks for illumination with the 450 nm LED under N_2 purge for up to 300 s exposure. Addition of even small molar ratios of the Mono-ol chromophore caused inhibition of conversion. It should be noted that a 5:1 molar ratio of chromophore to CQ is actually much less than what is encountered with a typical loading of CQ into Bis-mac or Mono-mac polymer. In agreement with this result, 450 nm LED exposures of a Bis-mac formulation with CQ/DMAB at 2 wt% for both CQ and DMAB produced no conversion of methacrylate in the Bis-mac polymer. Although the inhibition of reaction by chromophore by itself is not proof that chromophore absorption is to blame, the low extinction coefficient of CQ as well as the lack of literature examples of CQ/amine photoinitiators used with absorbing monomers suggest that it is the case.

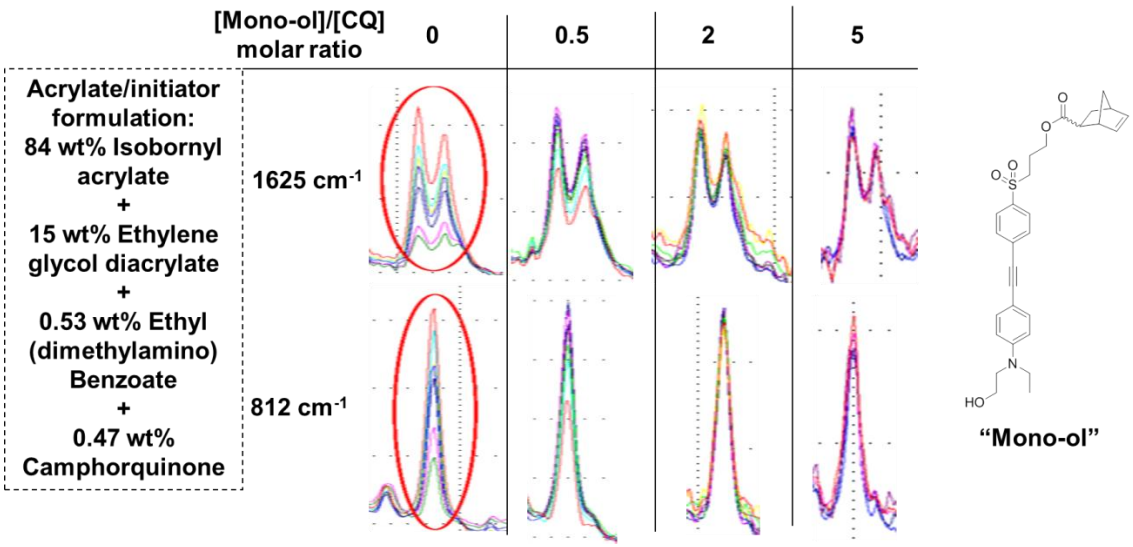

Figure 3.12: Acrylate FTIR peaks for acrylate conversion in an IBA/EGDA/CQ/DMAB mixture during illumination with the 450 nm LED light under N2 purge for up to 300 s exposure.

Irgacure 819 and Irgacure 784 photoinitiators both have absorption maxima that overlap the absorption of the chromophore. Using a combination of UV-vis spectroscopy and spectroscopic ellipsometry, the magnitude of absorbance of the Bis-mac polymer in the 350−600 nm regime was compared with the absorbance of PMMA films with 5 wt% Irgacure 819 and Irgacure 784, respectively. The absorbance per μm of films on quartz substrates was measured by an HP 8452 UV/vis spectrophotometer. For thick (>1 μm) Bis-mac films, the absorbance exhibited Fabry-Perot fringes, which mask the absorbance tail. To estimate the absorbance, UV/vis data was combined with spectroscopic ellipsometry measurements (M-2000, J.A. Woollam Co., Inc.) and the absorption band edge was fitted with a Lorentzian function using WVASE software (J.A. Woollam). The results, shown in Figure 3.13, indicate that the absorbance of the polymer is greater than the absorbance of the Irgacure 819 and Irgacure 784 initiators, save for a small sliver of the spectrum just below 500 nm in the case of Irgacure 784. This is consistent with

studies of 450 nm LED irradiation of Bis-mac polymers containing Irgacure 819 and Irgacure 784 that show no crosslinking conversion for Irgacure 819 and a small but measureable effect for Irgacure 784. However, if a broadband UV source is used, Irgacure 819 successfully initiates crosslinking, suggesting that its action may depend on absorption at a lower wavelength, to the blue of the main absorbance peak for the chromophore (cf. Figure 3.5).

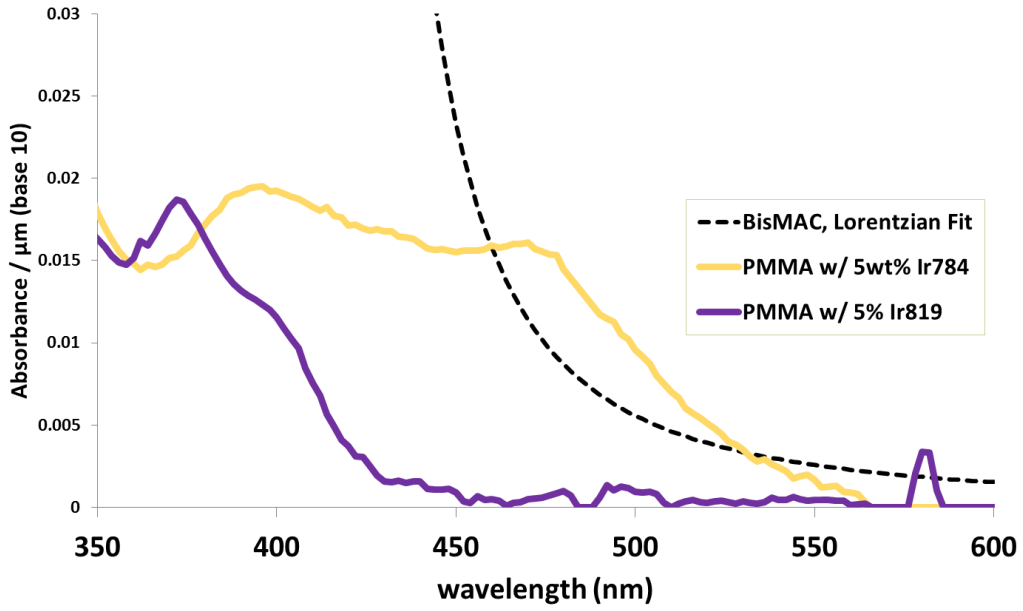

Figure 3.13: UV/vis absorbance per micron for a Bis-mac film and PMMA films with 5 wt% Irgacure 784 and Irgacure 819 initiators.

3.4.4 Crosslinking temperature

As expected, the temperature of the NLO polymers during exposure has a significant enhancement effect on the methacrylate double bond conversion in the Mono-mac and Bis-mac polymers. Figure 3.14 shows methacrylate conversion monitored by FTIR as a function of exposure time (exposure starts at 30 s) for exposure of Bis-mac

films with 5 wt% Irgacure 819 at various temperatures using a Novacure UV light source, indicating a dramatic temperature effect.

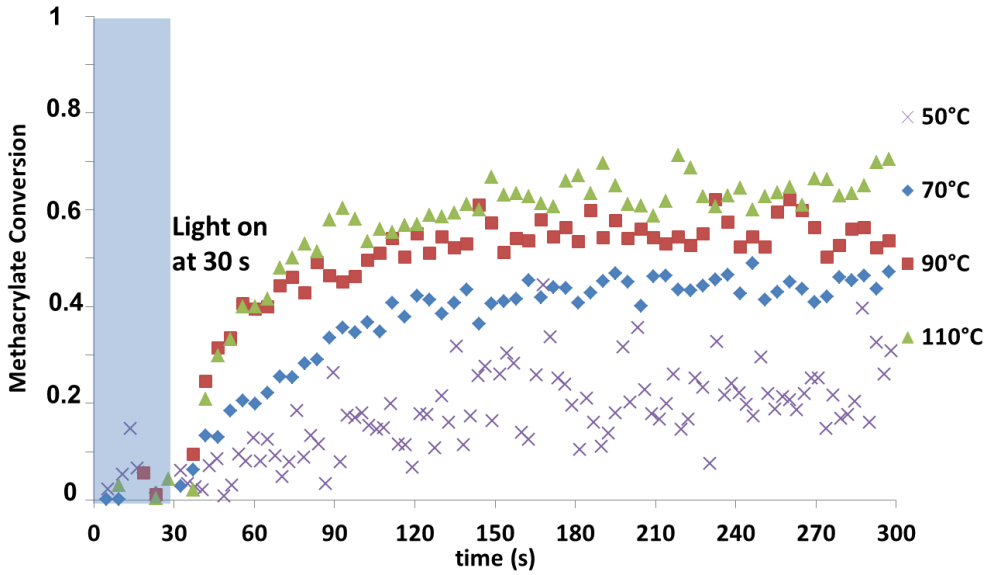

Figure 3.14: Methacrylate conversion monitored by FTIR as a function of exposure time (exposure starts at 30 s) for exposure of Bis-mac films with 5 wt% Irgacure 819 at various temperatures using a Novacure UV source.

Ideally, high conversion of double bonds would be achieved at low temperatures so that crosslinking could occur after cooling the sample following poling. However, the temperature effect can be exploited by ramping the temperature after reaching the maximum poling temperature while maintaining the poling field. For noncrosslinkable films, raising the temperature above T_g while maintaining the corona poling field causes film damage as described in Section 3.3.2. However, crosslinked films show no such damage, indicating that thermal stability has been imparted.

3.5 THERMAL STABILITY OF NLO PROPERTIES

To characterize the stability of NLO properties, SHG intensity is measure for samples at constant angle of incidence (45°) as described in Chapter 2. Effective SHG coefficients were determined relative to the initial value as given in the following equation:

$$\frac{d}{d_0} \cong \frac{\sqrt{I_{2\omega}/I_{2\omega}^{(0)}}}{I_{\omega}/I_{\omega}^{(0)}} \qquad 3.1$$

For these studies, polymer films containing 5 wt% Irgacure 819 (no initiator was used in Bis-acetate samples) were spin coated and baked under vacuum at 85 °C overnight to remove solvent. Samples were corona poled under N_2 using the corona poling conditions described in Section 3.3.2. At the end of incubation at the normal poling temperature, crosslinked samples were irradiated using the Novacure light source at 25 mW/cm^2 intensity. During this time, the temperature was ramped to 100°C at a 5 °C/min ramp rate to fully crosslink the samples. The temperature was then reduced to 25 °C and the poling field was finally extinguished.

The thermal stability of NLO properties was measured in two ways. First, the temperature was held constant and the effective SHG coefficients were monitored as a function of time. For non-crosslinked samples, the SHG intensity decays very fast when the temperature is close to T_g, but crosslinked samples retain stability for much longer and follow a different decay profile that tapers into a slow linear decay. Figure 3.15 shows the decay profiles of relative SHG coefficients for Mono-mac and Bis-mac samples with and without exposure to crosslink the sample. The additional stabilizing

effect of multiple crosslinkable groups is also demonstrated by the relative stability of exposed Bis-mac compared to exposed Mono-mac.

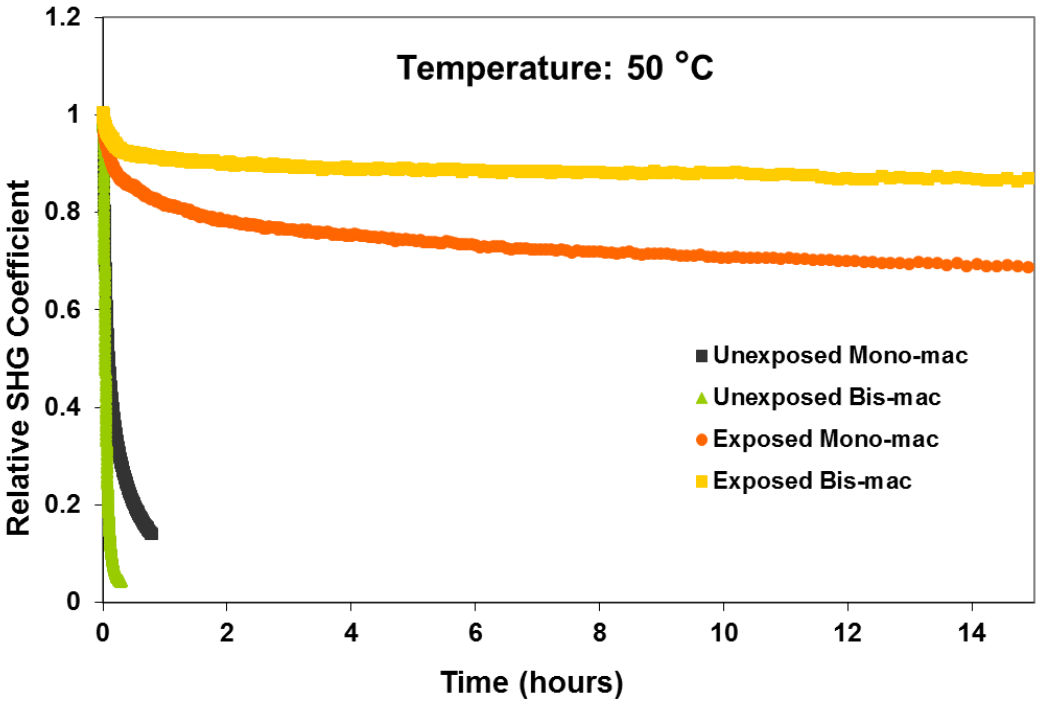

Figure 3.15: Decay profiles of relative SHG coefficients for Mono-mac and Bis-mac samples with and without UV exposure (see text) at 50 °C.

Thermal stability is also illustrated by considering the decay of SHG intensity as the temperature ramps from room temperature to an elevated temperature, as shown in Figure 3.16. In this case, while all polymer samples decay very quickly at the glass transition temperature, exposed Mono-mac and Bis-mac show enhanced thermal stability. Again, the doubly-crosslinked Bis-mac shows an improvement relative to Mono-mac.

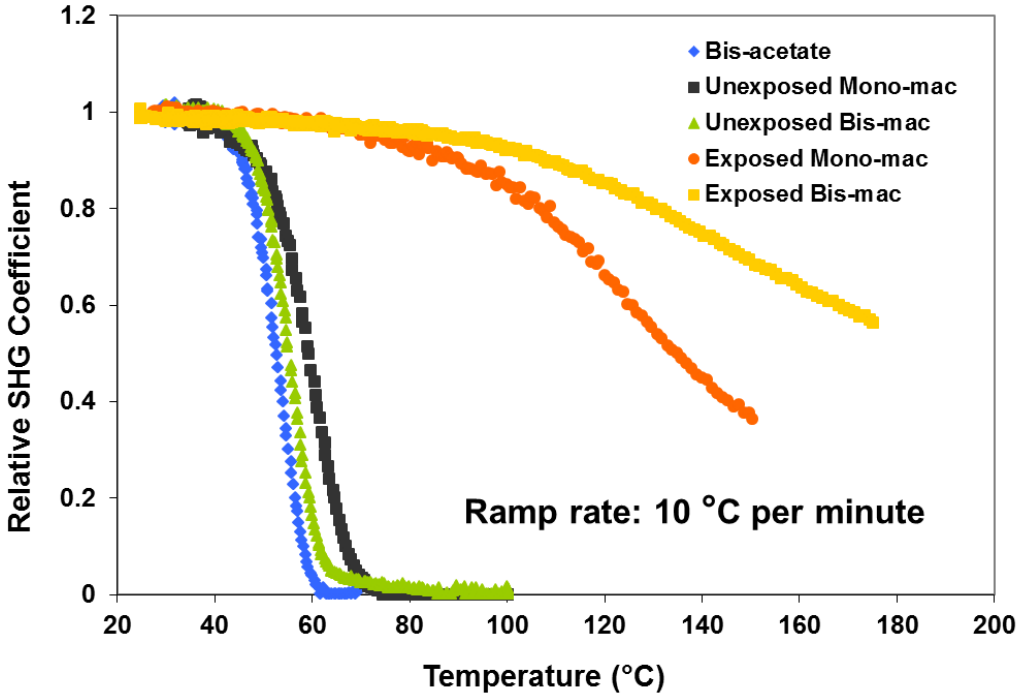

Figure 3.16: Relative SHG coefficients for poled polymer samples, including unexposed Bis-acetate and Mono-mac and Bis-mac samples with and without exposure as a function of temperature during a 10 °C/min temperature ramp.

The addition of reactive diluents, or cocrosslinkers, has been previously shown to increase conversion of in crosslinkable acrylate polymers.[41] To demonstrate the effect of reactive diluents, a multifunctional acrylate, pentaerythritol triacrylate, was added to the NLO polymers at 10 wt% loading while maintaining the 5 wt% of the Irgacure 819. The addition of the reactive diluent plasticizes the film, lowering the T_g, so the poling temperature is lowered to 55 °C. (The crosslinked films are still ramped to 100 °C during exposure, however.) Figure 3.17 shows the stabilizing effect of a reactive diluent for incorporation of P3A into Bis-mac polymers. SHG decay profiles of Bis-mac polymers with a reactive diluent similar to Figure 3.15 retain 75% of their initial values up to 60

hours at 100°C, which is remarkable considering that the T_g of the Bis-mac polymer is originally 70 °C.

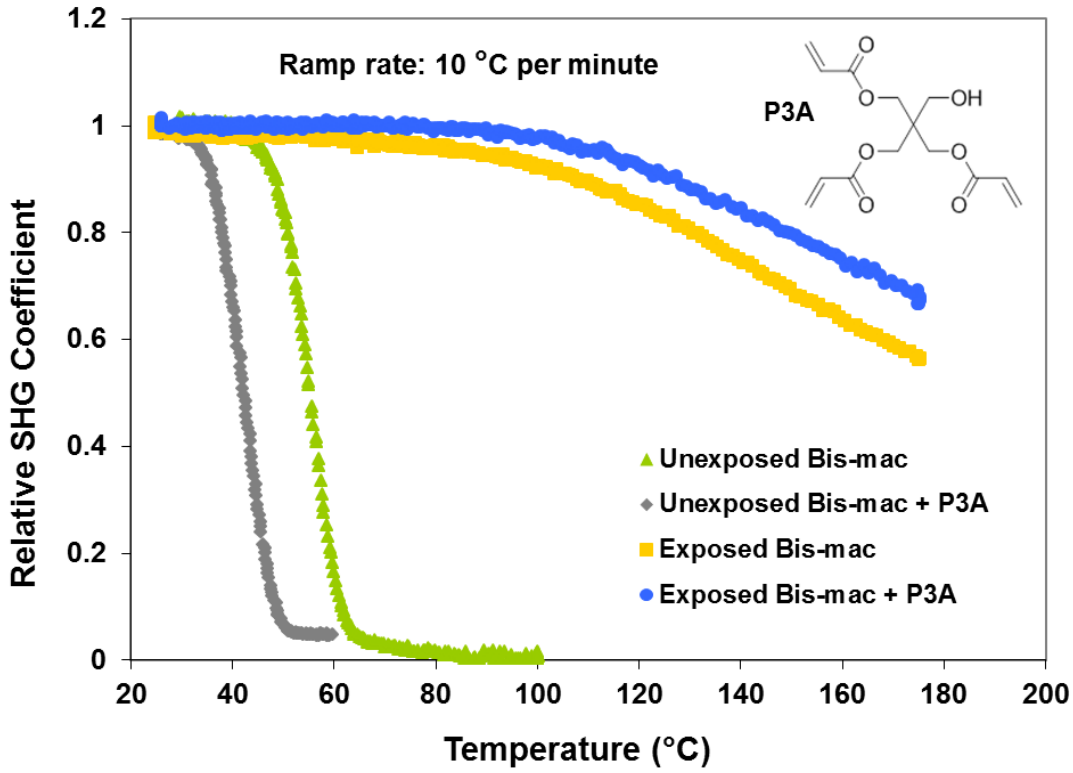

Figure 3.17: Relative SHG coefficients for poled Bis-mac samples incorporating a reactive diluent, including Bis-mac samples with and without exposure as a function of temperature during a 10 °C/min temperature ramp.

3.6 EXPERIMENTAL

All chemicals were purchased from Sigma-Aldrich Co. and used as received unless otherwise noted. Prior to use, IBA, EGDA, and P3A were filtered through basic alumina to remove inhibitor. Poled polymer solutions were formulated in solutions of cyclopentanone and stored in the dark. Solutions were spin coated at 1500 rpm and baked overnight in an 85 °C vacuum oven in the case of poled samples or on a 110°C hotplate for one minute in the case of unpoled samples.

ITO-coated glass substrates were purchased from Sigma-Aldrich and have a sheet resistance of 70 Ω/□. Substrates for contact poling were prepared by masking all but a portion of the area of the substrates with tape and etching the ITO with N/10 HCl solution (Fisher Scientific) prior to spin coating. Coated thicknesses were measured with a Dektak 6M stylus profiler (Veeco, Inc.). Gold was deposited onto the sample through a shadow mask by sputter coating (Electron Microscopy Sciences, Inc.). Electrodes were attached to needle micropositioners (Quater R&D, Inc.). Subsequent to poling, gold electrodes were etched by washing the samples with a 4:1:40 (by volume) solution of $KI:I_2:H_2O$ for 15 seconds. Poled samples were heated during poling using a Newport 3040 Temperature Controller and a thermoelectric module. LabVIEW software (National Instruments, Inc.) was used to control poling temperature and monitor current.

FTIR spectra were collected with a Magna 550 spectrometer (Thermo Scientific, Inc.). Samples were spin coated or drop-cast onto aluminum-coated silicon wafers and IR absorbance was measured in a normal specular reflectance configuration using a reflectance accessory (Axiom Analytical, Inc.) with nitrogen purging.

SHG data were collected as described in Chapter 2, with a 45° incident angle. Samples were mounted in a heater composed of two plates heated internally by flexible polyimide-coated nickel-chromium heaters with ¼" holes for beam clearance. Heating and data acquisition was controlled by LabVIEW software, with a 10 °C/min temperature ramp rate.

3.7 CONCLUSIONS

A series of tolane polymers incorporating zero, one, or two crosslinkable methacrylate groups were evaluated to determine the stabilizing effect of crosslinking across the chromophore. The crosslinking reaction was monitored by FTIR, allowing

insight into the effects of the photoinitiator, exposure source, and temperature during exposure. While all polymers show similar SHG activity following poling, thermal stability is significantly enhanced after photocrosslinking for Mono-mac and Bis-mac polymers, with Bis-mac being the most stable. Addition of the reactive diluent, pentaerythritol triacrylate, further enhances stability and allows for retention of 75% of the initial SHG coefficient for 60 hours at 100 °C. The materials investigated here are not optimized to maximize NLO coefficients, but the enhancement of thermal stability imparted to even a low T_g polymer effectively demonstrates the effect of photocrosslinking and suggests that further improvements may be realized with more efficient chromophores and higher T_g polymer backbones.

3.8 REFERENCES

1. Barto Jr, R. R.; Frank, C. W.; Bedworth, P. V.; Ermer, S.; Taylor, R. E., Near-infrared optical-absorption behavior in high-beta nonlinear optical chromophore-polymer guest-host materials. II. Dye spacer length effects in an amorphous polycarbonate copolymer host. *The Journal of chemical physics* **2005,** 122, 234907.

2. Zhang, C.; Dalton, L. R.; Oh, M.-C.; Zhang, H.; Steier, W. H., Low V Electrooptic Modulators from CLD-1: Chromophore Design and Synthesis, Material Processing, and Characterization. *Chemistry of Materials* **2001,** 13, (9), 3043-3050.

3. Kim, T.-D.; Kang, J.-W.; Luo, J.; Jang, S.-H.; Ka, J.-W.; Tucker, N.; Benedict, J. B.; Dalton, L. R.; Gray, T.; Overney, R. M.; Park, D. H.; Herman, W. N.; Jen, A. K. Y., Ultralarge and Thermally Stable Electro-Optic Activities from Supramolecular Self-Assembled Molecular Glasses. *Journal of the American Chemical Society* **2007,** 129, (3), 488-489.

4. Singer, K. D.; Kuzyk, M. G.; Holland, W. R.; Sohn, J. E.; Lalama, S. J.; Comizzoli, R. B.; Katz, H. E.; Schilling, M. L., Electro-optic phase modulation and optical second-harmonic generation in corona-poled polymer films. *Applied Physics Letters* **1988,** 53, (19), 1800-1802.

5. Hubbard, M. A.; Marks, T. J.; Yang, J.; Wong, G. K., Poled polymeric nonlinear optical materials. Enhanced second harmonic generation stability of crosslinkable matrix/chromophore ensembles. *Chemistry of Materials* **1989,** 1, (2), 167-169.

6. Mao, S. S. H.; Ra, Y.; Guo, L.; Zhang, C.; Dalton, L. R.; Chen, A.; Garner, S.; Steier, W. H., Progress toward Device-Quality Second-Order Nonlinear Optical Materials. 1. Influence of Composition and Processing Conditions on Nonlinearity, Temporal Stability, and Optical Loss. *Chemistry of Materials* **1998,** 10, (1), 146-155.

7. Wang, X.; Chen, J.-I.; Marturunkakul, S.; Li, L.; Kumar, J.; Tripathy, S. K., Epoxy-Based Nonlinear Optical Polymers Functionalized with Tricyanovinyl Chromophores. *Chemistry of Materials* **1997,** 9, (1), 45-50.

8. Hubbard, M. A.; Marks, T. J.; Lin, W.; Wong, G. K., Poled polymeric nonlinear optical materials. Enhanced second harmonic generation temporal stability of epoxy-based matrixes containing a difunctional chromophoric comonomer. *Chemistry of Materials* **1992,** 4, (5), 965-968.

9. Jungbauer, D.; Teraoka, I.; Yoon, D. Y.; Reck, B.; Swalen, J. D.; Twieg, R.; Willson, C. G., Second order nonlinear optical properties and relaxation characteristics of poled linear epoxy polymers with tolane chromophores. *Journal of Applied Physics* **1991,** 69, (12), 8011-8017.

10. Bai, Y.; Song, N.; Gao, J. P.; Sun, X.; Wang, X.; Yu, G.; Wang, Z. Y., A New Approach to Highly Electrooptically Active Materials Using Cross-Linkable, Hyperbranched Chromophore-Containing Oligomers as a Macromolecular Dopant. *Journal of the American Chemical Society* **2005,** 127, (7), 2060-2061.

11. Shi, Z.; Luo, J.; Huang, S.; Cheng, Y.-J.; Kim, T.-D.; Polishak, B. M.; Zhou, X.-H.; Tian, Y.; Jang, S.-H.; Knorr, J. D. B.; Overney, R. M.; Younkin, T. R.; Jen, A. K. Y., Controlled Diels−Alder Reactions Used To Incorporate Highly Efficient Polyenic Chromophores into Maleimide-Containing Side-Chain Polymers for Electro-Optics. *Macromolecules* **2009,** 42, (7), 2438-2445.

12. Kim, T.-D.; Luo, J.; Tian, Y.; Ka, J.-W.; Tucker, N. M.; Haller, M.; Kang, J.-W.; Jen, A. K. Y., Diels-Alder "Click Chemistry" for Highly Efficient Electrooptic Polymers. *Macromolecules* **2006,** 39, (5), 1676-1680.

13. Kuo, Y. H.; Luo, J.; Steier, W. H.; Jen, A. K. Y., Enhanced thermal stability of electrooptic polymer modulators using the Diels-Alder crosslinkable polymer. *IEEE Photonics Technology Letters* **2006,** 18, (1), 175-177.

14. Shi, Z.; Liang, W.; Luo, J.; Huang, S.; Polishak, B. M.; Li, X.; Younkin, T. R.; Block, B. A.; Jen, A. K. Y., Tuning the Kinetics and Energetics of Diels−Alder Cycloaddition Reactions to Improve Poling Efficiency and Thermal Stability of High-Temperature Cross-Linked Electro-Optic Polymers. *Chemistry of Materials* **2010,** 22, (19), 5601-5608.

15. Lee, S. K.; Cho, M. J.; Jin, J.-I.; Choi, D. H., Stability control of the electrooptic effect with new maleimide copolymers containing photoreactive tricyanopyrrolidene-based chromophores. *Journal of Polymer Science Part A: Polymer Chemistry* **2007,** 45, (3), 531-542.

16. Betterton, K.; Ebert, M.; Haeussling, L.; Lux, M. G.; Twieg, R. J.; Willson, C. G.; Yoon, D.; Burns, E. G.; Grubbs, R., Strategies for crosslinking NLO polymers across the chromophore. *Polymeric Materials Science and Engineering* **1992,** 66, 312-13.

17. Godt, A.; Fréchet, J. M. J.; Beecher, J. E.; Willand, C. S., Photopolymers for non-linear optics: Design and synthesis of a polymer containing styrene-terminated tolane chromophores and its stabilization in an oriented configuration by photocrosslinking. *Macromolecular Chemistry and Physics* **1995,** 196, (1), 133-147.

18. Morichere, D.; Chollet, P. A.; Fleming, W.; Jurich, M.; Smith, B. A.; Swalen, J. D., Electro-optic effects in two tolane side-chain nonlinear-optical polymers: comparison between measured coefficients and second-harmonic generation. *Journal of the Optical Society of America B: Optical Physics* **1993,** 10, (10), 1894-900.

19. Love, J. A.; Morgan, J. P.; Trnka, T. M.; Grubbs, R. H., A Practical and Highly Active Ruthenium-Based Catalyst that Effects the Cross Metathesis of Acrylonitrile. *Angewandte Chemie International Edition* **2002,** 41, (21), 4035-4037.

20. Scholl, M.; Ding, S.; Lee, C. W.; Grubbs, R. H., Synthesis and Activity of a New Generation of Ruthenium-Based Olefin Metathesis Catalysts Coordinated with 1,3-Dimesityl-4,5-dihydroimidazol-2-ylidene LigandsÂ§. *Organic Letters* **1999,** 1, (6), 953-956.

21. Schwab, P.; France, M. B.; Ziller, J. W.; Grubbs, R. H., A Series of Well-Defined Metathesis Catalysts–Synthesis of [RuCl2 (□ CHR′)(PR3) 2] and Its Reactions. *Angewandte Chemie International Edition in English* **1995,** 34, (18).

22. Leitgeb, A.; Wappel, J.; Slugovc, C., The ROMP toolbox upgraded. *Polymer* **2010,** 51, (14), 2927-2946.

23. Marder, S. R.; Perry, J. W., Nonlinear Optical Polymers: Discovery to Market in 10 Years? *Science* **1994,** 263, 1706-1707.

24. Chafin, A. P.; Lindsay, G. A., A Pattern for Increasing the First Hyperpolarizability of a Push-Pull Polyene Dye as Indicated from DFT Calculations. *The Journal of Physical Chemistry C* **2008,** 112, (21), 7829-7835.

25. Dalton, L. R., Organic electro-optic materials. Past, present, and future. *PMSE Preprints* **2003,** 88, 173-174.

26. Long, B. Design, Synthesis, and Application of Lithographic Resists and Nonlinear Optical Materials. University of Texas at Austin, Austin, 2009.

27. Contreras, A. P.; Tlenkopatchev, M. A.; del Mar Lopez-Gonzalez, M.; Riande, E., Synthesis and Gas Transport Properties of New High Glass Transition Temperature Ring-Opened Polynorbornenes. *Macromolecules* **2002,** 35, (12), 4677-4684.

28. Wang, Z.; Sun, W.; Chen, A.; Kosilkin, I.; Bale, D.; Dalton, L. R., Organic electro-optic thin films by simultaneous vacuum deposition and laser-assisted poling. *Opt. Lett.* **2011,** 36, (15), 2853-2855.

29. Sprave, M.; Blum, R.; Eich, M., High electric field conduction mechanisms in electrode poling of electro-optic polymers. *Applied Physics Letters* **1996,** 69, (20), 2962-2964.

30. Blum, R.; Sprave, M.; Sablotny, J.; Eich, M., High-electric-field poling of nonlinear optical polymers. *JOSA B* **1998,** 15, (1), 318-328.

31. Huang, S.; Kim, T. D.; Luo, J.; Hau, S. K.; Shi, Z.; Zhou, X. H.; Yip, H. L.; Alex, K. Y. J., Highly efficient electro-optic polymers through improved poling using a thin TiO-modified transparent electrode. *Applied Physics Letters* **2010,** 96, 243311.

32. Giacometti, J. A.; Campos, J. S. C., Constant current corona triode with grid voltage control. Application to polymer foil charging. *Review of Scientific Instruments* **1990,** 61, (3), 1143-1150.

33. Hill, R. A.; Knoesen, A.; Mortazavi, M. A., Corona poling of nonlinear polymer thin films for electro-optic modulators. *Applied Physics Letters* **1994,** 65, (14), 1733-1735.

34. Stansbury, J. W.; Dickens, S. H., Determination of double bond conversion in dental resins by near infrared spectroscopy. *Dent Mater* **2001,** 17, (1), 71-9.

35. Shanmuganathan, K.; Sankhagowit, R. K.; Iyer, P.; Ellison, C. J., Thiol–Ene Chemistry: A Greener Approach to Making Chemically and Thermally Stable Fibers. *Chemistry of Materials* **2011,** 23, (21), 4726-4732.

36. Cramer, N. B.; Bowman, C. N., Kinetics of thiol–ene and thiol–acrylate photopolymerizations with real-time fourier transform infrared. *Journal of Polymer Science Part A: Polymer Chemistry* **2001,** 39, (19), 3311-3319.

37. Roper, T. M.; Guymon, C.; Jönsson, E.; Hoyle, C., Influence of the alkene structure on the mechanism and kinetics of thiol–alkene photopolymerizations with real-time infrared spectroscopy. *Journal of Polymer Science Part A: Polymer Chemistry* **2004,** 42, (24), 6283-6298.

38. Lee, T. Y.; Roper, T. M.; Jonsson, E. S.; Kudyakov, I.; Viswanathan, K.; Nason, C.; Guymon, C.; Hoyle, C., The kinetics of vinyl acrylate photopolymerization. *Polymer* **2003,** 44, (10), 2859-2865.

39. Neumann, M. G.; Miranda Jr, W. G.; Schmitt, C. C.; Rueggeberg, F. A.; Correa, I. C., Molar extinction coefficients and the photon absorption efficiency of dental photoinitiators and light curing units. *Journal of Dentistry* **2005,** 33, (6), 525-532.

40. Tehfe, M.-A.; Blanchard, N.; Fries, C.; Lalevée, J.; Allonas, X.; Fouassier, J. P., Bis(germyl)ketones: Toward a New Class of Type I Photoinitiating Systems Sensitive Above 500 nm? *Macromolecular Rapid Communications* **2010,** 31, (5), 473-478.

41. Decker, C., Kinetic study and new applications of UV radiation curing. *Macromolecular Rapid Communications* **2002,** 23, (18), 1067-1093.

Chapter 4: Dual-tone Photoresist

4.1 INTRODUCTION

4.1.1 Overlay and alignment

Controlling overlay and alignment is an important requirement of multistep lithography patterning. The conformal nature of large area and flexible substrates limits the accuracy of alignment and overlay that can be acheived during the patterning of these materials. Overlay problems can be caused by applied forces on the substrates during processing, or by stress and strain mismatches between a deposited layer and an underlying material.[1, 2] Such processes induce curvature in the substrate, and a variable radius of curvature across the substrate leads to misalignment.[3] Transistor function depends on the overlay alignment of the gate to the source and drain isolation region.

One remedy to overlay misalignment on flexible substrates is the use of self-aligned structures that can be patterned in a single lithographic exposure, a process first implemented by Hinsberg *et al*.[4] This eliminates the problem of aligning a mask with a patterned layer on a flexible substrate and replaces it with the problem of alignment of two layers on a single mask (or two single-layer masks), minimizing the impact of substrate distortions. A self-aligned, single exposure process is shown in Figure 4.1. The two most important features are a dichroic mask and a dual-tone photoresist. In contrast to a traditional photomask, which has regions that are either completely transparent or completely opaque, a dichroic mask has three regions, one that is completely transparent, another that is completely opaque, and another that transmits light of one wavelength range while absorbing and reflecting other wavelengths.

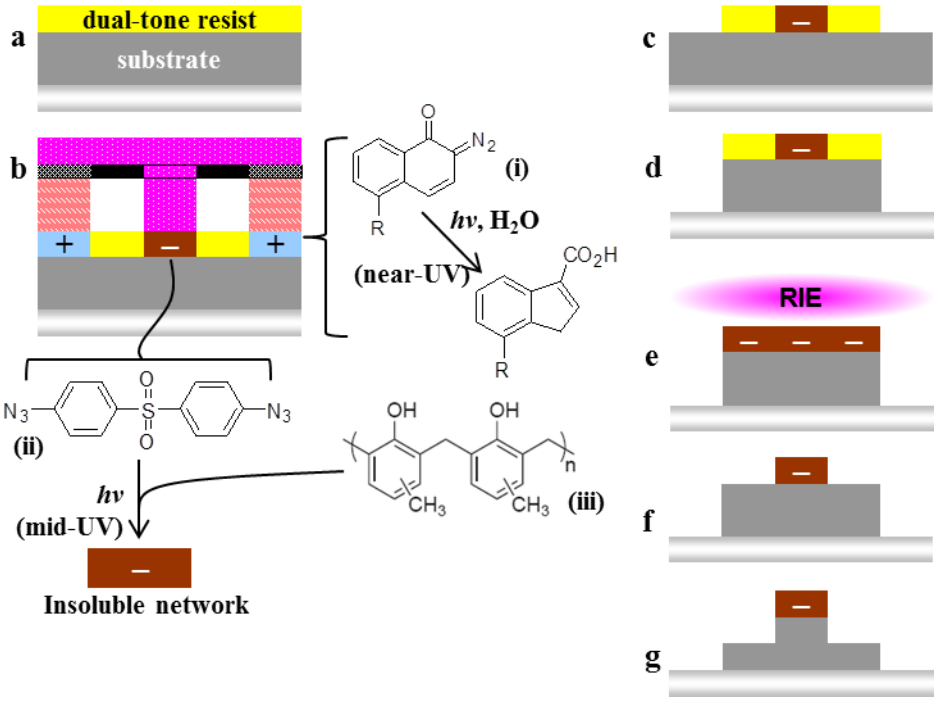

Figure 4.1: Overview of the Hinsberg dual-tone lithographic process for patterning of self-aligned structures. a) The substrate coated with a dual-tone photoresist film. b) After dual-tone exposure using a dichromatic photomask. In the region exposed to near-UV light, the DNQ (i) undergoes photochemical transformations that cause an increase in the solubility of the resist. In the region exposed to mid-UV light, the bis(azidophenyl)sulfone crosslinker (ii) undergoes photolysis to produce reactive intermediates that react with and crosslink the novolak resin which renders it insoluble (iii). c) Development produces the positive-tone image but neither the unexposed or crosslinked areas dissolve. d) A wet etch can be used to transfer the positive-tone image into the substrate. e) Flood exposure with near-UV light then renders the unexposed regions soluble and subsequent development leaves behind only the "hidden", crosslinked negative-tone image. f) A second etch transfers the negative-tone image into the substrate. g) Reactive ion etch (RIE) processes produce mid-UV light and therefore inadvertently expose the unexposed areas of the dual-tone resist, causing loss of the negative-tone latent image.

The Hinsberg-type dual-tone photoresist dual-tone photoresist allows patterning of more than one layer at a time in conjunction with a dichroic mask.[5] Just as a dichroic mask has three regions defined by the wavelengths that are transmitted, the dual-tone

resist must be able to store and transfer multiple images differentiated by the wavelength of the incident UV light. This is most straightforwardly accomplished by combining a negative-tone resist with a positive-tone resist. To achieve spectral selectivity, the light-sensitive compounds in the positive- and negative- tone components must be active at different wavelengths. For many applications involving flexible and large-area substrates, the critical dimensions are relatively large, on the order of a micron, so that a large range of spectrum is available for exposure. The Hinsberg implementation builds on an Hg i-line photoresist, consisting of a novolak resin, and a diazonaphthoquinone (DNQ) photoactive compound (PAC). In areas exposed to only near-UV light (320–450 nm), the DNQ PAC undergoes photo-decomposition. The unreacted DNQ is a dissolution inhibitor, but the rearranged carboxylic acid derivative is a dissolution promotor. In the exposed areas the resist film becomes more soluble in aqueous base developer, producing a positive-tone image of the mask.

In order to add a negative-tone functionality, a light-sensitive crosslinker, bis(azideophenyl)sulfone, is added to the positive i-line UV photoresist. Bis-azide crosslinkers have been commonly employed as crosslinkers in negative-tone photoresists[6] and have also been used in electron beam lithography resists.[7] In areas exposed with mid-UV light (250–320 nm), the bis(azidophenyl)sulfone undergoes photolysis which leads to cross-linking reactions with the phenolic resin that reduce the photoresist's solubility in basic developer and produce the negative-tone image.

Conveniently, the same negative-tone behavior occurs if the resist is exposed to both near-UV and mid-UV light, because the dissolution inhibition effect of the cross-linking reactions overwhelms the dissolution promotion effect of the photo-decomposed PAC. This spectral selectivity enables the dual-tone photoresist to store two distinct latent

images based on the wavelength of the incident exposure light, allowing the patterning of two device layers in one lithographic exposure step.

During the exposure process, a dichromatic mask allows for the simultaneous exposure of distinct photoresist regions to different wavelengths of UV light to produce either positive-tone or negative-tone latent images. Alternatively, it is also possible to carry out sequential aligned exposures using different wavelengths of UV light to produce the positive-tone and negative-tone latent images. In the latter case, the exposures must be carried out without moving the flexible substrate. The latent images are then processed to produce the two layer self-aligned structures by a sequence of selective development and etch steps.

4.1.2 Reactive ion etch compatibility

Note that in the process described, a portion of the unexposed and the negative-tone latent image photoresist must withstand several development and etch steps. In particular, as shown in Figure 4.1(e), the photoresist undergoes a development step after the first transfer etch, in contrast to the usual process in which the photoresist is removed immediately followed the transfer etch. In the photoresist system reported by Hinsberg et al., a wet etch process was used to transfer the positive-tone image into the substrate, while maintaining the unexposed and negative-tone images in the photoresist [Figure 4.1(d)]. However, when a reactive ion etch (RIE) process is applied for the same etch transfer of positive-tone image, the unexposed region undergoes inadvertent exposure and the latent image is lost. The loss of the latent image is attributed to the production of UV radiation by the etchant gas plasma during the RIE process, resulting in the photoresist being unintentionally flood exposed as it is being etched. This flood exposure causes the cross-linking reaction to occur between the novolak polymer and the negative-

tone sensitizer, producing a negative-tone response in the entire photoresist film and erasing the negative-tone/unexposed latent image, as shown in Figure 4.1(g).

The negative-tone latent image can be preserved through the RIE step by strengthening the requisite conditions of the negative-tone exposure response. Requiring an additional bake step during or after the exposure allows for inadvertent exposure to be distinguished from intentional exposure. To implement this, a variation on the above-mentioned novolak/PAC based dual-tone photoresist system was designed. It incorporates a thermally activated, chemically amplified cross-linker and a photoacid generator (PAG). The process is shown in Figure 4.2. Because this work focuses on the function of the photoresist, a series of sequential exposures of different wavelengths through two binary photomasks [Figure 4.2(a)] served as a convenient method of producing a dichromatic image in the laboratory rather than using a dichroic mask, although either method can be used to produce the resist response, since the response is not time-dependent. The first exposure was done using a broadband UV medium pressure mercury arc lamp spot curing system with a 345 nm long pass filter, and the second exposed with no filter.

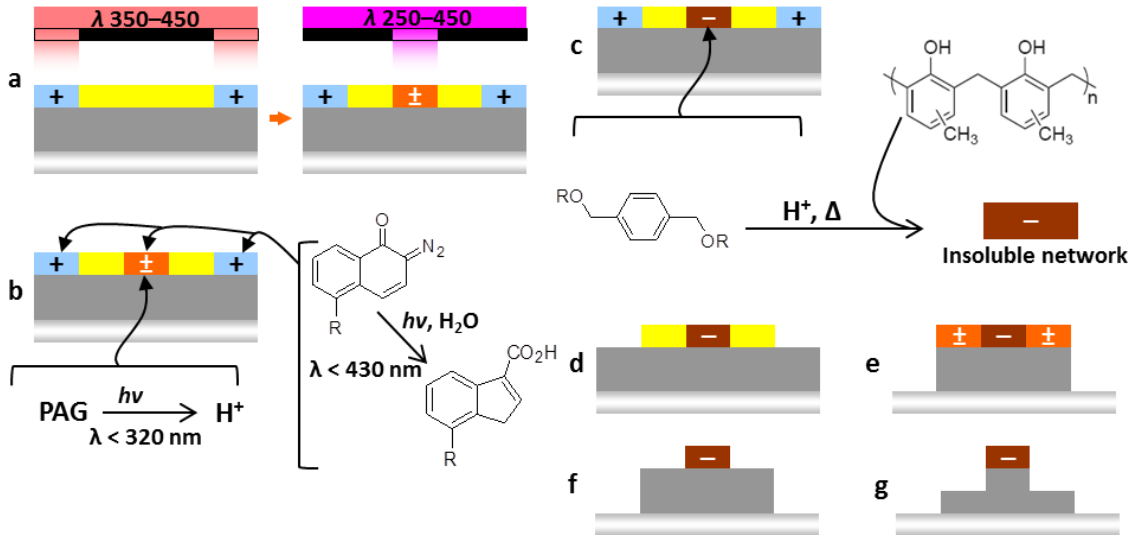

Figure 4.2: Overview of the improved dual-tone lithographic process demonstrated in this work: a) Sequential exposure at different wavelengths of a stationary substrate through monochromatic masks produces a dose pattern equivalent to that generated by a dichromatic mask. b) The positive-tone latent image is formed by photolysis of the dissolution inhibitor DNQ in regions exposed to <430 nm wavelength UV. An acid latent image is formed in regions exposed to <320 nm wavelength UV light by photolysis of the PAG. c) The acid latent image is converted into a latent negative-tone image by aid catalysis of a reaction between the crosslinker and the phenolic polymer, which forms an insoluble network. This reaction requires both acid and heat. d) Development in aqueous base removes the exposed, uncross-linked positive-tone regions while leaving both the cross-linked and unexposed regions. e) RIE transfers the positive-tone image. The light from the plasma exposes the resist, causing both rearrangement of the DNQ and generation of acid, but no reaction with the crosslinker occurs in the absence of heat. f) The exposed, but uncross-linked region is removed by aqueous base developer to reveal the "hidden" latent negative tone image. g) The negative-tone image is transferred in a second RIE etch.

In the new system, the rearrangement of the DNQ PAC occurs in the positive region as before [Figure 4.2(b)]. However, in this design, a photoacid generator (PAG) provides the spectral selectivity for the negative-tone response by producing an acid latent image in regions exposed at wavelengths below 320 nm. The negative-tone response is an acid catalyzed cross-linking reaction that requires thermal activation.

Hence, the generation of the negative-tone response requires both exposure and baking. It is this bake requirement that distinguishes this process from that of Hinsberg and enables differentiation between the intentional negative-tone exposure of the lithography step and the unavoidable flood exposure during the plasma etch step [Figure 4.2(e)], allowing the negative-tone latent image to survive the RIE process and be developed and transferred [Figure 4.2(f,g)]. Several chemicals were evaluated for their suitability as the cross-linker and PAG in such a system. The results of these experiments are described in the following sections.

4.2 NEGATIVE-TONE COMPONENTS

4.2.1 Crosslinkers

The crosslinker enables the novolak resin in the photoresist to undergo crosslinking, reducing its solubility in the developer solvent and imparting a negative-tone response into the photoresist system. Several candidate compounds were tested for their compatibility with the novolak / DNQ photoresist formulation and their cross-linking performance.

In an attempt to replicate previous formulations of dual-tone photoresists, the bis-azide sulfone derivatives were added to novolak / DNQ mixtures. However, both bis(4-azidophenyl) sulfone and bis(3-azidophenyl) sulfone cross-linkers had poor solubility in PGMEA, a standard solvent for the commercial novolak photoresist; as a result neither formulation produced sufficient cross-linking to enable a negative-tone photoresist response.

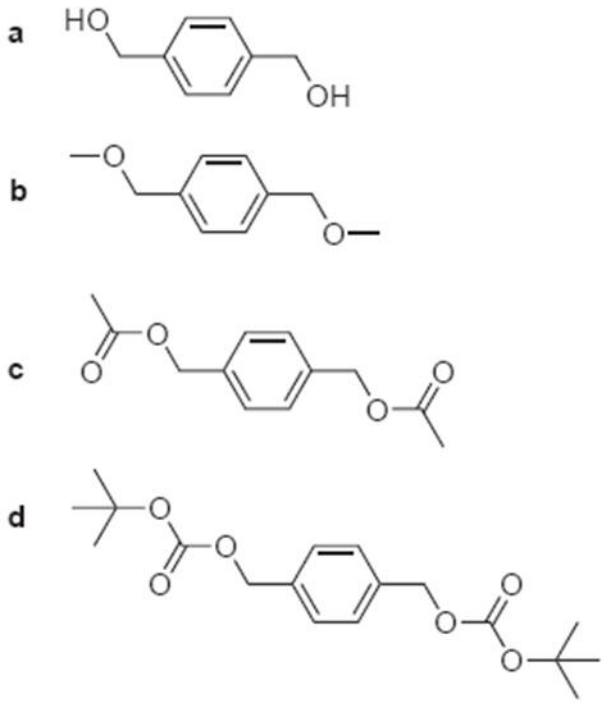

Figure 4.3: Cross-linker candidates for the development of dual-tone photoresist: a) 1,4-benzenedimethanol; b) 1,4-bis-methoxymethyl-benzene; c) 1,4-bis-acetoxymethyl-benzene; d) 1,4-bis-tertbutoxycarbonyloxymethyl-benzene.

The 1,4-benzenedimethanol ('diol') and its derivatives 1,4-bis-methoxymethyl-benzene ('methoxy'), 1,4-bis-acetoxymethyl-benzene ('acetoxy'), and 1,4-bis-tertbutoxycarbonyloxymethyl-benzene ('t-boc') (Figure 4.3) all have moderate solubility in PGMEA, and successfully produced negative-tone response with the application of acid and heat. The derivatives differ in the acid labile protecting group used to cap the methanol cross-linking functionality: methoxy, acetoxy, and tertbutoxycarbonyloxy ('t-boc'). The influence of the protecting groups on negative-tone response of the dual-tone photoresist was measured by the change in the threshold post exposure bake (PEB) temperature required for the negative-tone cross-linking reaction. This was determined by measuring the remaining film thickness after a 60-second unfiltered broadband UV

exposure followed by a 110 °C, 60-second PEB and a 60-second dip in 0.26 N TMAH developer. The different protecting groups were expected to have a significant effect on the crosslinking temperature required for negative tone response, which was presumed to be mediated by the benzyl carbocation formed by acid-catalyzed hydrolysis. In fact, the effects of the different protecting groups were found to be less than expected. As shown in Figure 4.4, the change in threshold PEB temperature across the four different cross-linkers was less than 20 °C, and all of the structures were able to produce sufficient cross-linking reactions at 110 °C PEB temperature to realize the negative-tone image. As a result, the commercially available 1,4-benzenedimethanol (Sigma-Aldrich Co), was chosen for all subsequent dual-tone photoresist formulations.

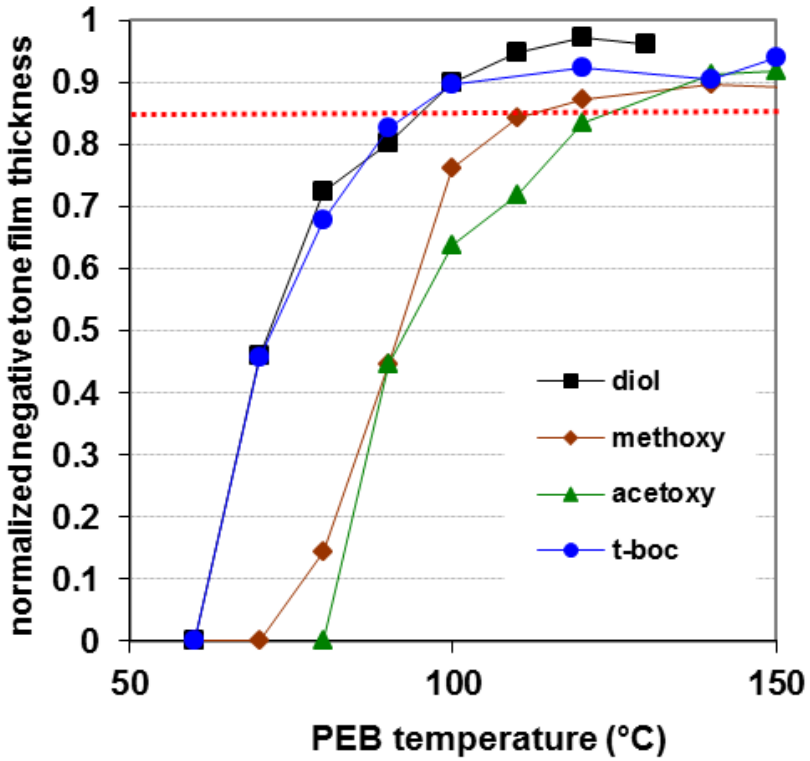

Figure 4.4: Negative-tone exposure response as a function of post-exposure bake (PEB) temperature for derivatives of 1,4-benzenedimethanol ('diol') with different protecting groups: 'methoxy', 'acetoxy', and 't-boc' (see Figure ???). Normalized negative tone film thickness is the remaining film thickness after a 60-second unfiltered broadband UV exposure followed by a 110 °C, 60-second PEB and a 60-second dip in 0.26 N TMAH developer, divided by the original film thickness.

4.2.2 Photoacid Generators

The photoacid generator (PAG) additive provides the acid catalyst that initiates the negative-tone exposure response of the photoresist. During UV light exposure, the PAG undergoes photolysis, producing strong acid in a latent image. Upon subsequent heating of the photoresist, the acid generates benzylic carbocations from the cross-linkers. These carbocations can react with the phenolic units of the novolak polymer, forming ethereal linkages or undergo electrophilic aromatic substitution yielding carbon-

carbon bond cross-links.[8] The cross-linked novolak polymer becomes less soluble to the aqueous base developer, producing the negative-tone image. A variety of PAGs with different UV absorption spectra are available, allowing the PAG to be independently chosen to ensure little spectral overlap of the negative-tone exposure response with that of the positive-tone PAC. Figure 4.5 shows UV-vis spectra and structures of individual photoactive components in solution. Most positive-tone i-line resists use proprietary DNQ dissolution inhibitors, so a substitute DNQ (IBM Almaden Research Center), 1-Naphthalenesulfonic acid, 6-diazo-5,6-dihydro-5-oxo-, 1,1'-[(octahydro-4,7-methano-1H-indene-2,5-diyl)bis(methylene)] ester was used as a representative of the resist positive-tone PAC. The positive-tone DNQ has a broad absorption band between 200 and 440 nm, while triphenylsulfonium perfluorobutanesulfonate (TPS nonaflate), a commercially available PAG, only strongly absorbs up to 290 nm.

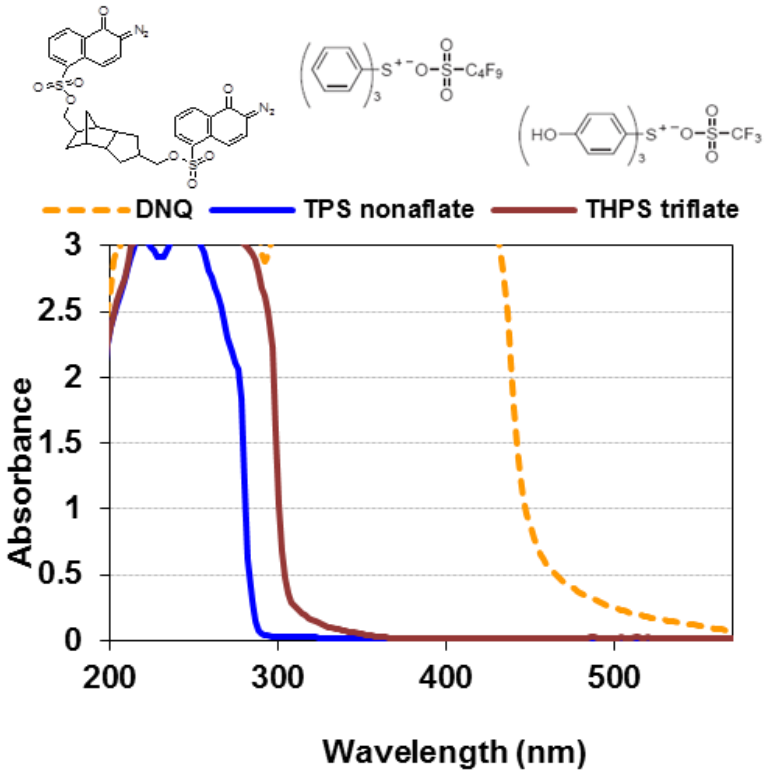

Figure 4.5: UV-Vis absorption spectra and structures of photoacid generators (TPS nonaflate and THPS triflate) and photoactive compound (DNQ).

Initial print tests of dual-tone photoresist with TPS nonaflate demonstrated good negative-tone exposure response, produced the negative latent image as designed, and showed that the resist was capable of tolerating the RIE process. However, it was soon noted that the addition of the negative-tone additives into the novolak / DNQ formulation significantly reduced the dissolution rate of the novolak polymer in aqueous base developer, suppressing the photoresist's positive-tone exposure response. The decrease in the dissolution rate can be compensated for by increasing the exposure dose (especially for the positive tone exposures) and increasing the develop time. However, these produced additional problems such as blurred images and photoresist swelling, as well as

unintentional lift-off of the negative tone, which occurs after long development times or with shaking.

In order to identify the impact of various individual negative-tone additives on the positive-tone dissolution of the resist, the dissolution rate of the novolak / DNQ photoresist was measured after positive-tone exposure. Figure 4.6 shows the dissolution inhibition effect of several combinations of novolak / DNQ photoresist with PAGs and cross-linkers. The figure shows the time required for the positive-tone exposed region to fully dissolve in the aqueous base developer following UV exposures of various times and a 60-second, 110 °C PEB. The addition of the TPS nonaflate was found to be the most significant contributor to the suppression of the positive-tone dissolution rate, tripling the required time in developer; while the cross-linkers yielded comparatively minor increases in develop time. This phenomenon has been reported previously and exploited in the design of positive-tone photoresists by Chambers *et al*.[9]

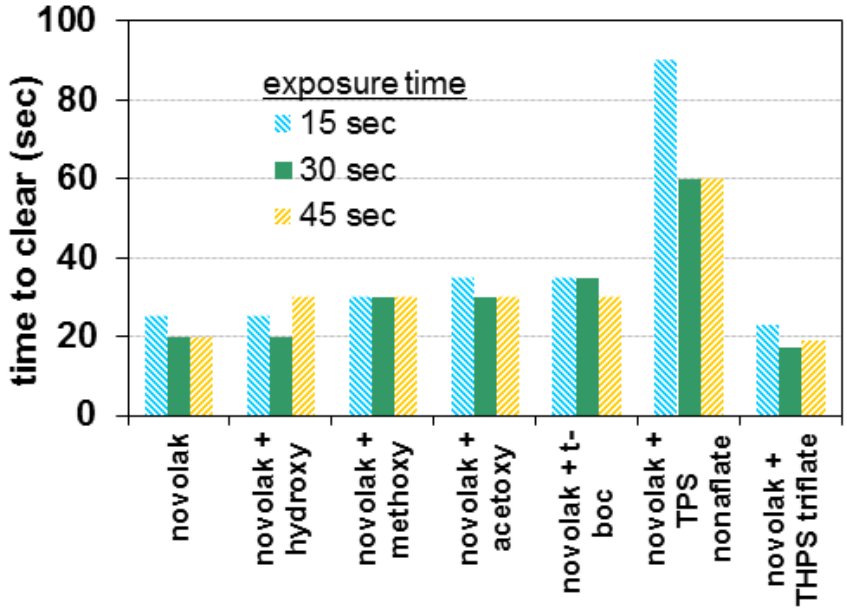

Figure 4.6: The dissolution inhibition effect of several combinations of novolak / DNQ photoresist with PAGs and cross-linkers as illustrated by the time required for the positive-tone exposed region to fully dissolve in aqueous base developer after UV exposure and a 60-second, 110 °C PEB.

The dissolution inhibition effect of the TPS nonaflate can be mitigated by rendering the PAG molecule base soluble. This was accomplished by introducing phenolic hydroxyl groups on the phenyl groups of the PAG. The resulting compound, tris(4-hydroxyphenyl)sulfonium trifluoromethanesulfonate (THPS triflate), is freely soluble in aqueous base and has an UV absorption drop off around 310 nm (Figure 4.5), similar to that of TPS nonaflate. This enabled THPS triflate spectral differentiation from the positive-tone DNQ during the exposure process. THPS triflate did not exhibit any dissolution inhibition effects, restoring the novolak resin's original positive-tone development rate (Figure 4.6) while maintaining its negative-tone response capability. While THPS triflate is the ideal PAG for the dual-tone photoresist application, it is not

yet commercially available in quantities suitable for functional formulations of the dual-tone photoresist for device testing, so these were prepared from TPS nonaflate.

4.3 DUAL-TONE PATTERNING

Top-down optical microscope images and profilometer traces of a patterned photoresist sample after dual-tone exposure and positive-tone image development are shown in Figure 4.7(a). The optical image (right column) shows a sample device area, with a solid line denoting the profilometer trace area across the positive-tone photoresist. The profilometer trace (center column) shows a 900 nm tall photoresist structure after the positive-tone development.

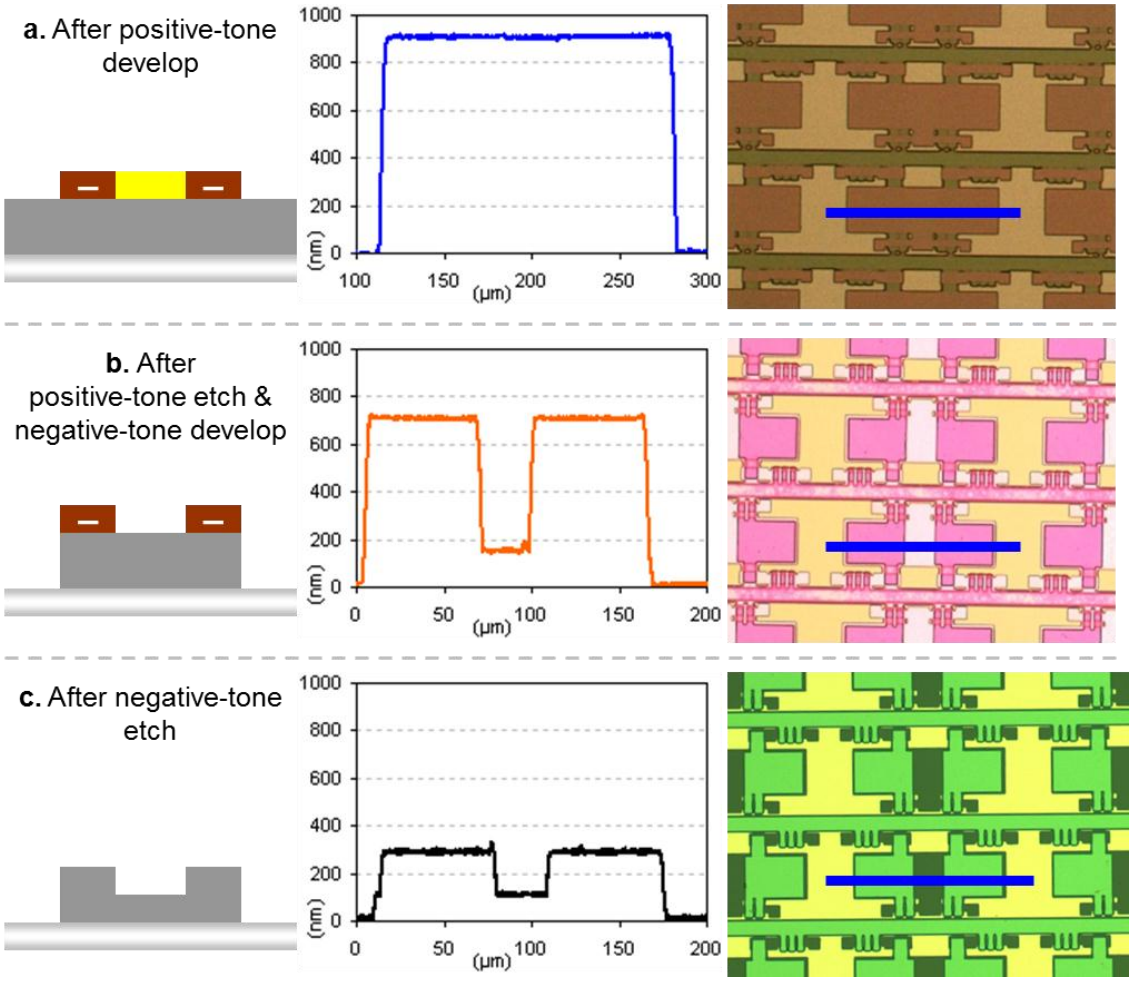

Figure 4.7: Profilometer traces and optical microscope images of patterned dual-tone photoresist sample: (a) after developing the positive-tone image; (b) after transferring the positive-tone image into the substrate by reactive ion etching and then developing the negative-tone image; (c) after transferring the negative tone image by RIE and stripping the photoresist.

The sample was then etched by RIE to transfer the positive-tone image into the substrate, and developed again to remove previously unexposed photoresist, leaving behind the negative-tone device image. The development of the etched photoresist is inhibited by the formation of an insoluble crust that forms on top of the etched photoresist. Using a short (< 1 min) oxygen plasma descum etch, the crust layer was

removed, allowing the resist to be developed, although the development time was extended to several minutes to ensure complete removal of resist. Figure 4.7(b) shows the top-down image of the dual-tone photoresist sample with the positive-tone image etched into the substrate and negative-tone photoresist image left. The profilometer trace shows approximately 550 nm of photoresist remaining after the positive-tone structures are etched into the silicon substrate.

Finally, the sample was etched again by RIE to transfer the negative-tone image into the substrate, and then stripped of the photoresist, leaving behind the two layers of device structures in the substrate. Figure 4.7(c) shows the top-down image of the dual-tone photoresist sample with both positive-tone and negative-tone images etched into the substrate. The profilometer trace shows ~100 nm tall positive-tone structures and ~200 nm tall negative-tone structures.

4.4 EXPERIMENTAL

All chemicals were purchased from Sigma-Aldrich and used as received unless otherwise stated. All reactions were conducted under a positive nitrogen atmosphere with oven-dried glassware unless otherwise stated. Dry dichloromethane (DCM), triethylamine (TEA), and pyridine were obtained by distillation over CaH_2 while dry THF was obtained by distillation over Na/benzophenone. All ^{1}H and ^{13}C NMR spectra were recorded on a Varian Unity Plus 400 MHz instrument. All chemical shifts are reported in ppm downfield from TMS using the residual protonated solvent as an internal standard ($CDCl_3$, ^{1}H 7.26 ppm and ^{13}C 77.0 ppm). High resolution mass spectrometry (HMRS) was obtained on a VG analytical ZAB2-E instrument. UV-vis data was recorded with an HP 8452A diode array photospectrometer. IR data was recorded on a Nicolet Avatar 360 FT-IR and all peaks are reported in cm^{-1}.

The base developer, AZ 300 MIF, consisting of aqueous tetramethylammonium hydroxide solution (0.261 N), was purchased from AZ Electronic Materials USA Corp. The i-line positive-tone photoresist, consisting of novolak polymer and DNQ PAC in propylene glycol monomethyl ether acetate (PGMEA) solvent, was obtained as a generous gift from the AZ Electronic Materials, as was a sample of TPS nonaflate.

A sample of tris(4-hydroxyphenyl)sulfonium chloride was obtained as generous gift from BASF SE. Synthesis of THPS triflate is done by anion metathesis of tris(4-hydroxyphenyl)sulfonium chloride and silver trifluoromethanesulfonate.

To synthesize 1,4-bis-acetoxymethy-benzene, a 50 mL round bottom flask (RBF) was charged with dimethylaminopyridine (88 mg, 0.7 mmol), acetic anhydride (13.7 mL, 145.0 mmol), pyridine (11.7 mL, 145.0 mmol), 1,4-benzenedimethanol (2.0 g, 14.5 mmol), and a stir bar. This solution was stirred at rt for 24 h then diluted with ether (200 mL). The organic layer was thoroughly rinsed with 1 *M* KOH (4 x 100 mL), followed by rinsing with 1 *M* $CuSO_4$ (2 x 50 mL). The organic layers were combined, dried over $MgSO_4$, and concentrated *in vacuo* to yield 1,4-bis-acetoxymethyl-benzene as a white crystalline solid (mp = 54-56 °C) (20.7 g, 89%); ^{1}H NMR ($CDCl_3$) δ ppm: 7.351 (s, 4H), 5.094 (s, 4H), 2.090 (s, 6H); ^{13}C NMR ($CDCl_3$) δ ppm: 170.736, 135.932, 128.386, 65.811, 20.909; IR (NaCl) cm^{-1}: 2960, 2897, 1722, 1227, 1018; HRMS (CI): 245.0787 calc, 245.0784 found.

To synthesize 1,4-bis-methoxymethyl-benzene, 50 mL RBF was charged with NaH (2.3 g, 57.9 mmol, 60% dispersion in mineral oil), THF (10 mL), and a stir bar. The suspension was vigorously stirred as 1,4-benzenedimethanol (2.0 g, 14.5 mmol) was added slowly at rt. Upon complete evolution of gas, iodomethane (9.0 mL, 145 mmol) was slowly added. The solution was stirred for 24 h, and then the excess iodomethane was removed *in vacuo*. The remaining suspension was dissolved in ether, and the salts

were removed by filtration. 1,4-bis-methoxymethyl-benzene was isolated by distillation (75-77 °C, 0.83 torr) in good yield (2.0 g, 81%) as a clear liquid; ^{1}H NMR ($CDCl_3$) δ ppm: 7.301 (s, 4H), 4.425 (s, 4H), 3.351 (s, 6H); ^{13}C NMR ($CDCl_3$) δ ppm: 137.406, 127.546, 74.189, 57.784; IR (NaCl) cm^{-1}:2982, 2925, 2852, 1380, 1123, 1099, 809; HRMS (CI): 165.0916 calc, 165.0922 found.

To synthesize 1,4-bis-tertbutoxycarbonyloxymethyl-benzene, a 100 mL RBF was charged with imidazole (40 mg, 0.6 mmol), di-tert-butyl di-carbonate (758 mg, 3.5 mmol), toluene (30 mL), THF (5 mL), and a stir bar. After stirring for 10 min, 1,4-benzenedimethanol (200 mg, 1.5 mmol) was added, and the reaction was stirred at rt for 48 h. DCM was added to the reaction which was then rinsed with brine, dried over $MgSO_4$, and concentrated *in vacuo*. This crude mixture was subjected to flash column chromatography (9:1 Hex:EtOAc) to yield 1,4-bis-tertbutoxycarbonyloxymethyl-benzene as a white crystalline solid in moderate yield (234 mg, 49.6%); mp = 71-74 °C; ^{1}H NMR ($CDCl_3$) δ ppm: 7.364 (s, 4H), 5.079 (s, 4H), 1.482 (s, 18H); ^{13}C NMR ($CDCl_3$) δ ppm: 153.368, 135.772, 128.373, 82.331, 68.246, 27.739; IR (KBr) cm^{-1}:2984, 1738, 1396, 180, 1157, 1087; HRMS (CI): 339.1808 calc, 339.1810 found. The procedure was adapted from Basel and Hassner.[10]

For the photoresist print tests, the dual-tone photoresist formulation consisted of a commercial novolak polymer with DNQ PAC, a triphenylsulfonium perfluorobutanesulfonate PAG, and 1,4-benzenedimethanol cross-linker. The resist was applied by spin-coating, followed by a 60-second, 110 °C soft bake.

Silicon wafers were used for initial testing of the photoresists, and stainless steel foils were used for final testing of the photoresist on a flexible substrate. The substrates were treated with a commercial adhesion promoter (AP410, Silicon Resources Inc.) to ensure good adhesion between the photoresist and the substrate surface. The photoresists

were then spin-coated and baked at 110 °C for 60 seconds to produce 1 μm films, verified via stylus profilometry.

The exposure and bake conditions were optimized to allow positive-tone image to develop in less than 60 seconds in the AZ 300 MIF developer (aqueous tetramethylammonium hydroxide solution), while maintaining the negative-tone film loss at less than 5%. Test exposures were done with a medium pressure mercury arc lamp UV curing system (Novacure, EXFO, 250–450 nm wavelength, ~8 mW/cm^2 at the wafer plane), and a 345 nm long pass filter was applied on the wafer side during positive-tone exposure. No filter was applied for the negative-tone exposure. Subsequent to development of the positive-tone image, a broadband flood exposure was applied to the entire sample without additional bake to activate the unexposed portion of the photoresist, rendering the unexposed region soluble for later development. Etch conditions (including etch pressure, reactant flow rates, and etch power) were optimized to improve etch rates of silicon dioxide and selectivity with respect to loss of resist. All reactive ion etching was performed using an Oracle III (Trion Technology) etcher. Transfer etches into silicon dioxide were done using 15 sccm CF_4, 5 sccm He, 50 mTorr pressure, and 150 W power. The oxygen crust removal etch process used 20 sccm O_2, 50 mTorr pressure, and 150 W power for 30 s.

4.5 CONCLUSION

The dual-tone photoresist is capable of storing and transferring multiple latent images by combining a positive tone, i-line, novolak-based resist with a photoacid generator and an acid-catalyzed, thermally activated crosslinker. The photoactive compounds that initiate positive and negative tone responses were independently chosen to allow spectral differentiation of positive and negative exposed regions. The dual-tone

photoresist has been successfully applied in a self-aligned patterning process, demonstrating the simultaneous imaging of two device layers and the subsequent transfer of those images into the substrate. The successful integration of the dual-tone photoresist addresses the challenge of layer to layer alignment during the patterning of flexible substrate materials and suggests the possibility for application to higher resolution lithography.

4.6 REFERENCES

1. Cheng, I. C.; Kattamis, A.; Long, K.; Sturm, J. C.; Wagner, S., Stress control for overlay registration in a Si: H TFTs on flexible organic polymer foil substrates. *Journal of the Society for Information Display* **2005,** 13, 563.
2. Jain, K.; Klosner, M.; Zemel, M.; Raghunandan, S., Flexible Electronics and Displays: High-Resolution, Roll-to-Roll, Projection Lithography and Photoablation Processing Technologies for High-Throughput Production. *Proceedings of the IEEE* **2005,** 93, (8), 1500-1510.
3. Gleskova, H.; Cheng, I. C.; Wagner, S.; Sturm, J. C.; Suo, Z., Mechanics of thin-film transistors and solar cells on flexible substrates. *Solar Energy* **2006,** 80, (6), 687-693.
4. Hinsberg, W. D.; Pederson, L. A.; Willson, C. G. In *Zero-misalignment Lithographic Process Using a Photoresist with Wavelength-selected tone*, Advances in resist technology and processing V, Santa Clara, California, 29 February-2 March, 1988; MacDonald, S. A., Ed. SPIE: Santa Clara, California, 1988; pp 2-12.
5. Hinsberg, W. D.; MacDonald, S. A.; Pederson, L. A.; Willson, C. G., A lithographic analog of color photography: self-aligning photolithography using a resist with wavelength-dependent tone. *Journal of Imaging Science* **1989,** 33, (4), 129-35.
6. Iwayanagi, T.; Kohashi, T.; Nonogaki, S.; Matsuzawa, T.; Douta, K.; Yanazawa, H., Azide-phenolic resin photoresists for deep UV lithography. *Electron Devices, IEEE Transactions on* **1981,** 28, (11), 1306-1310.
7. Yamamoto, J.; Uchino, S.; Hattori, T.; Yoshimura, T.; Murai, F., Nanometer electron beam lithography with azide-phenolic resin resist systems. *Japanese journal of applied physics* **1996,** 35, (part 1), 6511-6516.

8. Frechet, J. M. J.; Matuszczak, S.; Reck, B.; Stover, H. D. H.; Willson, C. G., Chemically amplified imaging materials based on electrophilic aromatic substitution: poly [4-(acetoxymethyl) styrene-co-4-hydroxystyrene]. *Macromolecules* **1991,** 24, (8), 1746-1754.

9. Chambers, C. R.; Kusumoto, S.; Lee, G. S.; Vasudev, A.; Walthal, L.; Osborn, B. P.; Zimmerman, P.; Conley, W.; Willson, C. G. In *Dissolution inhibitors for 157-nm photolithography*, Advances in Resist Technology and Processing XX, Santa Clara, CA, 24 February 2003, 2003; SPIE: Santa Clara, CA, 2003; p 93.

10. Basel, Y.; Hassner, A., Di-tert-butyl Dicarbonate and 4-(Dimethylamino)pyridine Revisited. Their Reactions with Amines and Alcohols1. *The Journal of Organic Chemistry* **2000,** 65, (20), 6368-6380.

Chapter 5: Optimization of photoresist for materials-based pitch division

5.1 INTRODUCTION

As discussed in Chapter 1, with the delayed introduction of extreme ultraviolet lithography (EUV), there has been increased demand for resolution enhancement techniques for 193 nm lithography. One such class of techniques is double patterning, which, in conjunction with immersion lithography, aims to extend 193 nm photolithography to the 22 nm and 16 nm technology nodes. Litho-etch-litho-etch (LELE), litho-freeze-litho-etch (LFLE)[1] and self-aligned double patterning[2] techniques are being developed to extend 193 nm lithography. However, these all rely on multiple exposure or etch processing steps, which are detrimental to production costs and throughput. In contrast, the materials-based solutions for pitch division described below possess two dose threshold responses in a single resist, allowing for the generation of two latent images without additional etch or aligned exposure steps.

5.2 DESCRIPTION OF MATERIALS-BASED PITCH DIVISION RESIST

Typical positive-tone, chemically amplified resists used in 193 nm lithography are based on a UV-transparent polyacrylate combined with a photoacid generator (PAG) designed to produce acid when exposed to actinic light, which in turn catalyzes the deprotection of the polymer during a post-exposure bake (PEB). Subsequent development in aqueous base developer removes the soluble resist in the exposed regions.

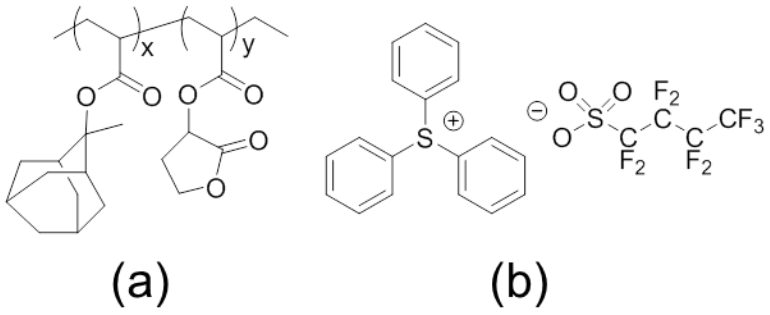

Figure 5.1: Components of 193 nm chemically amplified photoresist: a) generic acid-labile UV-transparent acrylate, methacrylate methyl adamantyl methacrylate-co-γ-butyrolactone methacrylate (MADMA-co-GBLMA); and b) a photoacid generator, triphenylsulfonium (TPS) nonaflate.

As the exposure dose increases, it eventually passes through a threshold at which the resist becomes completely soluble. The solubility threshold occurs (for a given set of PEB conditions and developer) at the dose-to-clear, known as E_0. When this solubility threshold behavior is applied to a sinusoidal (line/space) exposure aerial image, lines and spaces are formed, wherein the spatial frequency of the lines are equal to that of the exposure pattern, as illustrated in Figure 5.2.

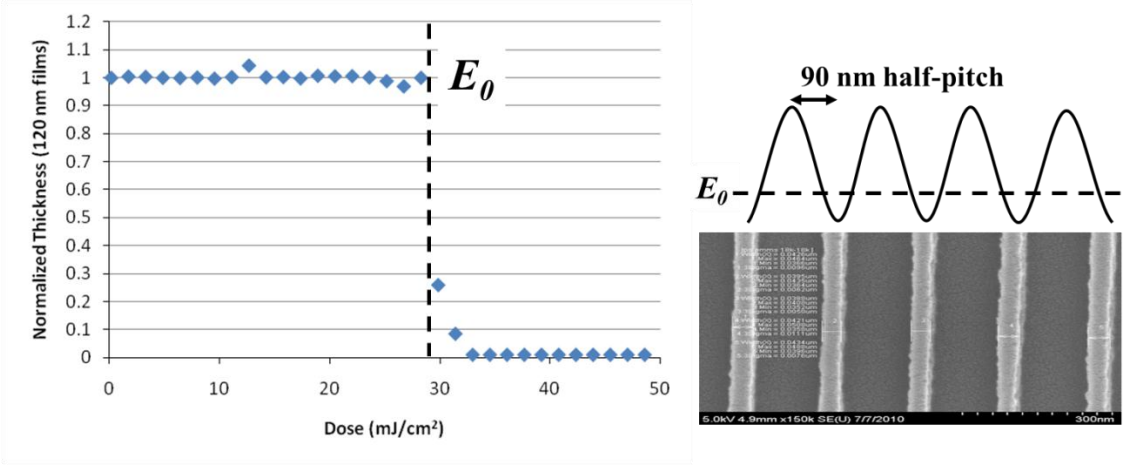

Figure 5.2: Dose response of a typical chemically amplified resist. Left: the remaining film thickness after development as a function of dose. The dose to clear, E_0, is the dose at which the film becomes soluble in aqueous base. Right: A single-threshold resist exposed a sinusoidal aerial image produces a line/space pattern with the same spatial frequency as the image.

The materials-based dual-tone photoresist developed and reported by Gu *et al.*[3] combines the positive-tone response, including the dose-to-clear, with a negative-tone response, resulting in a second solubility threshold in the contrast curve. The negative-tone dose threshold, called the dose-to-negative, E_n, is always higher than the dose-to-clear for development in positive-tone developers. Accordingly, for exposure doses below E_0, the resist is insoluble, for doses between E_0 and E_n, the resist is soluble, and for doses above E_n, the resist is again insoluble. The solubility threshold is illustrated in Figure 5.3. Also shown is the effect on the printed features for a line/space aerial image: the spatial frequency of the features is double that of the aerial image. In other words, for every peak in aerial image intensity, there are two sets of lines and spaces.

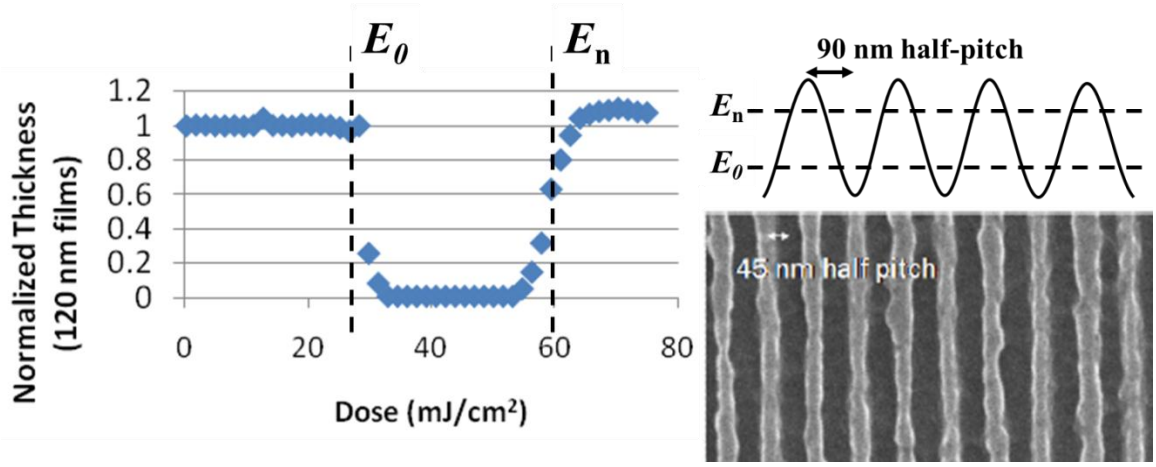

Figure 5.3: Dose response of a dual-threshold photoresist for materials-based pitch division. Left: the remaining film thickness after development as a function of dose, showing the dose-to-clear, E_0, and the dose-to-negative, E_n. Right: the dual-threshold behavior, when applied to a sinusoidal aerial image, results in a line/space pattern with a spatial frequency of twice that of the aerial image, i.e., a 45 nm half-pitch line/space pattern from a 90 nm half-pitch image.

The dual-threshold response in the contrast curve depicted in Figure 5.3 results from the addition of a single additional component into the positive-tone photoresist: a photobase generator (PBG). Upon absorption of 193 nm UV light, the PBG produces a base that neutralizes a portion of the acid produced by the PAG. Importantly, the neutralization reaction of the acid and the base is much faster than the reaction of the polymer with either the acid or the base, so the dual-threshold response is due to the amount of *net acid* in the film (after neutralization) as a function of dose. The net amount of acid in the photoresist depends on the amount of PAG and PBG in the resist, and the rate of acid and base production as a function of exposure dose. For the hypothetical case where the PAG/PBG molar ratio is unity and the rates of PAG and PBG decomposition to acid and base are equal, the acid produced by the PAG will always be neutralized by the

base produced by the PBG, so the net acid will always be zero and no reaction take place in the resist.

In order to produce a dual-threshold response, the PAG/PBG combination must produce acid and base at different rates. More specifically, in order to achieve the dose-to-clear response, there must be an excess of acid so the rate of acid production as a function of dose is initially faster than the rate of base production. In order to achieve the second (dose-to-negative) threshold, the rate of production of the base must overtake the rate of production of the acid, such that at high doses, the net amount of acid decreases. This occurs when the production of acid by the PAG becomes saturated as it is depleted, while the PBG continues to produce base.

Assuming first-order kinetics for both the PAG and PBG decomposition into acid or base, the concentration of the net acid generated in the resist is as follows:

$$[Net\ Acid] = [PAG]_0[(1-p) - e^{-k_{\mathrm{PAG}}D} + pe^{-k_{\mathrm{PBG}}D}] \qquad 5.1$$

In this equation, $[PAG]_0$ is the initial (zero dose) molar concentration of PAG, p is the ratio of initial molar concentration of PBG to that of the PAG, k_{PAG} and k_{PBG} are the rate constants for the acid and base production, respectively, and D is the exposure dose in the photoresist. Figure 5.4 shows acid, base, and net acid concentrations produced by Equation 5.5 for the case where the molar loading of the PBG is four times that of the PAG, and k_{PAG} and k_{PBG} are 0.077 cm^2/mJ and 0.00385 cm^2/mJ, respectively.

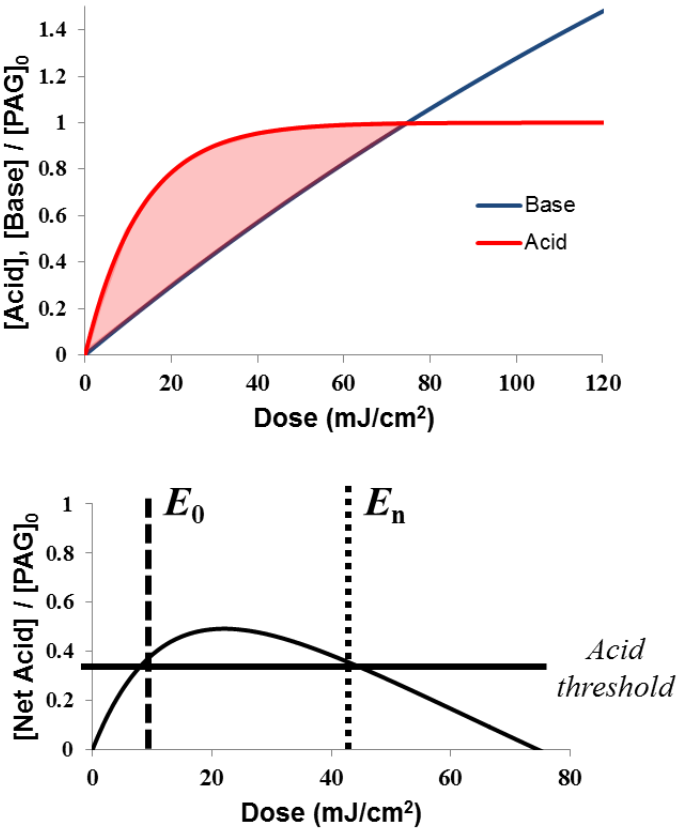

Figure 5.4: Plot of acid and base concentrations vs. dose (top) and plot of net acid concentration vs. dose (bottom) for $p = 4$, $k_{PAG} = 0.077$ cm^2/mJ, and $k_{PBG} = 0.00385$ cm^2/mJ (see Equation 5.5). All acid and base concentrations are normalized with respect to the initial PAG concentration.

A variety of photobase generators have been synthesized and studied[4-7], of which *o*-nitrobenzyl carbamates were initially chosen for photoresist formulation by Gu *et al*.[8] One of these, *o*-nitrobenzyl N,N-dicyclohexylcarbamate (DCHA-CARB) is shown in Figure 5.5. The kinetics of the dissolution of PAGs and *o*-nitrobenzyl carbamate PBGs were studied previously.[3] PAG dissociation was monitored in the resist by measuring the dose-to-clear as a function of the concentration of base quencher added to the formulation to titrate the generated acid. Measurement of PBG kinetic constants are more difficult, but the generation of base by PBG can be quantified by real-time FTIR monitoring of the

PBG dissociation via disappearance of the nitro group absorbance of the PBG by FTIR.[3] Addition of DCHA-CARB into a commercial 193 nm, chemically amplified, positive tone photoresist resulted in pitch division, as shown by the micrograph in Figure 5.3.[8]

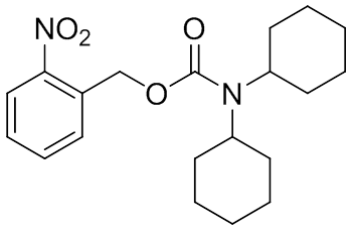

Figure 5.5: *o*-nitrobenzyl N,N-dicyclohexylcarbamate (DCHA-CARB)

5.3 IMPROVING LINE EDGE ROUGHNESS AND RESOLUTION

5.3.1 Formulation and process optimization

Although the addition of DCHA-CARB to commercial 193 nm resists results in a resist capable of pitch division, the pitch division of a 90 nm half-pitch line/space image to 45 nm half-pitch lines and spaces falls short of the resolution requirements for the current 22 nm and future 16 nm (linewidth) technology nodes. In addition, the line edge roughness (LER) of the patterned features is larger than the current standard. While line edge roughness is a function of the image log slope of the aerial image, in the limit of high image log slope, the resist materials contribute a fundamental limitation to the LER.[9] Other contributors to LER are photon shot noise and acid diffusion at the line edge, but these effects are less understood at feature sizes below 50 nm.[10] One effort to reduce LER in pitch-division resists focuses on reducing the diffusion of acid and base by binding the PAG and PBG to the polymer backbone, which results in improved process windows for pitch division.[11]

Aside from evaluating new PBGs as additives in commercial resist and developing polymer-bound PAGs and PBGs, optimization of formulations comprising

off-the-shelf chemicals has the potential to achieve improvements in pitch division results while being more likely to uncover the causes of LER and resolution problemsThe model system explored here consists of a MADMA-co-GBLMA polymer with a molar repeat unit ratio of 58:42 MADMA:GBLMA (Dupont), TPS nonaflate PAG (TPS-nf), DCHA-CARB, and a base quencher, trioctylamine (TOA). As a starting point, a formulation was chosen consisting of 5 wt% MADMA-co-GBLMA resin in 2-heptanone, with the addition of TPS-nf in a weight ratio of 7:100 TPS-nf to resin solids as well as TOA in the molar ratio of 0.375:1 TOA:PAG. The addition of TOA moves the dose-to-clear for the positive tone resist into a convenient range for exposure. Finally, DCHA-CARB is added in a 1:1 molar ratio to the PAG. The contrast curve for the resist formulation is shown in Figure 5.6: the dose-to-clear is 11 mJ/cm^2 and the dose-to-negative is 42 mJ/cm^2.

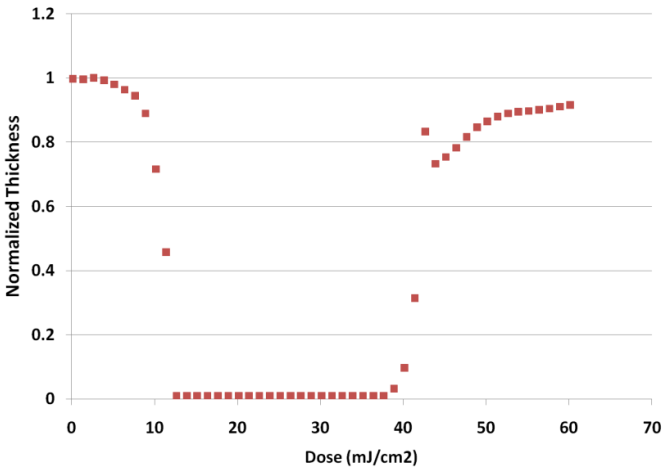

Figure 5.6: Contrast curve for the model resist including a molar ratio of TPS-nf:TOA:DCHA-CARB of 1:0.375:1. E_0 = 11 mJ/cm^2 and E_n = 42 mJ/cm^2. The PEB temperature is 110 °C.

To achieve pitch division with a line/space aerial image, the dose thresholds, E_0 and E_n, must be within the window defined by the minimum and maximum dose received by the resist, as illustrated in Figure 5.3. Simulations using PROLITH software (KLA

Tencor) indicate that, as the difference between the minimum and maximum dose (as measured by the image contrast $(I_{max} - I_{min})/(I_{max} + I_{min})$) grows, the optimal difference between E_0 and E_n also grows linearly.[3] The difference between E_0 and E_n is captured in an expression analogous to the image contrast, called the "E-factor":

$$\text{E Factor} = \frac{E_n - E_0}{E_n + E_0} \qquad 5.2$$

Because the contrast of the Amphibian imaging tool does not vary, the optimal E-factor for pitch division is relatively constant. An E-factor of 0.5 was targeted, since the Amphibian imaging tool is not subject to speckle or flare as with traditional photolithography exposure tools.

The E-factor can be tuned by modifying the dose-to-clear and the dose-to-negative. The dual-threshold response is due to the parabolic shape of the net acid vs. dose curve. When the net acid in the film reaches or exceeds a threshold concentration, the film becomes soluble. As the net acid concentration decreases, it again crosses the threshold acid concentration, and the resist becomes insoluble. Hence, the dose-to-clear, E_0, and the dose-to-negative, E_n, are both mainly determined by two factors: the net acid curve and the threshold acid concentration (Figure 5.4).

The acid threshold is the amount of acid that is necessary to catalyze sufficient reaction in the photoresist to effect a solubility change. The acid threshold is predicted to decrease with increasing PEB temperature due to increased acid diffusion and reaction rates during PEB. Although it is difficult to define and measure the acid threshold, for most resist formulations, the E-factor can be tuned by changing the PEB temperature: as PEB temperature increases, the E-factor increases, as shown in Figure 5.7a.

In addition to tuning the acid threshold, the concentration of the net acid in the resist can be tuned. The net acid is obviously modified by changing the PAG and PBG

loadings as well as the kinetic constants, as discussed above. The net acid curve can be uniformly shifted downward by adding a base quencher, such as trioctylamine (TOA), to the formulation. The effect of base quencher is shown by the contrast curves in Figure 5.7b.

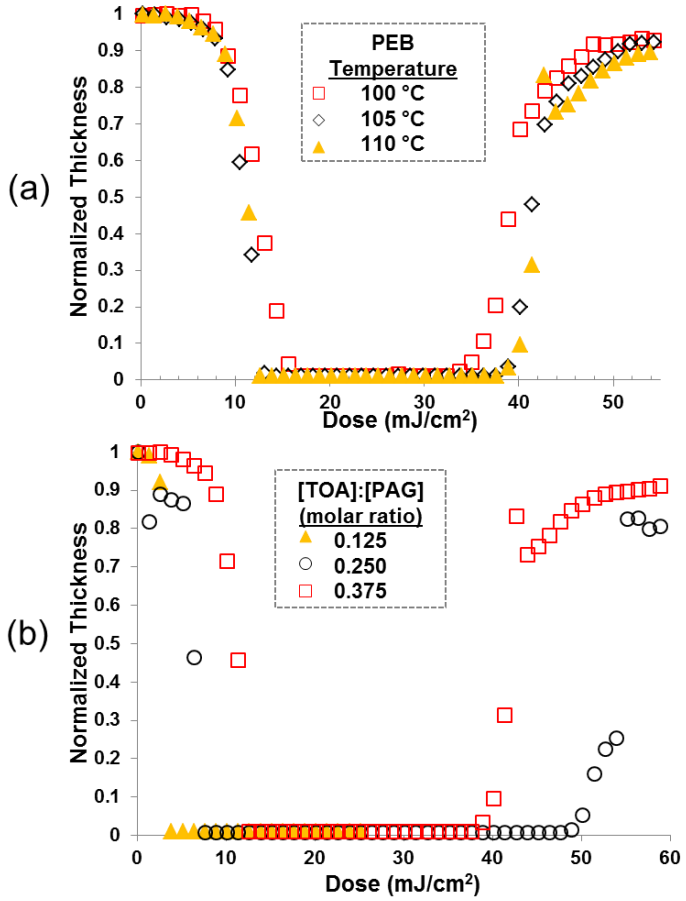

Figure 5.7: Contrast curves for the resist described above with variations in (a) PEB temperature and (b) TOA:PAG molar ratio (all at 110 °C PEB)

5.3.2 Imaging

Imaging of line/space patterns in pitch division resists was accomplished by a 193 nm interference lithography system (see section 5.5) with either 240 nm half pitch (at low NA) or 90 nm half pitch (at high NA) patterns. The most easily controlled process

variable is the average exposure dose over the patterned area (1-2 mm^2). Since the patterned area is produced by the interference of two laser beams with Gaussian intensity distributions, the exposure varies within the patterned area. Accordingly,the exposure is highest in the middle and tails off at the edge of the exposed region. The variation in exposure results in three regions: the outer regions are underexposed, so the maximum dose is not high enough to cross the E_n threshold; the center regions are overexposed, so the minimum dose is higher than E_0; and the intermediate region is where pitch division is observed, if possible.

The size of the exposure dose process window for pitch division is roughly represented by the area in which pitch division occurs. The advantage of the variable exposure dose over the exposed field is that it allows for a quick visual survey of the pitch division process window. However, it is extremely difficult to quantify the exposure dose at a particular point in the exposed field, so a quantitative process window cannot be obtained.

Figure 5.8 shows a low magnification image of an exposed field for the photoresist formulation, described above, along with high-magnification images obtained in the positive- and negative-tone regions. The critical dimension (CD) and LER are measured from the images collected from each region. Starting at the outside of the field, the positive-tone lines start to appear as large lines between small spaces. The line CD decreases approaching the pitch division region. In the case of many formulations, including the one imaged in Figure 5.8, the pitch division region exhibits no pitch division. Loss of adhesion and large variations in line width result in the positive tone lines disappearing before the smallest negative-tone lines appear at more exposed regions; so the pitch division region appears cleared.

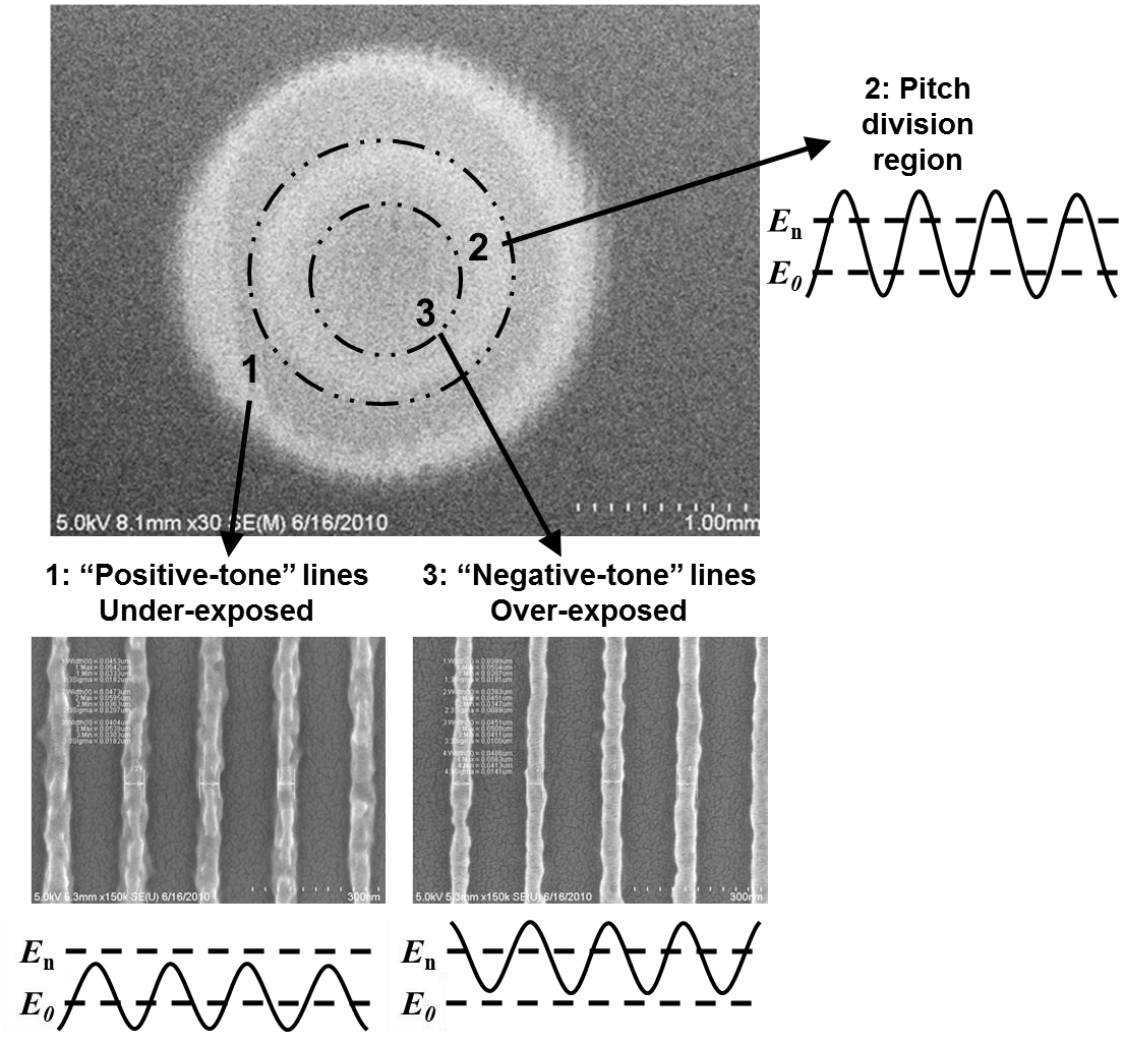

Figure 5.8: Low-magnification scanning electron micrograph (top) of exposed field of the resist described above, with annotations indicating the positive-tone, negative-tone, and pitch division regions. High-magnification images show positive-tone and negative-tone lines (45 nm, ~15 nm LER)

The cleared pitch division region suggested that the E-factor (i.e. the spread between E_n and E_0) was too large, causing the minimum and maximum doses to lie between E_n and E_0. Decreasing the E-factor by lowering the PEB temperature from 110 °C to 100 °C resulted in discernible pitch division, although the pitch division region was

found to be small and there was considerable bridging between lines and spaces. The PEB temperature was adjusted to 105 °C PEB to address bridging, and this resulted in distinct but rough pitch division, as shown in Figure 5.9. The formulation is 5 wt% MADMA-co-GBLMA, with a 7 wt% TPS-nf to resin ratio and [TPS-nf]:[DCHA-CARB]:[TOA] = 1:0.375:1 (molar).

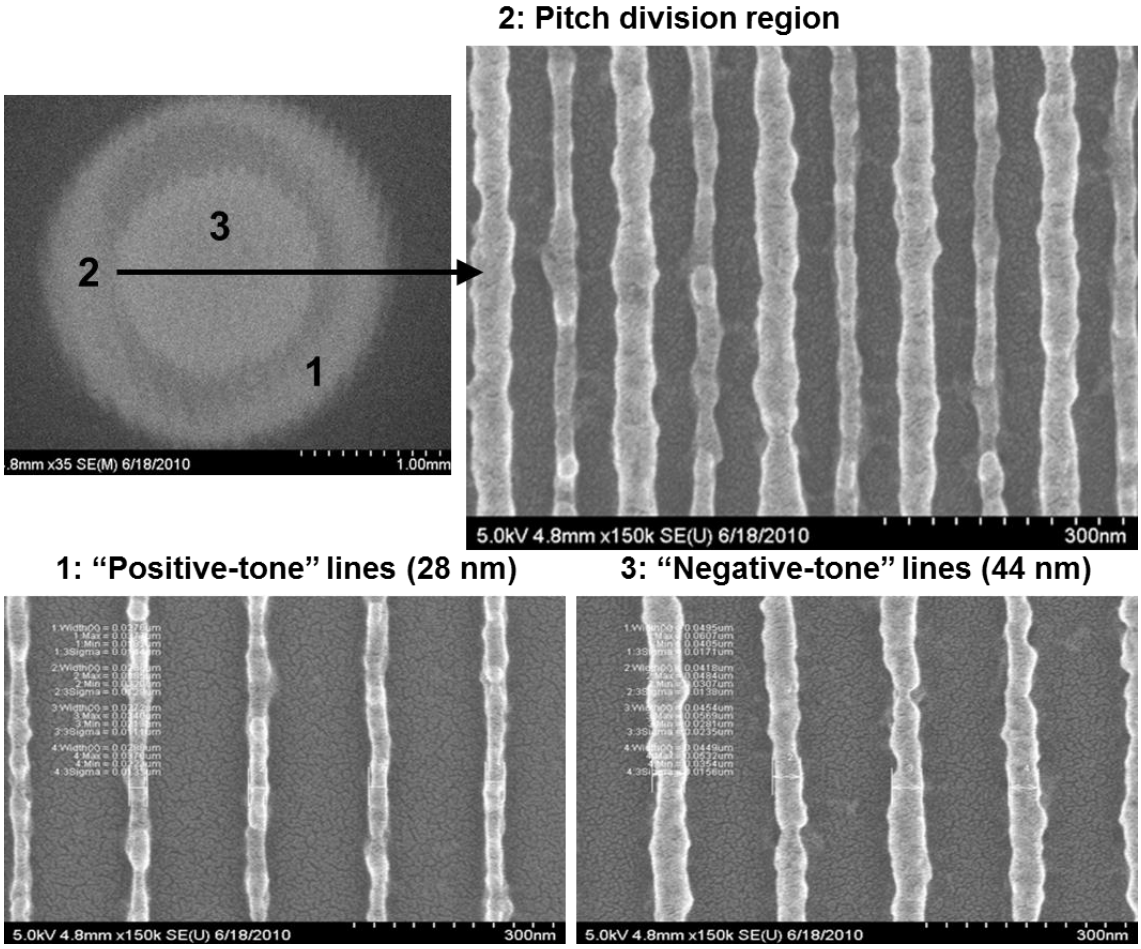

Figure 5.9: Pitch division in a photoresist formulated from off-the-shelf chemicals and polymers along with positive- and negative-tone lines.

The demonstration of pitch division is the first in a resist formulated from off-the-shelf chemicals and invites further inquiry into the causes of the high LER and resolution

limitations of pitch division resists. The role of the base quencher, in this case TOA, is particularly interesting for pitch division resists. Addition of base into chemically amplified photoresists increases the dose-to-clear, but, perhaps more importantly, it has been shown to have an effect on the shape of the reaction-diffusion front of the photogenerated acid, improving the acid gradient at the line edge.[12] However, as shown in Figure 5.7, addition of base quencher decreases the E-factor. The decrease in E-factor can be offset by increasing the PEB temperature; however, increasing PEB temperature increases the diffusion of the acid and the base, potentially leading to a broader deprotection front.

The acid gradient at the line edge greatly affects line edge roughness. The tradeoff between the line-sharpening effects of the base quencher and the increased acid diffusion of the higher PEB could be mitigated by replacing base quencher with additional PBG to reduce required bake temperature. Increasing the amount of base quencher also increases the acid gradient at the line edge formed by the E_n threshold, although any such increase comes at the expense of the acid gradient at the E_0 threshold line edge. To explore the effect of substituting PBG with base quencher, a series of formulations were made as shown in Table 5.1. For all formulations, the PEB was adjusted to maintain the E-factor as determined from contrast curves at or near 0.5. PEB temperatures ranged from 90 to 110 °C. The wider-than-expected range indicates that the decrease in base quencher was not sufficiently offset by increases in the PBG amount.

An analysis of the resist line/space images, produced for the indicated formulations and processing parameters using a 90 nm half pitch aerial image, indicate that conditions for pitch division are best achieved at intermediate PBG loadings. For the [PBG]:[PAG] molar ratio of 2:1, pitch division was observed, but the overlap region was extremely small (only a few tens of lines) and bridging of lines was widespread. For a

[PBG]:[PAG] ratio of 3:1, no pitch division was observed, but the minimum positive-tone linewidth obtainable was 28 nm with a 11 nm linewidth roughness (LWR) as measured by three times the standard deviation of linewidth. Similarly, the smallest negative tone lines were 55 nm with 13 nm LWR. The CD was significant, and probably contributed to the failure of the pitch division.

Table 5.1: Several PBG and base quencher combinations for the exploration of base substitution. PEB temperature was adjusted to bring the E-factor as close to 0.5 as possible. PEB temperature is encoded as follows: yellow: 90°C, orange: 100°C, red: 110°C.

		[TOA]:[PAG] Molar Ratio														
		0			0.125			0.25			0.375			0.5		
		E_n	E_0	E-factor	E_n	E_0	E-factor	E_n	E_0	E-factor	E_n	E_0	E-factor	E_n	E_0	E-factor
[PBG] / [PAG] Molar Ratio	1										68	12	0.7	48	17	0.48
	2							26	9	0.49						
	3				22	7	0.52									
	4	11	4	0.47												

5.3.3 Negative tone development

Development of dual tone resists by organic developers was also investigated, as it was believed that the dissolution sensitivity might be better for negative tone development. A commercial 193 nm resist with added DCHA-CARB was imaged with both 90 nm and 240 nm half-pitch aerial images, followed by a PEB at 107 °C and development with either an aqueous base developer or anisole, an organic solvent. No

pitch division was observed for the 90 nm half pitch aerial images, while the 240 nm half pitch aerial image produces pitch division to 120 nm. The top-down images (Figure 5.10) show that complementary images are formed by the two developers. Cross-section SEM images reveal distinct defects in resist lines. Anisole-developed lines exhibit footing, but only in the direction of maximum dose. Conversely, aqueous base-developed lines exhibit undercutting, but again, only in the direction of maximum dose. One explanation for this behavior is absorption in the photoresist. Simulations of effects of absorption in dual-tone resist predict undercutting of lines formed by the E_n threshold.[13]

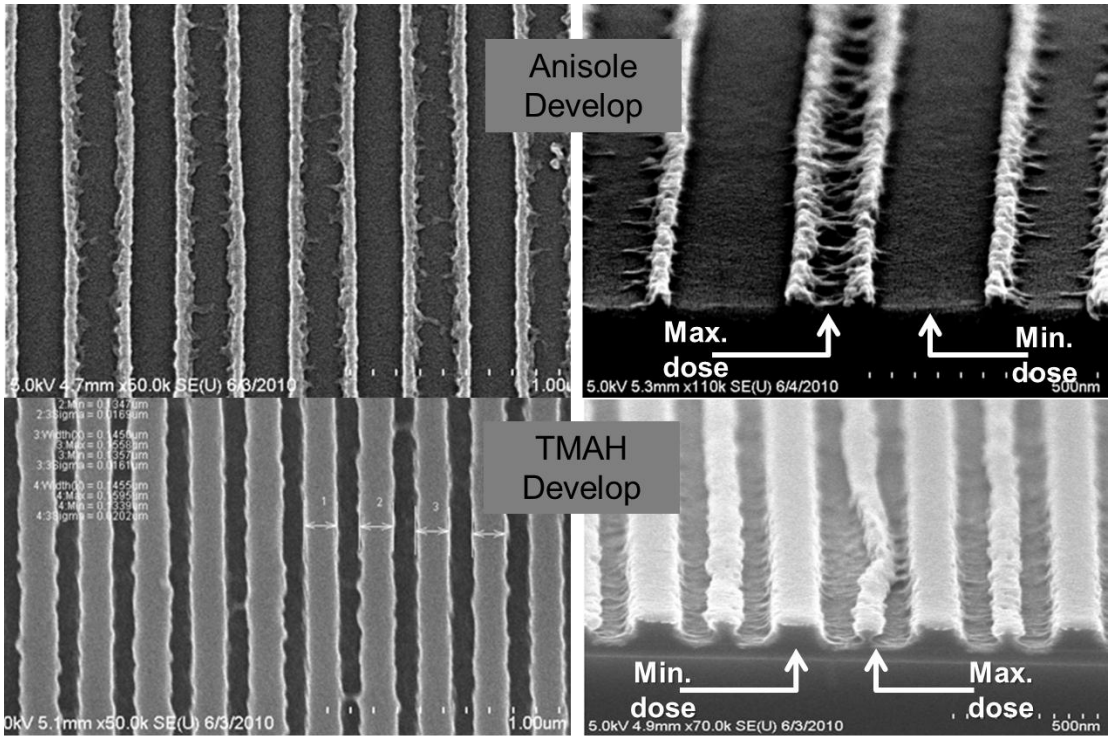

Figure 5.10: Top-down (left) and cross-section (right) images of the resist profile of a pitch division photoresist developed with anisole (top) and TMAH solution (right).

5.4 PAG AND PBG KINETICS

5.4.1 Kinetics for one-stage and two-stage PBGs

Materials-based pitch division produces twice the number of features because it has twice the number of dissolution thresholds, since the net acid vs. dose curve is parabolic. However, when the dissociation of PAG and PBG follow first order kinetics, the acid gradient at each line edge is significantly less than it is for a regular chemically amplified photoresist. This can be verified by writing an expression for the derivative of net acid versus dose with respect to dose in the limit of zero dose:

$$\left.\frac{d[Net\ Acid]}{dD}\right|_{D=0} = [PAG]_0(k_{PAG} - pk_{PBG}) \qquad 5.3$$

When E_0 occurs at doses which are low relative to k_{PAG}^{-1}, Equation 5.3 describes the acid gradient at the line edge formed by the E_0 threshold. At the E_n line edge, the gradient is negative and is approximated by the following expression:

$$\left.\frac{d[Net\ Acid]}{dD}\right|_{E_n} \sim -[PAG]_0 pk_{PBG} \qquad 5.4$$

Equations 5.3 and 5.4, taken together, demonstrate that increasing the PBG loading increases the gradient at the E_n line edge, but *decreases* the acid gradient at the E_0 line edge. This decrease in acid gradient with respect to dose is compounded by the fact that the image log slope (ILS) at the line edge is significantly lower since the line edge is no longer located at the point of steepest intensity gradient.

The exact slope at the E_0 and E_n thresholds will depend on E_0 and E_n, but it can be estimated by stipulating, for the purpose of calculation, that E_0 and E_n are equidistant from the critical dose E_{crit}, which is the dose at which the net acid reaches a maximum. This allows specification of E_0 and E_n for a given value of the E-factor. Using Equation 5.1 for an E-factor of 0.5 allows computation of the acid gradients as a function of PBG

loading, normalized by the slope for the case where PBG loading is zero (i.e. a normal chemically amplified resist). Table 5.2 gives the values for the case where k_{PAG} and k_{PBG} are 0.054 cm^2/mJ and 0.007 cm^2/mJ, respectively. The table values predict a maximum in the normalized acid gradient for a [PBG]:[PAG] ratio near 3.0, which is consistent with the observations from the base substitution study (above).

Table 5.2: Normalized acid slope computed from Equation 5.1 (relative to a normal chemically amplified resist) for a PBG resist and an E-factor of 0.5 where k_{PAG} and k_{PBG} are 0.054 cm^2/mJ and 0.007 cm^2/mJ, respectively.

$\frac{[PBG]_0}{[PAG]_0}$	$\frac{d[Net\ Acid]}{dD}\Big\|_{E_0} / (k_{PAG}[PAG]_0)$	$\frac{-d[Net\ Acid]}{dD}\Big\|_{E_n} / (k_{PAG}[PAG]_0)$	Average Gradient
6	0.10	0.08	0.09
4	0.19	0.12	0.16
3	0.22	0.12	0.17
2	0.23	0.09	0.16
1.5	0.22	0.08	0.15
1	0.20	0.05	0.13
No PBG	1.0 (at 0 dose limit)	--	--

Table 5.2 predicts that acid gradients at the line edge for pitch division resists are a fraction of the maximum obtainable value for a normal chemically amplified resist. The degraded acid gradients are a consequence of first order kinetics for acid and base generation. However, if the production of base can be delayed at low doses, the net acid would rise faster as a function of dose. Similarly, acceleration of production of base at higher doses would improve the acid gradient at high doses. While there is no known example of this type of photobase generator in the literature, similar kinetics can be realized with a two-stage series reaction:

$$L-PBG \xrightarrow{hv,k_{PBG1}} PBG \xrightarrow{hv,k_{PBG2}} Base$$

In this reaction a latent PBG (L-PBG) reacts with a photon to form a PBG, which reacts with a second photon to produce a base. Figure 5.11 shows a cartoon of possible acid and base concentration vs. dose for single-stage and two-stage PBGs. Two-stage PBGs would enable the net acid vs. dose curve to have greater slopes.

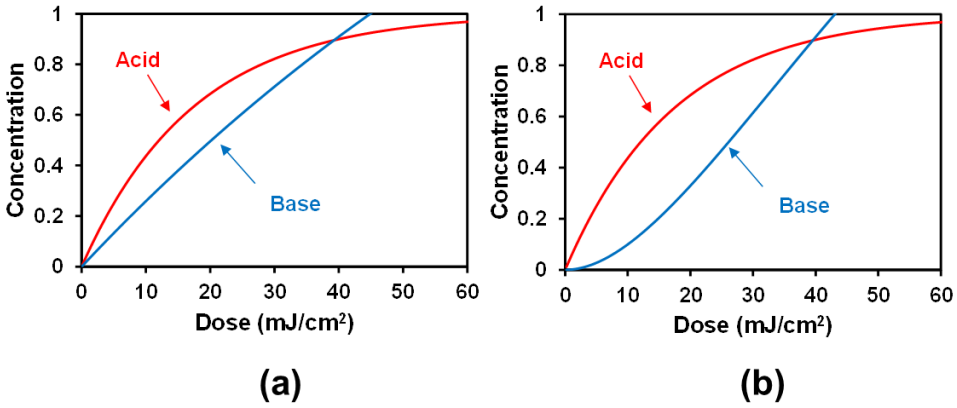

Figure 5.11: Concentration of acid and base as a function of dose for (a) a single-stage PBG following first order kinetics and (b) a two-stage PBG.

Assuming that each step in the production of base from a two-stage PBG follows first-order kinetics, we can write the following equation for the net acid:

$$\frac{d[Net\ Acid]}{dD} = [PAG]_0\left(k_{PAG}e^{-k_{PAG}D} - \frac{k_{PBG1}k_{PBG2}p}{k_{PBG2}-k_{PBG1}}\left(e^{-k_{PBG1}D} - e^{-k_{PBG2}D}\right)\right) \quad 5.5$$

Following the same assumptions and method used to produce Table 5.2, we find the normalized gradients as a function of PBG loading relative to the PAG for the case where k_{PAG}, k_{PBG1}, and k_{PBG1} are 0.054 cm^2/mJ, 0.007 cm^2/mJ, and 0.007 cm^2/mJ, respectively.

Table 5.3: Normalized acid slope computed from Equation 5.5 (relative to a normal chemically amplified resist) for a two-stage PBG and an E-factor of 0.5 where k_{PAG} and k_{PBG1}, and k_{PBG2} are 0.054 cm^2/mJ, 0.007 cm^2/mJ, and 0.007 cm^2/mJ, respectively.

$\frac{[PBG]_0}{[PAG]_0}$	$\frac{d[Net\ Acid]}{dD}\Big\|_{E_0} / (k_{PAG}[PAG]_0)$	$\frac{-d[Net\ Acid]}{dD}\Big\|_{E_n} / (k_{PAG}[PAG]_0)$	Average Gradient
16	0.38	0.24	0.31
8	0.33	0.17	0.25
4	0.27	0.11	0.19
2	0.22	0.06	0.14
1.5	0.20	0.05	0.12
1	0.17	0.04	0.10
No PBG	1.0 (at 0 dose limit)	--	--

The relative rate of the two steps in the production of photogenerated base is an important parameter because, if one of the steps is much faster than the other, the resist behaves as if the PAG were single-stage. Table 5.3 also shows that PBG loading for a two-stage PBG can be increased without negatively affecting acid gradients. Indeed, the main benefit of two-stage PBGs with respect to acid gradients comes at high PBG loading. However, at very high PBG loading, adverse effects from absorption of the 193 nm light by the PBG as well as dissolution inhibition/promotion effects will likely override any gains from increased acid gradient at the line edge.

5.4.2 NMR characterization of PAG and PBG kinetics

One benefit of the availability of a functioning pitch division photoresist formulated from off-the-shelf chemicals is the ability to more fully characterize the kinetics of the photochemistry that takes place in the resist. Using a Microprobe sample probe (Bruker Biospin), it is possible to quantitatively monitor the products and reactants for decomposition reactions of PAGs and PBGs as a function of dose. For example, the

photoresist imaged in Figure 5.9, which is characterized by the contrast curve in Figure 5.6, was monitored via NMR by exposing 11 full wafers coated with photoresist to a range of exposure doses from 0 to 60 mJ/cm^2. The photoresist formulation consists of 5 wt% MADMA-co-GBLMA resin in 2-heptanone with the addition of TPS-nf in a weight ratio of 7:100 TPS-nf to resin solids as well as TOA in the molar ratio of 0.375:1 TOA:PAG. While monitoring the appearance of acid and base is difficult, the rate of acid and base production can be inferred indirectly from the rate of disappearance of the PAG and PBG. Table 5.4 lists some relevant peaks found in the NMR spectra, and Figure 5.12 shows a portion of the NMR spectra for a series of exposed wafers.

Table 5.4: Selected NMR peaks relevant to the characterization of PAG and PBG kinetics.

δ (ppm) / multiplicity	Assignment	# of Eq. ^{1}Hs	Notes
3.0 (m)	TOA-H$^+$ [−N(−C**H$_2$**−)$_3$]	6	Product of quencher neutralization
4.3 (d)	Polymer backbone aliphatic H	--	Used as normalization peak
7.7 (m)	TPS Nanoflate [$^+$S(−Ar−**H**$_5$)$_3$]	15	PAG
8.1 (d)	DCHA-CARB [Ar−**H**]	1	PBG

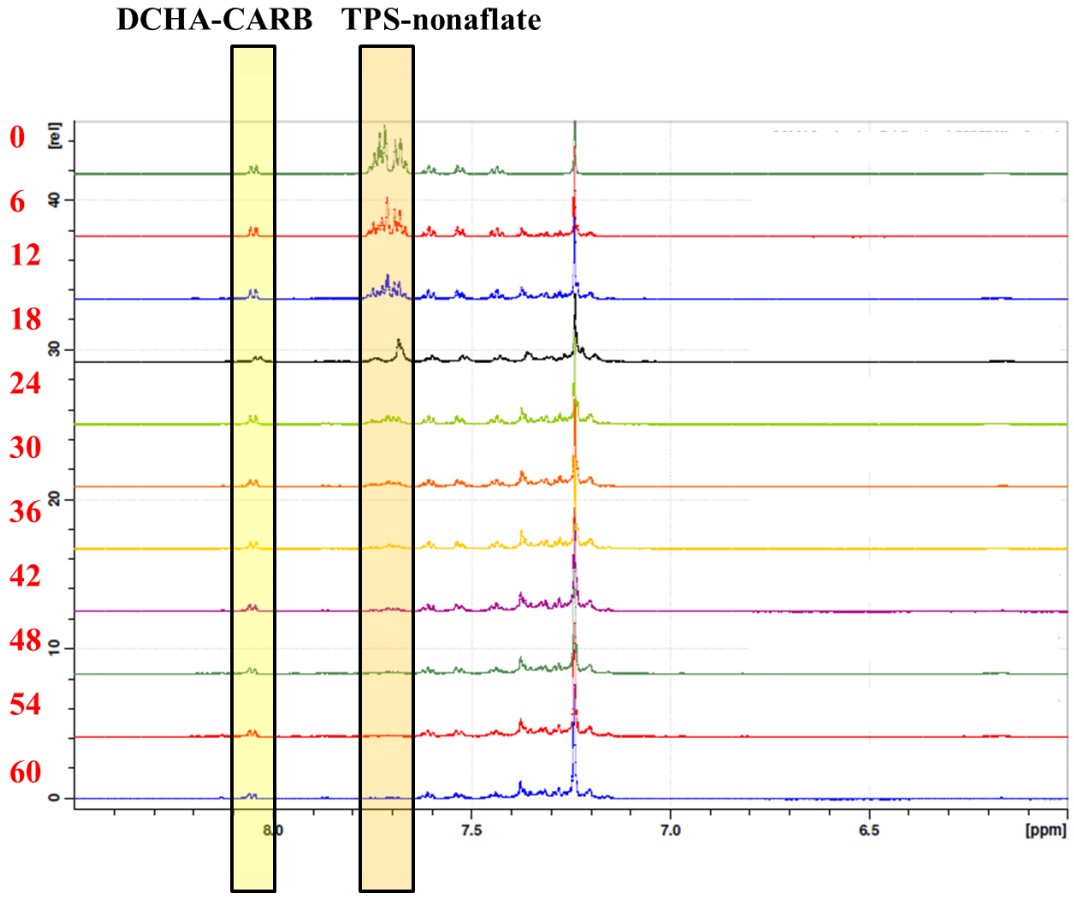

Figure 5.12: The aromatic region of 1H NMR spectra of a series of exposed silicon wafers at several exposure doses (shown at left in mJ/cm2). Highlighted are peaks corresponding to the unreacted PAG and PBG in the photoresist.

The integration values for the resist components are normalized to the aliphatic hydrogens in the polymer backbone, assuming that the polymer backbone is unaffected by the reaction of the PAG and the PBG, which is reasonable since no post-exposure bake was carried out after exposure. Figure 5.13 shows a plot of the integration constants for functional groups associated with the PBG, the PAG, and the quencher (TOA), normalized by the number of equivalent hydrogens and relative to the polymer peak. The PAG decays rapidly with dose and is fitted with an exponential decay, which yields an estimate of $k_{PAG} = 0.054$ cm^2/mJ. The PBG decay is much slower and can be fitted with a

linear function, which results in a k_{PBG} = 0.004 cm^2/mJ. A similar study of a photoresist film without PAG or TOA yielded k_{PBG} = 0.007 cm^2/mJ. This latter value was used in the modeling of the single-stage and two-stage PBGs above.

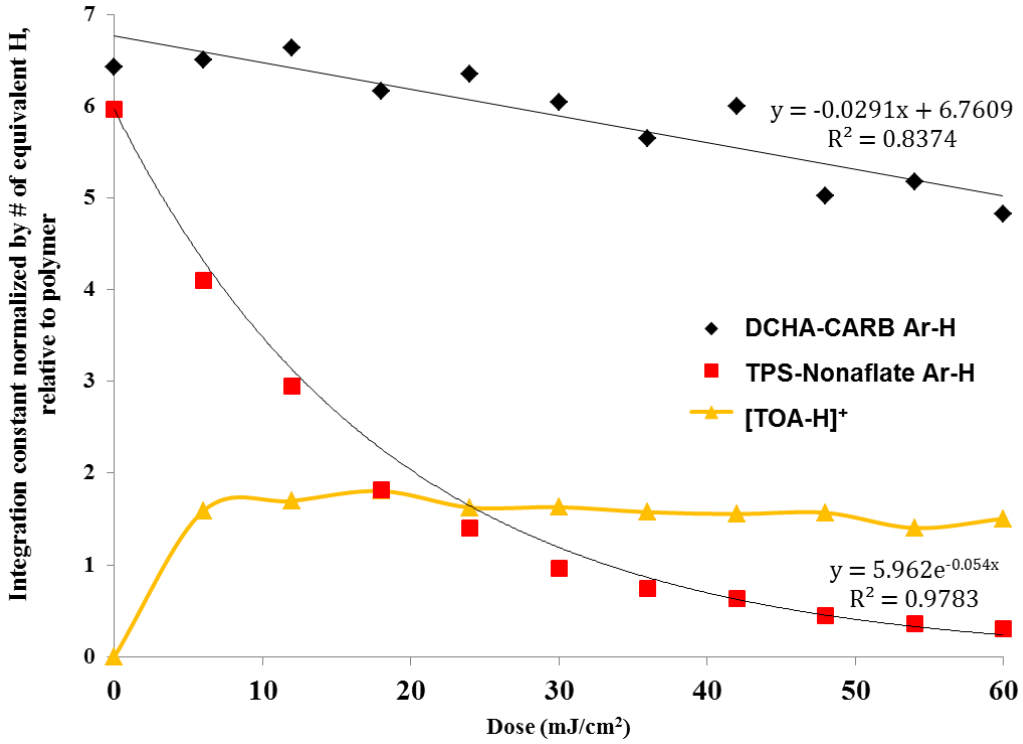

Figure 5.13: Normalized integration constants of photoresist components relative to a polymer peak. Fits of DCHA-Carb and TPS-Nonaflate were used to calculate kinetic constants.

5.5 EXPERIMENTAL

Silicon wafers were coated with a 70 nm bottom antireflection coating (BARC, Brewer Sciences), verified by spectroscopic ellipsometry. Photoresist was applied by hand to a wafer on an air-filtered track, followed by a post apply bake at 110 °C for 60 s. Exposures were done with an Amphibian interference lithography system[14] equipped with a 193 nm excimer laser (Coherent). To create contrast curves, the laser was arranged to bypass the imaging optics and was directed onto the wafer, which sat on an automated

stage. Patterned samples were exposed with a line-narrowed 193 nm excimer laser via a phase shift mask and Smith Talbot prism line in air (no immersion fluid). Low numerical aperture ("Low NA") exposures employed a 0.22 NA prism that produces an aerial image with a 240 nm half-pitch, while a "High NA" configuration operated with a 0.54 NA and produces 90 nm half-pitch lines and spaces. For full wafer exposures, the wafer moved at a constant speed under a line-shaped exposure region formed with a cylindrical lens. For NMR analysis of full wafer exposures, photoresist on exposed wafers was collected by dissolving in dichloromethane, evaporating and reconstituting in deuterated chloroform. ^{1}H NMR spectra were collected using a Bruker AVANCE 400 MHz NMR system with a Microprobe accessory for small samples. All SEM images were recorded on a Hitachi S-4700 SEM. Thicknesses for the contrast curves were obtained by spectroscopic ellipsometry with a VASE ellipsometer (J.A. Woollam Co., Inc.).

All photoresists were formulated in 2-heptanone (used as received from Sigma Aldrich) unless otherwise noted. The polymer resin used was methacrylate methyl adamantyl methacrylate-co-γ-butyrolactone methacrylate (MADMA-co-GBLMA), obtained from Dupont Electronic Materials, with a molar repeat unit ratio of 58:42 MADMA:GBLMA, a molecular weight of 5.2 kDa, and a polydispersity index of 1.5. The base quencher, trioctylamine was obtained from Sigma Aldrich. The TPS-nonaflate PAG was obtained from AZ Electronic Materials. DCHA-CARB was synthesized according to Gu *et al*.[3] Polymer-bound PAG and polymer-bound PBG resists were synthesized and purified according to Cho *et al*.[11] Photoresists were developed by dispensing a puddle of 2.38% aqueous tetramethylammonium hydroxide (TMAH) on them for 60 s, followed by a water rinse and a subsequent spin-off step.

5.6 CONCLUSION

Materials-based pitch division has the potential to be a less expensive alternative to other double patterning technologies, since the doubling of the spatial frequency is spontaneously performed by the resist. The pitch division results from the fact that the resist exhibits two solubility thresholds. The dual-threshold behavior is a result of the parabolic nature of the net acid vs. dose curve which is itself a result of the asymmetric kinetics of the PAG and the PBG.

Formulation and demonstration of a PBG-based pitch division resist composed of fully characterized chemicals enables improvement of resolution capability and LER of pitch-division photoresists by opening the door to studies of reaction kinetics, acid diffusion, acid-base neutralization kinetics, and optimization of line-edge acid gradients. Two-stage PBGs offer a solution to the problem of low acid gradients at the line edge, but modeling of resist kinetics suggests that high loadings of PBG will be necessary. Other issues such as absorption may well be dominant at higher loadings, especially since there is evidence that resist absorption already plays a role in the patterning of single-stage PBG-based resists. Characterization of two-stage PBGs in photoresist films by NMR spectroscopy will help determine the optimal loadings of the PBGs. Optimization of pitch division photoresists will be greatly aided by the understanding of how the interplay between PAG and PBG kinetics affects resist performance.

5.7 REFERENCES

1. Finders, J.; Dusa, M.; Vleeming, B.; Megens, H.; Hepp, B.; Maenhoudt, M.; Cheng, S.; Vandeweyer, T. In *Double patterning for 32nm and below: an update*, San Jose, CA, USA, 2008; Levinson, H. J.; Dusa, M. V., Eds. SPIE: San Jose, CA, USA, 2008; pp 692408-12.
2. Fonseca, C.; Somervell, M.; Scheer, S.; Printz, W.; Nafus, K.; Hatakeyama, S.; Kuwahara, Y.; Niwa, T.; Bernard, S.; Gronheid, R. In *Advances and challenges in dual-tone development process optimization*, San Jose, CA, USA, 2009;

Levinson, H. J.; Dusa, M. V., Eds. SPIE: San Jose, CA, USA, 2009; pp 72740I-12.

3. Gu, X.; Bates, C.; Cho, Y.; Costner, E.; Marzuka, F.; Nagai, T.; Ogata, T.; Shi, C.; Sundaresan, A. K.; Turro, N. J.; Bristol, R.; Zimmerman, P.; Wilson, C. G., A New Materials-based Pitch Division Technique. *Journal of Photopolymer Science and Technology* **2009,** 22, (6), 773-781.

4. Chae, K. H., Thermal curing reaction of poly(glycidyl methacrylate) using photogenerated amines from oxime-urethane derivatives. *Macromolecular Rapid Communications* **1998,** 19, (1), 1-4.

5. Ohba, T.; Nakai, D.; Suyama, K.; Shirai, M., Photo-Crosslinking of Poly(glycidyl methacrylate) Using Di-functional Photobase Generators. *Journal of Photopolymer Science and Technology* **2004,** 17, (1), 11-14.

6. Kanji, S.; Satoshi, N.; Masamitsu, S., Thermally Stable Carbamates as Novel Photobase Generator. *Journal of Photopolymer Science and Technology* **2005,** 18, (1), 141-148.

7. Suyama, K.; Shirai, M., Photobase generators: Recent progress and application trend in polymer systems. *Progress in Polymer Science* **2009,** 34, (2), 194-209.

8. Gu, X.; Bates, C. M.; Cho, Y.; Kawakami, T.; Nagai, T.; Ogata, T.; Sundaresan, A. K.; Turro, N. J.; Bristol, R.; Zimmerman, P.; Willson, C. G. In *Photobase generator assisted pitch division*, San Jose, California, USA, 2010; Allen, R. D., Ed. SPIE: San Jose, California, USA, 2010; pp 763906-12.

9. Pawloski, A. R.; Acheta, A.; Lalovic, I.; La Fontaine, B. M.; Levinson, H. J. In *Characterization of line-edge roughness in photoresist using an image fading technique*, Santa Clara, CA, USA, 2004; Sturtevant, J. L., Ed. SPIE: Santa Clara, CA, USA, 2004; pp 414-425.

10. Bristol, R. L. In *The tri-lateral challenge of resolution, photospeed, and LER: scaling below 50nm?*, San Jose, CA, USA, 2007; Lin, Q., Ed. SPIE: San Jose, CA, USA, 2007; pp 65190W-11.

11. Cho, Y.; Gu, X.; Hagiwara, Y.; Kawakami, T.; Ogata, T.; Rawlings, B.; Li, Y.; Sundaresan, A. K.; Turro, N. J.; Bristol, R.; Blackwell, J. M.; Willson, C. G. In *Polymer-bound photobase generators and photoacid generators for pitch division lithography*, San Jose, California, USA, 2011; Allen, R. D.; Somervell, M. H., Eds. SPIE: San Jose, California, USA, 2011; pp 797221-8.

12. Vogt, B. D.; Kang, S.; Prabhu, V. M.; Rao, A.; Lin, E. K.; Wu, W.-l.; Satija, S. K.; Turnquest, K., Influence of base additives on the reaction-diffusion front of model chemically amplified photoresists. *Journal of Vacuum Science & Technology B: Microelectronics and Nanometer Structures* **2007,** 25, (1), 175-182.

13. Gu, X.; Cho, Y.; Kawakami, T.; Hagiwara, Y.; Rawlings, B.; Mesch, R.; Ogata, T.; Kim, T.; Seshimo, T.; Wang, W.; Sundaresan, A. K.; Turro, N. J.; Gronheid, R.; Blackwell, J.; Bristol, R.; Willson, C. G. In *Photobase generator enabled pitch division: a progress report*, San Jose, California, USA, 2011; Allen, R. D.; Somervell, M. H., Eds. SPIE: San Jose, California, USA, 2011; pp 79720F-13.

14. Smith, B. W.; Bourov, A.; Fan, Y.; Cropanese, F.; Hammond, P. In *Amphibian XIS: an immersion lithography microstepper platform*, San Jose, CA, USA, 2004; Smith, B. W., Ed. SPIE: San Jose, CA, USA, 2004; pp 751-759.

Chapter 6: Conclusion and future work

The stabilizing effect of multiple crosslinkable groups across the chromophore can be exploited in a number of ways. The NLO polymeric materials described can be incorporated into waveguide modulator devices such as Mach-Zehnder interferometers or more advanced photonic structures such as photonic crystals. In addition, since the thermal stability is achieved by photoinitiated polymerization, the NLO properties could be patterned by exposing the NLO material through a photomask in a manner similar to a photoresist.

To achieve a thermally stable high NLO efficiency suitable for devices, future inquiry should focus on improving the maximum obtainable SHG and EO coefficients. This can be done by employing more efficient chromophores and donors, which will incur the additional benefit of moving the absorption maximum of the chromophore outside the absorption region of photoinitiators. Additional thermal stability is possible by replacing the norbornene polymerizable group with more stable groups such as those exemplified in Figure 6.1. Although these would require higher poling temperatures, they would potentially allow for thermal stability at temperatures greater than 200°C, provided that the chromophore is stable at elevated temperatures.

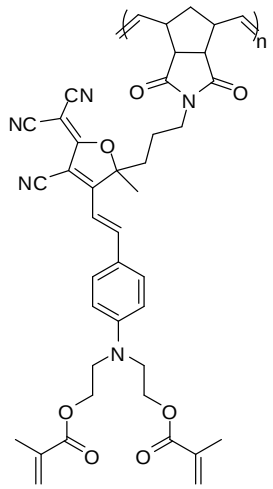

Figure 6.1: Exemplar of a chromophore synthesized via ring-opening metathesis polymerization of N-phenylnorbornene-5,6-dicarboximide (NDI)

The dual-tone photoresist that was formulated shows the ability to store and transfer two latent images that are selected by exposure wavelength. This allows for the patterning of two-layer structures without an alignment step, a feature that is beneficial in the patterning of electronics on flexible or large area substrates. One logical extension of dual-tone photoresists is to smaller feature sizes. The minimum resolution obtainable by the novolak/DNQ/crosslinker formulation is limited by the exposure wavelength as described by Rayleigh's equation, so an adaptation of a dual-tone photoresist would involve systems with PAGs and dissolution inhibitors that are active at smaller wavelengths. The nature of the crosslinking reaction must be adapted as well, since highly absorbing phenolic resins are not appropriate for deep UV resists. As in the dual threshold resist for pitch division, a combination of PAGs and PBGs could be used to activate positive or negative responses.

For PBG-based pitch division, the realization of a photoresist formulated with well characterized and commercially available components suggests a number of avenues of further inquiry. The characterization of photoresist kinetics in the film provides a

valuable tool for evaluating new classes of PBGs, such as oxime esters, that may be more suitable for pitch division applications. This new information can be used to predict optimal formulations for maximizing the obtainable acid gradient at the line edge.

Possible two-staged PBGs are being designed and synthesized, including acetophenone-protected PBGs that react in a two-stage series reaction to produce base. Characterization of the kinetics of such PBGs is possible in solution via NMR or ion chromatography, but these methods should be supplemented with NMR of photoresist films to verify that the two-stage kinetics are observed in solid films. The usefulness of two-stage photoresists depends on the ratio of the kinetics constants of the first and second steps. The ideal situation is one where the two constants are roughly equal. Further into the future, other pitch division strategies such as negative tone development or sidewall spacers could even be combined with dual-threshold resists to produce additional pitch division.

Appendix A: Analysis of Maker Fringes

This analysis shows a derivation for transmission of SHG through a thin film of nonlinear optical material supported by a transparent substrate. The present analysis treats the *p*-to-*p* transmission, that is, it considers only the *p*-polarized incident and transmitted waves.

Starting with Maxwell's equations:

$$\begin{aligned} \nabla \cdot \widetilde{\mathbf{D}} &= \tilde{\rho} \\ \nabla \cdot \widetilde{\mathbf{B}} &= 0 \\ \nabla \times \tilde{\mathbf{E}} &= -\frac{\partial \widetilde{\mathbf{B}}}{\partial t} \\ \nabla \times \widetilde{\mathbf{H}} &= \frac{\partial \widetilde{\mathbf{D}}}{\partial t} + \tilde{\mathbf{J}} \end{aligned} \qquad \text{A.1}$$

We make the following assumptions: no free charges, $\tilde{\rho} = 0$; no free currents, $\tilde{\mathbf{J}} = 0$. 3; and nonmagnetic material $\widetilde{\mathbf{B}} = \mu_0 \widetilde{\mathbf{H}}$. We also assume the material is nonlinear, so $\widetilde{\mathbf{D}} = \epsilon_0 \tilde{\mathbf{E}} + \widetilde{\mathbf{P}}$. Taking the curl of the 3rd equation above:

$$\nabla \times \nabla \times \tilde{\mathbf{E}} = -\frac{\partial}{\partial t} \nabla \times \widetilde{\mathbf{B}} = -\mu_0 \frac{\partial}{\partial t} \nabla \times \widetilde{\mathbf{H}}$$

Using the 4th Maxwell equation:

$$\nabla \times \nabla \times \tilde{\mathbf{E}} = -\mu_0 \frac{\partial^2}{\partial t^2} \widetilde{\mathbf{D}} = -\frac{1}{c^2} \frac{\partial^2 \tilde{\mathbf{E}}}{\partial t^2} - \frac{1}{\epsilon_0 c^2} \frac{\partial^2 \widetilde{\mathbf{P}}}{\partial t^2}$$

The polarization consists of a component due to nonlinear optical effects as well as a linear polarization: $\widetilde{\mathbf{P}} = \widetilde{\mathbf{P}}^{(1)} + \widetilde{\mathbf{P}}^{\mathrm{NL}}$.

A vector identity relates the curl of the curl to the Laplacian, plus another term:

$$\nabla \times \nabla \times \tilde{\mathbf{E}} = \nabla\left(\nabla \cdot \tilde{\mathbf{E}}\right) - \nabla^2 \tilde{\mathbf{E}}$$

The first of Maxwell's equations listed above tell us that the divergence of the electric displacement is zero. It would be convenient if the divergence of the electric field

$\boldsymbol{E}$ is also zero, so that only the Laplacian term remains. Introducing the dielectric tensor, we can find an alternate expression for the polarization: $\widetilde{\mathbf{P}} = \epsilon_0\boldsymbol{\epsilon}^{(\mathbf{1})} \cdot \tilde{\mathbf{E}} - \epsilon_0\tilde{\mathbf{E}} + \widetilde{\mathbf{P}}^{\mathrm{NL}}$, so that $\widetilde{\mathbf{D}} = \epsilon_0\boldsymbol{\epsilon}^{(\mathbf{1})} \cdot \tilde{\mathbf{E}} + \widetilde{\mathbf{P}}^{\mathrm{NL}}$**.** There are two conditions, then, for the divergence of the field to be zero: first, $\boldsymbol{\epsilon}^{(\mathbf{1})}$ must be isotropic. Second, the divergence of $\widetilde{\boldsymbol{P}}^{\boldsymbol{NL}}$ must be zero. In general, in nonlinear optics, this is not true. For the case of second harmonic generation, this is only true for the case where the nonlinear coefficient of the material is isotropic (not typical).

The differential equation can be solved by separation of variables. In this case, the solution is of the form: $\tilde{\mathbf{E}} = \mathbf{E}_{\mathrm{n}}(\mathbf{r})\exp(-i\omega t)$, with a similar form for $\boldsymbol{P}^{\boldsymbol{NL}}$**.** Plugging this into the wave equation above, we find:

$$\nabla^2\mathbf{E}_n(\mathbf{r}) - \nabla(\nabla \cdot \mathbf{E}_n(\mathbf{r})) + \frac{\omega_n^2}{c^2}\boldsymbol{\epsilon}^{(\mathbf{1})}(\omega_n) \cdot \mathbf{E}_n(\mathbf{r}) = -\frac{\omega_n^2}{\epsilon_0 c^2}\mathbf{P}_n^{\mathrm{NL}}(\mathbf{r})$$

In this equation, the index n represents each frequency component. The incident wave is a plane wave at frequency ω:

$$\mathbf{E}_{1v} = \hat{\mathbf{e}}_v E_1 \exp[i(\mathbf{q}_1 \cdot \mathbf{r})]$$

For p-incidence, $\hat{\mathbf{e}}_v = (\cos\theta, 0, -\sin\theta)$; for s-incidence, $\hat{\mathbf{e}}_v = (0,1,0)$. Also, $\mathbf{q}_1 = \frac{n_1(\omega)\omega}{c}(\sin\theta, 0, \cos\theta)$.

The second harmonic frequency component in region 1 is found by analysis of SHG reflection. In general, for any waves at a plane interface, the component of the wavevector parallel to the surface must be equal for all the waves, or else the boundary conditions can only be satisfied at isolated points on the surface. At frequency ω, for reflected waves, this is simply the law of reflection, that is, the incident angle is equal to the reflected angle (judged from the normal). For transmitted waves, this amounts to Snell's law, which states that the product of the index of refraction and the sine of the angle is the same for incident and refracted waves.

The waves at frequency ω are, in region 1, for the reflected wave:

$$\mathbf{E}_{1v} = \left[r_{af}^{1v}\right]\hat{\mathbf{e}}_v^r E_1 \exp[i(\mathbf{q}_1^r \cdot \mathbf{r})]$$

In this expression, $\mathbf{q}_1^r = \frac{n_1(\omega)\omega}{c}(\sin\theta, 0, -\cos\theta)$, $\hat{\mathbf{e}}_s^r = (0,1,0)$, $\hat{\mathbf{e}}_p^r = (-\cos\theta\,, 0, -\sin\theta)$, and $\left[r_{af}^{1v}\right]$ is the reflection coefficient given by the Fresnel formulae:

$$\left[r_{af}^{1s}\right] = \frac{\sin(\theta_t - \theta)}{\sin(\theta_t + \theta)}$$

and

$$\left[r_{af}^{1p}\right] = -\frac{\tan(\theta_t - \theta)}{\tan(\theta_t + \theta)}$$

with θ_t given by Snell's law applied at the air-film surface.

Similarly, the transmitted wave is, in region 2, when there is no birefringence:

$$\mathbf{E}_{1v} = \left[t_{af}^{1v}\right]\hat{\mathbf{e}}_v^t E_1 \exp[i\mathbf{k}_1^t \cdot \mathbf{r}]$$

where $\mathbf{k}_1^t = \frac{n_2(\omega)\omega}{c}(\sin\theta_t, 0, \cos\theta_t)$, $\hat{\mathbf{e}}_s^t = (0,1,0)$, $\hat{\mathbf{e}}_p^t = (\cos\theta_t\,, 0, -\sin\theta_t)$, and $\left[t_{af}^{1s}\right] = \frac{2\sin\theta_t\cos\theta}{\sin(\theta_t+\theta)}$ and $\left[t_{af}^{1p}\right] = \frac{2\sin\theta_t\cos\theta}{\sin(\theta_t+\theta)\cos(\theta_t-\theta)}$, where, again, θ_t is given by Snell's law applied at the air-film surface.

For the birefringent case, the index will be dependent on the polarization. The same type of analysis can be carried out at the interface between the NLO film and the substrate.

At frequency 2ω, there is no incident SHG wave, but there is a reflected SHG wave and a transmitted SHG wave, as well as a polarization wave (nonlinear response) due to the transmitted fundamental wave. The polarization wave is related to the fundamental wave by the coefficient *d*:

$$\mathbf{P}^{\mathrm{NL}} = 2\epsilon_0 \mathbf{d}\colon \mathbf{E}_{1v}\mathbf{E}_{1v} = 2\epsilon_0 |E_1|^2 \left[t_{af}^{1v}\right]^2 \exp[i2\mathbf{k}_1^t \cdot \mathbf{r}]\, \mathbf{d}\colon \hat{\mathbf{e}}_v^t \hat{\mathbf{e}}_v^t$$

For the reflected ray:

$$\mathbf{E}_{2v} = R\hat{\mathbf{e}}_{2v}^{r} \exp\left[i(\mathbf{q}_2^r \cdot [\mathbf{r} + \frac{L}{2}\hat{\mathbf{z}}])\right]$$

$$\mathbf{H}_{2v} = R\hat{\mathbf{e}}_{2\bar{v}}^{r} n_1(2\omega)\sqrt{\frac{\epsilon_0}{\mu_0}} \exp\left[i(\mathbf{q}_2^r \cdot [\mathbf{r} + \frac{L}{2}\hat{\mathbf{z}}])\right]$$

where $\mathbf{q}_2^r = \frac{n_1(2\omega)2\omega}{c}(\sin\theta_r, 0, -\cos\theta_r)$, $\hat{\mathbf{e}}_{2v}^{r} = (-\cos\theta_r, 0, -\sin\theta_r)$, and the phase factor of *L/2* is due to the boundary conditions.

The requirement that the components of the wavevector parallel to the surface must be equal gives the following: $\frac{n_1(2\omega)2\omega}{c}\sin\theta_{2r} = \frac{2n_2(\omega)\omega}{c}\sin\theta_t = \frac{2n_1(\omega)\omega}{c}\sin\theta$ which simplifies to the law of reflection for SHG,

$$n_1(\omega)\sin\theta = n_1(2\omega)\sin\theta_{2r}$$

For the transmitted ray, there is a similar law:

$$n_1(\omega)\sin\theta = n_2(2\omega)\sin\theta_{2t}$$

For the second harmonic wave in region II, it is instructive to show one process for finding the solution to the wave equation. The wave equation is, for the isotropic case:

$$\nabla^2\mathbf{E}_2(\mathbf{r}) - \nabla\big(\nabla\cdot\mathbf{E}_2(\mathbf{r})\big) + \frac{n_2^2(2\omega)(2\omega)^2}{c^2}\mathbf{E}_2(\mathbf{r}) = -\frac{(2\omega)^2}{\epsilon_0 c^2}2\epsilon_0|E_1|^2\left[t_{af}^{1v}\right]^{\mathbf{2}}\exp[i\,(2\mathbf{k}_1^t\cdot\mathbf{r})]\,\mathbf{d}\colon\hat{\mathbf{e}}_v^t\hat{\mathbf{e}}_v^t$$

First, it is necessary to find the homogeneous solutions, where the right hand side vanishes.

$$\nabla^2\mathbf{E}_2(\mathbf{r}) - \nabla\big(\nabla\cdot\mathbf{E}_2(\mathbf{r})\big) + \frac{n_2^2(2\omega)(2\omega)^2}{c^2}\mathbf{E}_2(\mathbf{r}) = \mathbf{0}$$

Since we have assumed an isotropic index, and since there is no nonlinear term, it is safe to look for a solution where $\nabla\cdot\mathbf{E}_2(\mathbf{r}) = 0$, which is true for transverse plane waves.

Looking at the individual Cartesian components, for the homogeneous equation,

$$\nabla^2 E_x(\mathbf{r}) + \frac{n_2^2(2\omega)(2\omega)^2}{c^2}E_x(\mathbf{r}) = 0$$

$$\nabla^2 E_y(\mathbf{r}) + \frac{n_2^2(2\omega)(2\omega)^2}{c^2} E_y(\mathbf{r}) = 0$$
$$\nabla^2 E_z(\mathbf{r}) + \frac{\mathrm{n}_2^2(2\omega)(2\omega)^2}{\mathrm{c}^2} E_z(\mathbf{r}) = 0$$

The solutions are exponentials, in particular, plane waves. For example:

$$E_{2x}(\mathbf{r}) = A_x \exp[\mathrm{i}(\mathbf{k_2} \cdot \mathbf{r})] + B_x \exp[\mathrm{i}(\mathbf{k}_2^{\mathrm{r}} \cdot \mathbf{r})]$$

where $\mathbf{k_2}$ and $\mathbf{k}_2^{\mathrm{r}}$ satisfy $|\mathbf{k_2}|^2 = |\mathbf{k}_2^{\mathrm{r}}|^2 = \frac{\mathrm{n}_2^2(2\omega)(2\omega)^2}{\mathrm{c}^2}$.

The boundary conditions at the I-II interface and the II-III interface will determine the value of A_x and B_x. However, the wave condition must also hold at the boundary, which implies, as we determined before, that the components of $\mathbf{k_2}$ and $\mathbf{k}_2^{\mathrm{r}}$ parallel to the boundary must match those of all other waves at this frequency. The boundary is the xy-plane, so both the x- and y- components of the all wave vectors must match. We assumed a plane wave propagating in the xz-plane, so the y component of the polarization wavevector (equal to $2\mathbf{q}_1^t$, see above) is zero. Therefore, $k_{2y} = k_{2y}^r = 0$. Also, the x-component of the polarization wave vector is $2\mathbf{q}_{1x}^t = \frac{2n_2(\omega)\omega}{c}\sin\theta_t = \frac{2n_1(\omega)\omega}{c}\sin\theta$, using Snell's law. This must equal $\mathrm{k_{2x}}$ and k_{2x}^r: $k_{2y} = k_{2y}^r = \frac{2n_1(\omega)\omega}{c}\sin\theta$. Now, the z-component is determined:

$$k_{2z} = \pm\sqrt{|\mathbf{k}_2|^2 - \left(\frac{2n_1(\omega)\omega}{c}\right)^2 \sin^2\theta} = \pm\sqrt{\frac{n_2^2(2\omega)(2\omega)^2}{c^2} - \left(\frac{2n_1(\omega)\omega}{c}\right)^2 \sin^2\theta}$$
$$= \pm\frac{2\omega}{c}\sqrt{n_2^2(2\omega) - \mathrm{n}_1^2(\omega)\sin^2\theta}.$$

To shorten these expressions, let $s_m = \frac{n_1(\omega)}{n_2(m\omega)}\sin\theta$ and $c_m = \sqrt{1 - s_m^2}$, and now we can write

$$\mathbf{k_2} = \frac{2\omega n_2(2\omega)}{c}(s_2, 0, c_2)$$

$$\mathbf{k}_2^{\mathrm{r}} = \frac{2\omega n_2(2\omega)}{c}(s_2, 0, -c_2)$$

Since we also assumed $\nabla \cdot \mathbf{E}_{2\mathrm{hom}}(\mathbf{r}) = 0$ for the homogeneous solutions, this implies, given the solution we have found, that $A_x k_{2x} + A_y k_{2y} + A_z k_{2z} = \mathbf{A} \cdot \mathbf{k_2} = 0$ and $\mathbf{B} \cdot \mathbf{k}_2^r = 0$ as well. Thus, in order for our assumption to be justified, $\mathbf{A} = A\hat{\mathbf{e}}_p$ and $\mathbf{B} = B\hat{\mathbf{e}}_p^r$, where,

$$\hat{\mathbf{e}}_{2p} = (c_2, 0, -s_2)$$

$$\hat{\mathbf{e}}_{2p}^r = (-c_2, 0, -s_2)$$

For the case of s-waves, $\hat{\mathbf{e}}_{2s} = \hat{\mathbf{e}}_{2s}^r = (0,1,0)$.

The particular solution to the following wave equation must now be determined:

$$\nabla^2 \mathbf{E}_2(\mathbf{r}) - \nabla\big(\nabla \cdot \mathbf{E}_2(\mathbf{r})\big) + \frac{n_2^2(2\omega)(2\omega)^2}{c^2}\mathbf{E}_2(\mathbf{r}) = -\frac{(2\omega)^2}{\epsilon_0 c^2} 2\epsilon_0 |E_1|^2 \left[t_{af}^{1v}\right]^{\mathbf{2}} \exp[i\,(2\mathbf{k}_1^t \cdot \mathbf{r})]\, \overleftrightarrow{\mathbf{d}} : \hat{\mathbf{e}}_v^t \hat{\mathbf{e}}_v^t$$

Note that in this case, the presence of the nonlinear source term means that the solution will not satisfy $\nabla \cdot \mathbf{E}(\mathbf{r}) = 0$.

Following the method of undetermined coefficients, a solution of the same form as the source term is found: $\mathbf{E}_p = \mathbf{e}_b \exp[i\,(2\mathbf{k}_1^t \cdot \mathbf{r})] + \mathbf{N} \exp[-i\,(2\mathbf{k}_1^t \cdot \mathbf{r})]$. Plugging this into the wave equation:

$$\begin{aligned} -4(k_1^t)^2 \mathbf{e}_b \exp[i\,(2\mathbf{k}_1^t \cdot \mathbf{r})] - 4(k_1^t)^2 \mathbf{N} \exp[-i\,(2\mathbf{k}_1^t \cdot \mathbf{r})] \\ + 4\mathbf{k}_1^t\,(\mathbf{k}_1^t \cdot \mathbf{M}) \exp[i\,(2\mathbf{k}_1^t \cdot \mathbf{r})] + 4\mathbf{k}_1^t\,(\mathbf{k}_1^t \cdot \mathbf{N}) \exp[-i\,(2\mathbf{k}_1^t \cdot \mathbf{r})] \\ + \frac{n_2^2(2\omega)(2\omega)^2}{c^2}\{\mathbf{e}_b \exp[i\,(2\mathbf{k}_1^t \cdot \mathbf{r})] + \mathbf{N} \exp[-i\,(2\mathbf{k}_1^t \cdot \mathbf{r})]\} \\ = -\frac{(2\omega)^2}{\epsilon_0 c^2} 2\epsilon_0 |E_1|^2 \left[t_{af}^{1v}\right]^{\mathbf{2}} \exp[i(2\mathbf{k}_1^t \cdot \mathbf{r})]\, \overleftrightarrow{\mathbf{d}} : \hat{\mathbf{e}}_v^t \hat{\mathbf{e}}_v^t \end{aligned}$$

For this to hold, **N=0**, so we have:

$$\begin{aligned} -4(k_1^t)^2 \mathbf{e}_b \exp[i\,(2\mathbf{k}_1^t \cdot \mathbf{r})] + 4\mathbf{k}_1^t\,(\mathbf{k}_1^t \cdot \mathbf{e}_b) \exp[i\,(2\mathbf{k}_1^t \cdot \mathbf{r})] \\ + \frac{n_2^2(2\omega)(2\omega)^2}{c^2}\mathbf{e}_b \exp[i\,(2\mathbf{k}_1^t \cdot \mathbf{r})] \\ = -\frac{(2\omega)^2}{\epsilon_0 c^2} 2\epsilon_0 |E_1|^2 \left[t_{af}^{1v}\right]^{\mathbf{2}} \exp[i(2\mathbf{k}_1^t \cdot \mathbf{r})]\, \overleftrightarrow{\mathbf{d}} : \hat{\mathbf{e}}_v^t \hat{\mathbf{e}}_v^t \end{aligned}$$

Dividing out the exponential,

$$-4(k_1^t)^2\mathbf{e}_b + 4\mathbf{k}_1^t\,(\mathbf{k}_1^t\cdot\mathbf{e}_b) + \frac{n_2^2(2\omega)(2\omega)^2}{c^2}\mathbf{e}_b \;= -\frac{(2\omega)^2}{\epsilon_0 c^2}2\epsilon_0|E_1|^2\left[t_{af}^{1v}\right]^2\,\overleftrightarrow{\mathbf{d}}\!:\hat{\mathbf{e}}_v^t\hat{\mathbf{e}}_v^t$$

Letting $\widetilde{\mathbf{P}}^{\mathrm{NL}} = 2\epsilon_0|E_1|^2\left[t_{af}^{1v}\right]^2\,\overleftrightarrow{\mathbf{d}}\!:\hat{\mathbf{e}}_v^t\hat{\mathbf{e}}_v^t$ and $\mathbf{k}_b = 2\mathbf{k}_1^t$, we obtain

$$-|\mathbf{k}_b|^2\mathbf{e}_b + \mathbf{k}_b\,(\mathbf{k}_b\cdot\mathbf{e}_b) + |\mathbf{k}_2|^2\mathbf{e}_b \;= -\frac{(2\omega)^2}{\epsilon_0 c^2}\widetilde{\mathbf{P}}^{\mathrm{NL}}$$

Taking the dot product of both sides of the above equation with $\mathbf{k}_b$, we obtain a new equation:

$$-|\mathbf{k}_b|^2(\mathbf{e}_b\cdot\mathbf{k}_b) + |\mathbf{k}_b|^2\,(\mathbf{k}_b\cdot\mathbf{e}_b) + |\mathbf{k}_2|^2(\mathbf{e}_b\cdot\mathbf{k}_b) \;= -\frac{(2\omega)^2}{\epsilon_0 c^2}(\widetilde{\mathbf{P}}^{\mathrm{NL}}\cdot\mathbf{k}_b)$$

Evaluating this,

$$(\mathbf{k}_b\cdot\mathbf{e}_b) = -\frac{(2\omega)^2}{\epsilon_0 c^2|\mathbf{k}_2|^2}(\widetilde{\mathbf{P}}^{\mathrm{NL}}\cdot\mathbf{k}_b)$$

Substituting for $(\mathbf{k}_b\cdot\mathbf{e}_b)$ in the previous equation gives

$$-|\mathbf{k}_b|^2\mathbf{e}_b - \mathbf{k}_b\frac{(2\omega)^2}{\epsilon_0 c^2|\mathbf{k}_2|^2}(\widetilde{\mathbf{P}}^{\mathrm{NL}}\cdot\mathbf{k}_b) + |\mathbf{k}_2|^2\mathbf{e}_b \;= -\frac{(2\omega)^2}{\epsilon_0 c^2}\widetilde{\mathbf{P}}^{\mathrm{NL}}$$

Solving for $\mathbf{e}_b$,

$$\mathbf{e}_b \;= \frac{\mathbf{1}}{\epsilon_0(|\mathbf{k}_b|^2 - |\mathbf{k}_2|^2)}\frac{(2\omega)^2}{c^2}\left[\widetilde{\mathbf{P}}^{\mathrm{NL}} - \frac{\mathbf{k}_b(\mathbf{k}_b\cdot\widetilde{\mathbf{P}}^{\mathrm{NL}})}{|\mathbf{k}_2|^2}\right]$$

In summary, for the electric field of the SHG wave in region II,

$$\mathbf{E}_2(\mathbf{r}) = A\hat{\mathbf{e}}_{2v}\exp[i(\mathbf{k}_2\cdot\mathbf{r})] + B\hat{\mathbf{e}}_{2v}^r\exp[i(\mathbf{k}_2^r\cdot\mathbf{r})] + \mathbf{e}_b\exp[i(2\mathbf{k}_1^t\cdot\mathbf{r})]$$

A and *B* are determined from the boundary conditions. At each boundary, the components of the electric field and magnetic field parallel to the surface must be continuous across the surface. Therefore, the magnetic field must also be computed, using $\nabla\times\tilde{\mathbf{E}} = -\mu_0\frac{\partial\tilde{\mathbf{H}}}{\partial t}$ for a nonmagnetic material. This implies $\nabla\times\mathbf{E}_n(\mathbf{r}) = \mu_0 i\omega_n\mathbf{H}_n(\mathbf{r})$, so that $\mathbf{H}_n(\mathbf{r}) = \frac{1}{\mu_0 i\omega_n}\nabla\times\mathbf{E}_n(\mathbf{r})$. All of the electric fields are of the form $\mathbf{E}_n(\mathbf{r}) = \mathbf{E}_n\exp[i(\mathbf{k}\cdot\mathbf{r})]$. For this form, $\nabla\times\mathbf{E}_n(\mathbf{r}) = i\mathbf{k}\times\mathbf{E}_n\exp[i(\mathbf{k}\cdot\mathbf{r})] = i\mathbf{k}\times\mathbf{E}_n(\mathbf{r})$, so $\mathbf{H}_n(\mathbf{r}) = \frac{1}{\mu_0\omega_n}\,\mathbf{k}\times\mathbf{E}_n(\mathbf{r})$. We can now compute the magnetic field:

$$\mathbf{H}_2(\mathbf{r}) = A\big(\hat{\mathbf{k}}_2 \times \hat{\mathbf{e}}_{2v}\big)n_2(2\omega)\sqrt{\frac{\epsilon_0}{\mu_0}}\exp[i(\mathbf{k}_2 \cdot \mathbf{r})]$$
$$+ B\big(\hat{\mathbf{k}}_2^r \times \hat{\mathbf{e}}_{2v}^r\big)n_2(2\omega)\sqrt{\frac{\epsilon_0}{\mu_0}}\exp[i(\mathbf{k}_2^r \cdot \mathbf{r})]$$
$$+ \big(\hat{\mathbf{k}}_1^t \times \mathbf{e}_b\big)n_2(\omega)\sqrt{\frac{\epsilon_0}{\mu_0}}\exp[i(2\mathbf{k}_1^t \cdot \mathbf{r})]$$

More explicitly, using some vector algebra,

$$\hat{\mathbf{k}}_2 \times \hat{\mathbf{e}}_{2p} = (s_2, 0, c_2) \times (c_2, 0, -s_2) = (0,1,0) = \hat{\mathbf{e}}_{2s}$$
$$\hat{\mathbf{k}}_2^r \times \hat{\mathbf{e}}_{2p}^r = (s_2, 0, -c_2) \times (-c_2, 0, -s_2) = \hat{\mathbf{e}}_{2s}^r$$
$$\hat{\mathbf{k}}_2 \times \hat{\mathbf{e}}_{2s} = -\hat{\mathbf{e}}_{2p}$$
$$\hat{\mathbf{k}}_2^r \times \hat{\mathbf{e}}_{2s}^r = \hat{\mathbf{e}}_{2p}^r$$

Defining $\mathbf{h}_b = \sqrt{\frac{\epsilon_0}{\mu_0}}n_2(\omega)\big(\hat{\mathbf{k}}_1^t \times \mathbf{e}_b\big)$, we obtain, for p-incidence,

$$\mathbf{H}_2(\mathbf{r}) = \sqrt{\frac{\epsilon_0}{\mu_0}}\left(A\hat{\mathbf{e}}_{2s}n_2(2\omega)\exp[i(\mathbf{k}_2 \cdot \mathbf{r})] + B\hat{\mathbf{e}}_{2s}^r n_2(2\omega)\exp[i(\mathbf{k}_2^r \cdot \mathbf{r})]\right)$$
$$+ \mathbf{h}_b \exp[i(2\mathbf{k}_1^t \cdot \mathbf{r})]$$

(For s-incidence, $\hat{\mathbf{e}}_{2s}$ is replaced with $-\hat{\mathbf{e}}_{2p}$ in the above equation.)

At the boundary between region I and II (the plane z=-L/2), the tangential components of **E** and **H** must be continuous. At z=0, the reflected SHG in region 1 is

$$\mathbf{E}_{2v} = R\hat{\mathbf{e}}_v^r \exp\left[i(\mathbf{q}_2^r \cdot [\mathbf{r} + \frac{L}{2}\hat{\mathbf{z}}])\right]$$
$$\mathbf{H}_{2v} = R\hat{\mathbf{e}}_v^r n_1(2\omega)\sqrt{\frac{\epsilon_0}{\mu_0}}\exp\left[i(\mathbf{q}_2^r \cdot [\mathbf{r} + \frac{L}{2}\hat{\mathbf{z}}])\right]$$

In region 2:

$$\mathbf{E}_{2v}(\mathbf{r}) = A\hat{\mathbf{e}}_{2v}\exp[i(\mathbf{k}_2 \cdot \mathbf{r})] + B\hat{\mathbf{e}}_{2v}^r\exp[i(\mathbf{k}_2^r \cdot \mathbf{r})] + \mathbf{e}_b\exp[i(2\mathbf{k}_1^t \cdot \mathbf{r})]$$

$$\mathbf{H}_{2v}(\mathbf{r}) = \sqrt{\frac{\epsilon_0}{\mu_0}}\left(A\hat{\mathbf{e}}_{2\bar{v}}n_2(2\omega)\exp[i(\mathbf{k}_2\cdot\mathbf{r})] + B\hat{\mathbf{e}}^r_{2\bar{v}}n_2(2\omega)\exp[i(\mathbf{k}^r_2\cdot\mathbf{r})]\right)$$

$$+ \mathbf{h}_b\exp[i(2\mathbf{k}^t_1\cdot\mathbf{r})]$$

For the case where *v*=*p*, continuity of the electric field implies that:

$$-R\cos\theta_r = \sqrt{1-\left(\frac{n_1(\omega)}{n_2(2\omega)}\sin\theta\right)^2}\left(A\exp\left[-\frac{ik_{2z}L}{2}\right] - B\exp\left[\frac{ik_{2z}L}{2}\right]\right)$$

$$+ e_{bx}\exp[-i(k_{1z}L)]$$

Continuity of the magnetic field implies:

$$R\,n_1(2\omega) = An_2(2\omega)\exp\left[-\frac{ik_{2z}L}{2}\right] + Bn_2(2\omega)\exp\left[\frac{ik_{2z}L}{2}\right] + h_{by}Z_0\exp[-i(k_{1z}L)]$$

At least one more equation is needed to determine *A*, *B*, and *R*. The boundary conditions at the II-III boundary provide this. In region 3, there is no nonlinear source term, so the solution is just a plane wave. In region 3:

$$\mathbf{E}_{2v}(\mathbf{r}) = T\hat{\mathbf{e}}^{\text{sub}}_{2v}\exp\left[i\left(\mathbf{k}^{\text{sub}}_2\cdot\left(\mathbf{r}-\frac{L}{2}\hat{\mathbf{z}}\right)\right)\right]$$

$$\mathbf{H}_{2v}(\mathbf{r}) = n_3(2\omega)T\hat{\mathbf{e}}^{\text{sub}}_{2\bar{v}}\exp\left[i\left(\mathbf{k}^{\text{sub}}_2\cdot\left(\mathbf{r}-\frac{L}{2}\hat{\mathbf{z}}\right)\right)\right]$$

where

$$\hat{\mathbf{e}}^{\text{sub}}_{2s} = (0,1,0)$$

$$\hat{\mathbf{e}}^{\text{sub}}_{2p} = \left(\sqrt{1-\left(\frac{n_1(\omega)}{n_3(2\omega)}\sin\theta\right)^2}, 0, \frac{-n_1(\omega)}{n_3(2\omega)}\sin\theta\right)$$

$$\mathbf{k}^{\text{sub}}_2 = \frac{2\omega n_3(2\omega)}{\text{c}}\left(\frac{n_1(\omega)}{n_3(2\omega)}\sin\theta, 0, \sqrt{1-\left(\frac{n_1(\omega)}{n_3(2\omega)}\sin\theta\right)^2}\right)$$

Applying the boundary conditions, for *v*=*p*,

$$\sqrt{1-\left(\frac{n_1(\omega)}{n_2(2\omega)}\sin\theta\right)^2}\left(A\exp\left[\frac{ik_{2z}L}{2}\right] - B\exp\left[\frac{-ik_{2z}L}{2}\right]\right)$$

$$+ e_{bx}\exp[i(k_{1z}L)] = T\sqrt{1-\left(\frac{n_1(\omega)}{n_3(2\omega)}\sin\theta\right)^2}$$

and

$$An_2(2\omega)\exp\left[+\frac{ik_{2z}L}{2}\right]+Bn_2(2\omega)\exp\left[\frac{-ik_{2z}L}{2}\right]+h_{by}Z_0\exp[+i(k_{1z}L)]=n_3(2\omega)T$$

The resulting expressions for A, B, R, and T are found by solving the following 4x4 system of equations:

$$-R\cos\theta_r=\sqrt{1-\left(\frac{n_1(\omega)}{n_2(2\omega)}\sin\theta\right)^2}\left(A\exp\left[-\frac{ik_{2z}L}{2}\right]-B\exp\left[\frac{ik_{2z}L}{2}\right]\right)+e_{bx}\exp[-i(k_{1z}L)]$$

$$R\,n_1(2\omega)=An_2(2\omega)\exp\left[-\frac{ik_{2z}L}{2}\right]+Bn_2(2\omega)\exp\left[\frac{ik_{2z}L}{2}\right]+h_{by}Z_0\exp[-i(k_{1z}L)]$$

$$\sqrt{1-\left(\frac{n_1(\omega)}{n_2(2\omega)}\sin\theta\right)^2}\left(A\exp\left[\frac{ik_{2z}L}{2}\right]-B\exp\left[\frac{-ik_{2z}L}{2}\right]\right)+e_{bx}\exp[i(k_{1z}L)]=T\sqrt{1-\left(\frac{n_1(\omega)}{n_3(2\omega)}\sin\theta\right)^2}$$

$$An_2(2\omega)\exp\left[+\frac{ik_{2z}L}{2}\right]+Bn_2(2\omega)\exp\left[\frac{-ik_{2z}L}{2}\right]+h_{by}Z_0\exp[+i(k_{1z}L)]=n_3(2\omega)T$$

References

Ahn, S. H., & Guo, L. J. (2009). Large-Area Roll-to-Roll and Roll-to-Plate Nanoimprint Lithography: A Step toward High-Throughput Application of Continuous Nanoimprinting. *ACS Nano, 3*(8), 2304-2310. doi: 10.1021/nn9003633

Arias, A. C., MacKenzie, J. D., McCulloch, I., Rivnay, J., & Salleo, A. (2010). Materials and Applications for Large Area Electronics: Solution-Based Approaches. *Chemical Reviews, 110*(1), 3-24. doi: 10.1021/cr900150b

Siliconductor Industry Association (2011). Global Semiconductor Sales Hit Record $298.3 Billion in 2010, from http://www.sia-online.org/news/2011/01/31/global-sales-reports-2011/global-semiconductor-sales-hit-record-298.3-billion-in-2010/

Bai, Y., Song, N., Gao, J. P., Sun, X., Wang, X., Yu, G., & Wang, Z. Y. (2005). A New Approach to Highly Electrooptically Active Materials Using Cross-Linkable, Hyperbranched Chromophore-Containing Oligomers as a Macromolecular Dopant. *Journal of the American Chemical Society, 127*(7), 2060-2061. doi: 10.1021/ja042854f

Bartella, J., Schroeder, J., & Witting, K. (2001). Characterization of ITO- and TiOxNy films by spectroscopic ellipsometry, spectraphotometry and XPS. *Applied Surface Science, 179*(1–4), 181-190. doi: 10.1016/s0169-4332(01)00307-5

Barto Jr, R. R., Frank, C. W., Bedworth, P. V., Ermer, S., & Taylor, R. E. (2005). Near-infrared optical-absorption behavior in high-beta nonlinear optical chromophore-polymer guest-host materials. II. Dye spacer length effects in an amorphous polycarbonate copolymer host. *The Journal of chemical physics, 122*, 234907.

Basel, Y., & Hassner, A. (2000). Di-tert-butyl Dicarbonate and 4-(Dimethylamino)pyridine Revisited. Their Reactions with Amines and Alcohols1. *The Journal of Organic Chemistry, 65*(20), 6368-6380. doi: 10.1021/jo000257f

Bauer, S., Eberle, G., Eisenmenger, W., & Schlaich, H. (1993). Second-harmonic generation with partially poled polymers. *Optics letters, 18*(1), 16-18.

Benight, S. J., Johnson, L. E., Barnes, R., Olbricht, B. C., Bale, D. H., Reid, P. J., . . . Robinson, B. H. (2010). Reduced Dimensionality in Organic Electro-Optic Materials: Theory and Defined Order. *The Journal of Physical Chemistry B, 114*(37), 11949-11956. doi: 10.1021/jp1022423

Betterton, K., Ebert, M., Haeussling, L., Lux, M. G., Twieg, R. J., Willson, C. G., . . . Grubbs, R. (1992). Strategies for crosslinking NLO polymers across the chromophore. *Polymeric Materials Science and Engineering, 66*, 312-313.

Blum, R., Sprave, M., Sablotny, J., & Eich, M. (1998). High-electric-field poling of nonlinear optical polymers. *JOSA B, 15*(1), 318-328.

Born, M., Wolf, E., & Bhatia, A. B. (1999). *Principles of optics: electromagnetic theory of propagation, interference and diffraction of light*: Cambridge Univ Pr.

Boyd, G. T., Francis, C. V., Trend, J. E., & Ender, D. A. (1991). Second-harmonic generation as a probe of rotational mobility in poled polymers. *J. Opt. Soc. Am. B, 8*(4), 887-894.

Boyd, R. W. (2008). *Nonlinear Optics* (3rd ed.). Boston: Elsevier.

Bristol, R. L. (2007). *The tri-lateral challenge of resolution, photospeed, and LER: scaling below 50nm?*, San Jose, CA, USA.

Burnett, J. H., Benck, E. C., Kaplan, S. G., Sirat, G. Y., & Mack, C. (2009). *Birefringence issues with uniaxial crystals as last lens elements for high-index immersion lithography*.

Chae, K. H. (1998). Thermal curing reaction of poly(glycidyl methacrylate) using photogenerated amines from oxime-urethane derivatives. *Macromolecular Rapid Communications, 19*(1), 1-4. doi: 10.1002/(sici)1521-3927(19980101)19:1<1::aid-marc1>3.0.co;2-6

Chafin, A. P., & Lindsay, G. A. (2008). A Pattern for Increasing the First Hyperpolarizability of a Push-Pull Polyene Dye as Indicated from DFT Calculations. *The Journal of Physical Chemistry C, 112*(21), 7829-7835. doi:10.1021/jp711265v

Chambers, C. R., Kusumoto, S., Lee, G. S., Vasudev, A., Walthal, L., Osborn, B. P., . . . Willson, C. G. (2003, 24 February 2003). *Dissolution inhibitors for 157-nm photolithography*. Paper presented at the Advances in Resist Technology and Processing XX, Santa Clara, CA.

Chen, A., Chuyanov, V., Garner, S., Steier, W., & Dalton, L. (1997). Modified Attenuated Total Reflection for the Fast and Routine electro-optic Measurements of Nonlinear Optical Polymer Thin Films. *Organic thin films for photonic applications, 14*, 158.

Chen, J. J. H., Lin, S., Fang, T., Chang, S., Krecinic, F., & Lin, B. J. (2009). *Multiple electron beam maskless lithography for high-volume manufacturing*.

Cheng, I. C., Kattamis, A., Long, K., Sturm, J. C., & Wagner, S. (2005). Stress control for overlay registration in a Si: H TFTs on flexible organic polymer foil substrates. *Journal of the Society for Information Display, 13*, 563.

Cho, Y., Gu, X., Hagiwara, Y., Kawakami, T., Ogata, T., Rawlings, B., . . . Willson, C. G. (2011). *Polymer-bound photobase generators and photoacid generators for pitch division lithography*, San Jose, California, USA.

Clark, W. G., & Kerlin, A. L. (1967). Solid State Gated Integrator. *Review of Scientific Instruments, 38*(11), 1593-1596.

Clays, K., & Persoons, A. (1991). Hyper-Rayleigh scattering in solution. *Physical Review Letters, 66*(23), 2980-2983.

Contreras, A. P., Tlenkopatchev, M. A., del Mar Lopez-Gonzalez, M., & Riande, E. (2002). Synthesis and Gas Transport Properties of New High Glass Transition Temperature Ring-Opened Polynorbornenes. *Macromolecules, 35*(12), 4677-4684. doi: 10.1021/ma011959p

Cramer, N. B., & Bowman, C. N. (2001). Kinetics of thiol–ene and thiol–acrylate photopolymerizations with real-time fourier transform infrared. *Journal of Polymer Science Part A: Polymer Chemistry, 39*(19), 3311-3319. doi: 10.1002/pola.1314

Dalton, L. R. (2003). Organic electro-optic materials. Past, present, and future. *PMSE Preprints, 88*, 173-174.

Dalton, L. R., Steier, W. H., Robinson, B. H., Zhang, C., Ren, A., Garner, S., . . . Jen, A. (1999). From molecules to opto-chips: organic electro-optic materials. *Journal of Materials Chemistry, 9*(9), 1905-1920.

Dalton, L. R., Sullivan, P. A., & Bale, D. H. (2009). Electric Field Poled Organic Electro-optic Materials: State of the Art and Future Prospects. *Chemical Reviews, 110*(1), 25-55. doi: 10.1021/cr9000429

Decker, C. (2002). Kinetic study and new applications of UV radiation curing. *Macromolecular Rapid Communications, 23*(18), 1067-1093.

Dureiko, R. D., Schuele, D. E., & Singer, K. D. (1998). Modeling relaxation processes in poled electro-optic polymer films. *J. Opt. Soc. Am. B, 15*(1), 338-350.

Finders, J., Dusa, M., Vleeming, B., Megens, H., Hepp, B., Maenhoudt, M., . . . Vandeweyer, T. (2008). *Double patterning for 32nm and below: an update*, San Jose, CA, USA.

Fonseca, C., Somervell, M., Scheer, S., Printz, W., Nafus, K., Hatakeyama, S., . . . Gronheid, R. (2009). *Advances and challenges in dual-tone development process optimization*, San Jose, CA, USA.

Franken, P. A., Hill, A. E., Peters, C. W., & Weinreich, G. (1961). Generation of Optical Harmonics. *Physical Review Letters, 7*(4), 118-119.

Frechet, J. M. J., Matuszczak, S., Reck, B., Stover, H. D. H., & Willson, C. G. (1991). Chemically amplified imaging materials based on electrophilic aromatic substitution: poly [4-(acetoxymethyl) styrene-co-4-hydroxystyrene]. *Macromolecules, 24*(8), 1746-1754.

Furukawa, T., & Johnson, G. E. (1981). Measurements of ferroelectric switching characteristics in polyvinylidene fluoride. *Applied Physics Letters, 38*(12), 1027-1029. doi: 10.1063/1.92232

Giacometti, J. A., & Campos, J. S. C. (1990). Constant current corona triode with grid voltage control. Application to polymer foil charging. *Review of Scientific Instruments, 61*(3), 1143-1150.

Gleskova, H., Cheng, I. C., Wagner, S., Sturm, J. C., & Suo, Z. (2006). Mechanics of thin-film transistors and solar cells on flexible substrates. *Solar Energy, 80*(6), 687-693. doi: 10.1016/j.solener.2005.10.010

Godt, A., Fréchet, J. M. J., Beecher, J. E., & Willand, C. S. (1995). Photopolymers for non-linear optics: Design and synthesis of a polymer containing styrene-terminated tolane chromophores and its stabilization in an oriented configuration by photocrosslinking. *Macromolecular Chemistry and Physics, 196*(1), 133-147. doi: 10.1002/macp.1995.021960108

Gu, X., Bates, C., Cho, Y., Costner, E., Marzuka, F., Nagai, T., . . . Wilson, C. G. (2009). A New Materials-based Pitch Division Technique. *Journal of Photopolymer Science and Technology, 22*(6), 773-781.

Gu, X., Bates, C. M., Cho, Y., Kawakami, T., Nagai, T., Ogata, T., . . . Willson, C. G. (2010). *Photobase generator assisted pitch division*, San Jose, California, USA.

Gu, X., Cho, Y., Kawakami, T., Hagiwara, Y., Rawlings, B., Mesch, R., . . . Willson, C. G. (2011). *Photobase generator enabled pitch division: a progress report*, San Jose, California, USA.

Hayden, L. M., Sauter, G. F., Ore, F. R., Pasillas, P. L., Hoover, J. M., Lindsay, G. A., & Henry, R. A. (1990). Second-order nonlinear optical measurements in guest-host and side-chain polymers. *Journal of Applied Physics, 68*(2), 456-465.

Hecht, E. (2002). *Optics (4th edn)*. San Francisco, CA: Addison-Wesley.

Herman, W. N., & Hayden, L. M. (1995). Maker fringes revisited: second-harmonic generation from birefringent or absorbing materials. *J. Opt. Soc. Am. B, 12*(3), 416-427.

Hilczer, B., & Kulek, J. (1998). The effect of dielectric heterogeneity on the pyroelectric response of PVDF. *Dielectrics and Electrical Insulation, IEEE Transactions on, 5*(1), 45-50.

Hill, R. A., Knoesen, A., & Mortazavi, M. A. (1994). Corona poling of nonlinear polymer thin films for electro-optic modulators. *Applied Physics Letters, 65*(14), 1733-1735.

Hinsberg, W. D., MacDonald, S. A., Pederson, L. A., & Willson, C. G. (1989). A lithographic analog of color photography: self-aligning photolithography using a

resist with wavelength-dependent tone. *Journal of Imaging Science, 33*(4), 129-135.

Hinsberg, W. D., Pederson, L. A., & Willson, C. G. (1988, 29 February-2 March). *Zero-misalignment Lithographic Process Using a Photoresist with Wavelength-selected tone.* Paper presented at the Advances in resist technology and processing V, Santa Clara, California.

Huang, M., Zhao, F., Cheng, Y., Xu, N., & Xu, Z. (2008). Large area uniform nanostructures fabricated by direct femtosecond laser ablation. *Opt. Express, 16*(23), 19354-19365.

Huang, S., Kim, T. D., Luo, J., Hau, S. K., Shi, Z., Zhou, X. H., . . . Alex, K. Y. J. (2010). Highly efficient electro-optic polymers through improved poling using a thin TiO-modified transparent electrode. *Applied Physics Letters, 96*, 243311.

Hubbard, M. A., Marks, T. J., Lin, W., & Wong, G. K. (1992). Poled polymeric nonlinear optical materials. Enhanced second harmonic generation temporal stability of epoxy-based matrixes containing a difunctional chromophoric comonomer. *Chemistry of Materials, 4*(5), 965-968. doi: 10.1021/cm00023a003

Hubbard, M. A., Marks, T. J., Yang, J., & Wong, G. K. (1989). Poled polymeric nonlinear optical materials. Enhanced second harmonic generation stability of crosslinkable matrix/chromophore ensembles. *Chemistry of Materials, 1*(2), 167-169. doi: 10.1021/cm00002a001

Iwayanagi, T., Kohashi, T., Nonogaki, S., Matsuzawa, T., Douta, K., & Yanazawa, H. (1981). Azide-phenolic resin photoresists for deep UV lithography. *Electron Devices, IEEE Transactions on, 28*(11), 1306-1310.

Jain, K., Klosner, M., Zemel, M., & Raghunandan, S. (2005). Flexible Electronics and Displays: High-Resolution, Roll-to-Roll, Projection Lithography and Photoablation Processing Technologies for High-Throughput Production. *Proceedings of the IEEE, 93*(8), 1500-1510.

Jazbinsek, M., Mutter, L., & Gunter, P. (2008). Photonic Applications With the Organic Nonlinear Optical Crystal DAST. [Review]. *Ieee Journal of Selected Topics in Quantum Electronics, 14*(5), 1298-1311. doi: 10.1109/JSTQE.2008.921407

Jerphagnon, J., & Kurtz, S. K. (1970). Maker Fringes: A Detailed Comparison of Theory and Experiment for Isotropic and Uniaxial Crystals. *Journal of Applied Physics, 41*(4), 1667-1681.

Jungbauer, D., Teraoka, I., Yoon, D. Y., Reck, B., Swalen, J. D., Twieg, R., & Willson, C. G. (1991). Second order nonlinear optical properties and relaxation characteristics of poled linear epoxy polymers with tolane chromophores. *Journal of Applied Physics, 69*(12), 8011-8017.

Kanji, S., Satoshi, N., & Masamitsu, S. (2005). Thermally Stable Carbamates as Novel Photobase Generator. *Journal of Photopolymer Science and Technology, 18*(1), 141-148.

Kim, T.-D., Kang, J.-W., Luo, J., Jang, S.-H., Ka, J.-W., Tucker, N., . . . Jen, A. K. Y. (2007). Ultralarge and Thermally Stable Electro-Optic Activities from Supramolecular Self-Assembled Molecular Glasses. *Journal of the American Chemical Society, 129*(3), 488-489. doi: 10.1021/ja067970s

Kim, T.-D., Luo, J., Tian, Y., Ka, J.-W., Tucker, N. M., Haller, M., . . . Jen, A. K. Y. (2006). Diels-Alder "Click Chemistry" for Highly Efficient Electrooptic Polymers. *Macromolecules, 39*(5), 1676-1680. doi: 10.1021/ma052087k

Kuo, Y. H., Luo, J., Steier, W. H., & Jen, A. K. Y. (2006). Enhanced thermal stability of electrooptic polymer modulators using the Diels-Alder crosslinkable polymer. *IEEE Photonics Technology Letters, 18*(1), 175-177.

Kuzyk, M. G. (2000). Physical Limits on Electronic Nonlinear Molecular Susceptibilities. *Physical Review Letters, 85*(6), 1218-1221.

Kuzyk, M. G., & Dirk, C. W. (1998). *Characterization techniques and tabulations for organic nonlinear optical materials* (Vol. 60): CRC.

Lee, S. K., Cho, M. J., Jin, J.-I., & Choi, D. H. (2007). Stability control of the electrooptic effect with new maleimide copolymers containing photoreactive tricyanopyrrolidene-based chromophores. *Journal of Polymer Science Part A: Polymer Chemistry, 45*(3), 531-542. doi: 10.1002/pola.21887

Lee, T. Y., Roper, T. M., Jonsson, E. S., Kudyakov, I., Viswanathan, K., Nason, C., . . . Hoyle, C. (2003). The kinetics of vinyl acrylate photopolymerization. *Polymer, 44*(10), 2859-2865.

Leitgeb, A., Wappel, J., & Slugovc, C. (2010). The ROMP toolbox upgraded. *Polymer, 51*(14), 2927-2946. doi: 10.1016/j.polymer.2010.05.002

Liberman, V., Rothschild, M., Palmacci, S., Bristol, R., Byers, J., Turro, N., . . . Zimmerman, P. (2008). *High-index immersion lithography: preventing lens photocontamination and identifying optical behavior of LuAG*.

Long, B. (2009). *Design, Synthesis, and Application of Lithographic Resists and Nonlinear Optical Materials.* (Ph.D.), University of Texas at Austin, Austin.

Love, J. A., Morgan, J. P., Trnka, T. M., & Grubbs, R. H. (2002). A Practical and Highly Active Ruthenium-Based Catalyst that Effects the Cross Metathesis of Acrylonitrile. *Angewandte Chemie International Edition, 41*(21), 4035-4037. doi: 10.1002/1521-3773(20021104)41:21<4035::aid-anie4035>3.0.co;2-i

Mao, S. S. H., Ra, Y., Guo, L., Zhang, C., Dalton, L. R., Chen, A., . . . Steier, W. H. (1998). Progress toward Device-Quality Second-Order Nonlinear Optical Materials. 1. Influence of Composition and Processing Conditions on

Nonlinearity, Temporal Stability, and Optical Loss. *Chemistry of Materials, 10*(1), 146-155. doi: 10.1021/cm9702833

Marder, S. R., & Perry, J. W. (1994). Nonlinear Optical Polymers: Discovery to Market in 10 Years? *Science, 263*, 1706-1707.

Marder, S. R., Perry, J. W., & Schaefer, W. P. (1989). Synthesis of organic salts with large 2nd-order optical nonlinearities. [Article]. *Science, 245*(4918), 626-628.

Matsumoto, K., Costner, E. A., Nishimura, I., Ueda, M., & Willson, C. G. (2008). High Index Resist for 193 nm Immersion Lithography. *Macromolecules, 41*(15), 5674-5680. doi: 10.1021/ma800295s

Moore, G. E. (1998). Cramming more components onto integrated circuits. *Proceedings of the IEEE, 86*(1), 82-85.

Morichere, D., Chollet, P. A., Fleming, W., Jurich, M., Smith, B. A., & Swalen, J. D. (1993). Electro-optic effects in two tolane side-chain nonlinear-optical polymers: comparison between measured coefficients and second-harmonic generation. *Journal of the Optical Society of America B: Optical Physics, 10*(10), 1894-1900.

Neumann, M. G., Miranda Jr, W. G., Schmitt, C. C., Rueggeberg, F. A., & Correa, I. C. (2005). Molar extinction coefficients and the photon absorption efficiency of dental photoinitiators and light curing units. *Journal of Dentistry, 33*(6), 525-532. doi: 10.1016/j.jdent.2004.11.013

Ohba, T., Nakai, D., Suyama, K., & Shirai, M. (2004). Photo-Crosslinking of Poly(glycidyl methacrylate) Using Di-functional Photobase Generators. *Journal of Photopolymer Science and Technology, 17*(1), 11-14.

Park, D. H. (2008). *Characterization of linear electro-optic effect of poled organic thin films*. (Ph.D.), University of Maryland, College Park, MD.

Park, D. H., & Herman, W. N. (2012). Closed-form Maker fringe formulas for poled polymer thin films in multilayer structures. *Opt. Express, 20*(1), 173-185.

Park, D. H., Lee, C. H., & Herman, W. N. (2006). Analysis of multiple reflection effects in reflective measurements of electro-optic coefficients of poled polymers in multilayer structures. *Opt. Express, 14*(19), 8866-8884.

Park, D. H., Luo, J., Jen, A. K.-Y., & Herman, W. N. (2011). Simplified Reflection Fabry-Perot Method for Determination of Electro-Optic Coefficients of Poled Polymer Thin Films. *Polymers, 3*(3), 1310-1324.

Pawloski, A. R., Acheta, A., Lalovic, I., La Fontaine, B. M., & Levinson, H. J. (2004). *Characterization of line-edge roughness in photoresist using an image fading technique*, Santa Clara, CA, USA.

Prasad, P. N., & Williams, D. J. (1991). *Introduction to Nonlinear Optical Effects in Molecules and Polymers*. New York: John Wiley & Sons, Inc.

Roper, T. M., Guymon, C., Jönsson, E., & Hoyle, C. (2004). Influence of the alkene structure on the mechanism and kinetics of thiol–alkene photopolymerizations with real-time infrared spectroscopy. *Journal of Polymer Science Part A: Polymer Chemistry, 42*(24), 6283-6298.

Schildkraut, J. S. (1990). Determination of the electrooptic coefficient of a poled polymer film. *Applied Optics, 29*(19), 2839-2841.

Scholl, M., Ding, S., Lee, C. W., & Grubbs, R. H. (1999). Synthesis and Activity of a New Generation of Ruthenium-Based Olefin Metathesis Catalysts Coordinated with 1,3-Dimesityl-4,5-dihydroimidazol-2-ylidene LigandsÂ§. *Organic Letters, 1*(6), 953-956. doi: 10.1021/ol990909q

Schwab, P., France, M. B., Ziller, J. W., & Grubbs, R. H. (1995). A Series of Well-Defined Metathesis Catalysts–Synthesis of [RuCl2 (CHR′)(PR3) 2] and Its Reactions. *Angewandte Chemie International Edition in English, 34*(18).

Shanmuganathan, K., Sankhagowit, R. K., Iyer, P., & Ellison, C. J. (2011). Thiol–Ene Chemistry: A Greener Approach to Making Chemically and Thermally Stable Fibers. *Chemistry of Materials, 23*(21), 4726-4732. doi: 10.1021/cm2015093

Shi, Z., Liang, W., Luo, J., Huang, S., Polishak, B. M., Li, X., . . . Jen, A. K. Y. (2010). Tuning the Kinetics and Energetics of Diels−Alder Cycloaddition Reactions to Improve Poling Efficiency and Thermal Stability of High-Temperature Cross-Linked Electro-Optic Polymers. *Chemistry of Materials, 22*(19), 5601-5608. doi: 10.1021/cm101815b

Shi, Z., Luo, J., Huang, S., Cheng, Y.-J., Kim, T.-D., Polishak, B. M., . . . Jen, A. K. Y. (2009). Controlled Diels−Alder Reactions Used To Incorporate Highly Efficient Polyenic Chromophores into Maleimide-Containing Side-Chain Polymers for Electro-Optics. *Macromolecules, 42*(7), 2438-2445. doi: 10.1021/ma802612g

Singer, K. D., & Garito, A. F. (1981). Measurements of molecular second order optical susceptibilities using dc induced second harmonic generation. *The Journal of Chemical Physics, 75*(7), 3572-3580. doi: 10.1063/1.442467

Singer, K. D., Kuzyk, M. G., Holland, W. R., Sohn, J. E., Lalama, S. J., Comizzoli, R. B., . . . Schilling, M. L. (1988). Electro-optic phase modulation and optical second-harmonic generation in corona-poled polymer films. *Applied Physics Letters, 53*(19), 1800-1802.

Singer, K. D., Kuzyk, M. G., & Sohn, J. E. (1987). Second-order nonlinear-optical processes in orientationally ordered materials: relationship between molecular and macroscopic properties. *J. Opt. Soc. Am. B, 4*(6), 968-976.

Smith, B. W., Bourov, A., Fan, Y., Cropanese, F., & Hammond, P. (2004). *Amphibian XIS: an immersion lithography microstepper platform*, San Jose, CA, USA.

Sprave, M., Blum, R., & Eich, M. (1996). High electric field conduction mechanisms in electrode poling of electro-optic polymers. *Applied Physics Letters, 69*(20), 2962-2964.

Stansbury, J. W., & Dickens, S. H. (2001). Determination of double bond conversion in dental resins by near infrared spectroscopy. *Dent Mater, 17*(1), 71-79.

Sullivan, P. A., Akelaitis, A. J. P., Lee, S. K., McGrew, G., Lee, S. K., Choi, D. H., & Dalton, L. R. (2005). Novel Dendritic Chromophores for Electro-optics: Influence of Binding Mode and Attachment Flexibility on Electro-optic Behavior. *Chemistry of Materials, 18*(2), 344-351. doi: 10.1021/cm0517420

Sullivan, P. A., Rommel, H., Liao, Y., Olbricht, B. C., Akelaitis, A. J. P., Firestone, K. A., . . . Dalton, L. R. (2007). Theory-Guided Design and Synthesis of Multichromophore Dendrimers: An Analysis of the Electro-optic Effect. *Journal of the American Chemical Society, 129*(24), 7523-7530. doi: 10.1021/ja068322b

Suyama, K., & Shirai, M. (2009). Photobase generators: Recent progress and application trend in polymer systems. *Progress in Polymer Science, 34*(2), 194-209.

Tay, S., Blanche, P. A., Voorakaranam, R., Tunc, A. V., Lin, W., Rokutanda, S., . . . Peyghambarian, N. (2008). An updatable holographic three-dimensional display. *Nature, 451*(7179), 694-698.

Taylor, J. C., Costner, E. A., Goh, S., Wojtczak, W., Dewulf, D., & Willson, C. G. (2008). The effect of added salts on the optical properties of water for high index immersion lithography fluids. *Journal of Vacuum Science & Technology B: Microelectronics and Nanometer Structures, 26*, 506.

Tehfe, M.-A., Blanchard, N., Fries, C., Lalevée, J., Allonas, X., & Fouassier, J. P. (2010). Bis(germyl)ketones: Toward a New Class of Type I Photoinitiating Systems Sensitive Above 500 nm? *Macromolecular Rapid Communications, 31*(5), 473-478. doi: 10.1002/marc.200900695

Teng, C. C., & Man, H. T. (1990). Simple reflection technique for measuring the electro-optic coefficient of poled polymers. *Applied Physics Letters, 56*(18), 1734-1736.

Van Look, L., Bekaert, J., Truffert, V., Wiaux, V., Lazzarino, F., Maenhoudt, M., . . . Tarutani, S. (2010). *Printing the metal and contact layers for the 32- and 22-nm node: comparing positive and negative tone development process*, San Jose, California, USA.

Vogt, B. D., Kang, S., Prabhu, V. M., Rao, A., Lin, E. K., Wu, W.-l., . . . Turnquest, K. (2007). Influence of base additives on the reaction-diffusion front of model chemically amplified photoresists. *Journal of Vacuum Science & Technology B: Microelectronics and Nanometer Structures, 25*(1), 175-182.

Wagner, C., & Harned, N. (2010). EUV lithography: Lithography gets extreme. [10.1038/nphoton.2009.251]. *Nat Photon, 4*(1), 24-26.

Wang, X. (1996). Gated integrator with signal baseline subtraction: Google Patents.

Wang, X., Chen, J.-I., Marturunkakul, S., Li, L., Kumar, J., & Tripathy, S. K. (1997). Epoxy-Based Nonlinear Optical Polymers Functionalized with Tricyanovinyl Chromophores. *Chemistry of Materials, 9*(1), 45-50. doi: 10.1021/cm950560a

Wang, Z., Sun, W., Chen, A., Kosilkin, I., Bale, D., & Dalton, L. R. (2011). Organic electro-optic thin films by simultaneous vacuum deposition and laser-assisted poling. *Opt. Lett., 36*(15), 2853-2855.

Weis, R. S., & Gaylord, T. K. (1985). Lithium niobate: summary of physical properties and crystal structure. [Article]. *Applied Physics A: Materials Science & Processing, 37*(4), 191-203.

Williams, M. L., Landel, R. F., & Ferry, J. D. (1955). The Temperature Dependence of Relaxation Mechanisms in Amorphous Polymers and Other Glass-forming Liquids. *Journal of the American Chemical Society, 77*(14), 3701-3707. doi: 10.1021/ja01619a008

Wilson, C. G. (2009). A Decade of Step and Flash Imprint Lithography. *Journal of Photopolymer Science and Technology, 22*(2), 147-153.

Wooten, E. L., Kissa, K. M., Yi-Yan, A., Murphy, E. J., Lafaw, D. A., Hallemeier, P. F., . . . Bossi, D. E. (2000). A review of lithium niobate modulators for fiber-optic communications systems. *Selected Topics in Quantum Electronics, IEEE Journal of, 6*(1), 69-82.

Yamamoto, J., Uchino, S., Hattori, T., Yoshimura, T., & Murai, F. (1996). Nanometer electron beam lithography with azide-phenolic resin resist systems. *Japanese journal of applied physics, 35*(part 1), 6511-6516.

Yamasaki, K., Tanaka, A., Kimura, T., & Kajimoto, O. (1995). An inexpensive handmade grated integrator. *Review of Scientific Instruments, 66*(8), 4395-4396.

Yongrae, R., Varadan, V. V., & Varadan, V. K. (2002). Characterization of all the elastic, dielectric, and piezoelectric constants of uniaxially oriented poled PVDF films. *Ultrasonics, Ferroelectrics and Frequency Control, IEEE Transactions on, 49*(6), 836-847.

Zernike, F., & Midwinter, J. E. (2006). *Applied Nonlinear Optics*. New York: Dover.

Zhang, C., Dalton, L. R., Oh, M.-C., Zhang, H., & Steier, W. H. (2001). Low V Electrooptic Modulators from CLD-1: Chromophore Design and Synthesis, Material Processing, and Characterization. *Chemistry of Materials, 13*(9), 3043-3050. doi: 10.1021/cm010463j

Zhou, J., & Kuzyk*, M. G. (2008). Intrinsic Hyperpolarizabilities as a Figure of Merit for Electro-optic Molecules†. *The Journal of Physical Chemistry C, 112*(21), 7978-7982. doi: 10.1021/jp7120824

Zhou, J., Szafruga, U. B., Watkins, D. S., & Kuzyk, M. G. (2007). Optimizing potential energy functions for maximal intrinsic hyperpolarizability. *Physical Review A, 76*(5), 053831.

Vita

Brandon Mark Rawlings was born in 1983 in Dublin, GA. He graduated in 2002 from Dublin High School in Dublin, GA and concurrently earned an Associates of Science degree at Middle Georgia College in Cochran, GA through the Georgia Academy of Aviation, Mathematics, Engineering, and Science. He attended the California Institute of Technology from 2002 to 2006 and earned a Bachelor of Science with Honor degree in chemical engineering from Caltech in June 2006. Upon graduation, Brandon enrolled in the chemical engineering Ph.D. program under the supervision of Professor Grant Willson. During the summer of 2010, Brandon completed an internship with Intel Corporation in Hillsboro, OR. He has accepted a full-time position with Intel in Chandler, AZ.

Permanent Address: brandonrawlings@gmail.com

This manuscript was typed by the author.